이학박사 학위논문

Antiviral Drug Discovery and Cell Differentiation by Using Biocompatible Nanomaterials

생체적합성 나노물질을 활용한 항바이러스 의약품 발굴 및 세포 분화 연구

2021 년 02 월

서울대학교 대학원

화학과 나노바이오화학 전공

박 세 진

Ph.D DISSERTATION

Antiviral Drug Discovery and Cell Differentiation by Using Biocompatible Nanomaterials

By

Se-Jin Park

Advisor: Prof. Dal-Hee Min

February, 2021

Department of Chemistry

Graduate School

Seoul National University

Antiviral Drug Discovery and Cell Differentiation by Using Biocompatible Nanomaterials

지도 교수 민 달 희

이 논문을 이학박사 학위논문으로 제출함
2020 년 11 월

서울대학교 대학원
화학과 나노바이오화학 전공
박 세 진

박세진의 이학박사 학위논문을 인준함
2020 년 11 월

위 원 장 홍 종 인 (인)

부위원장 민 달 희 (인)

위 원 정 택 동

위 원 이 연 (인)

위 원 우 재 성 (인)

Abstract

Antiviral Drug Discovery and Cell Differentiation by Using Biocompatible Nanomaterials

Se-Jin Park
Department of Chemistry
(Major: Nanobiochemistry)
The Graduate School
Seoul National University

Since the arousal of the massive development and production of chemical medicine in 1980s, explosive scientific achievements of the traditional pharmaceuticals based on chemical products were accomplished. Nevertheless, numerous infectious diseases and neurological incurable disorders has been yet to be conquered, due to the integrated issues involving the complexity of the disease mechanism studies, difficulty in the critical factor control and so on. Therapeutic research on the RNA virus-associated diseases, for example, had suffered the drastic challenges such as the high rate of genetic mutation and increase in chance of drug evasion. As a result, seldom success has been accomplished in the development of antiviral drugs or vaccines to cope with such. Recent outbreak of several epidemics has been aggressive and severe, which has evoked the urgent need for the antiviral drugs and led to the massive competition of research and development among numerous pharmaceuticals.

In the meantime, it has not been long since the potential of nanotechnology has risen on debate for its interdisciplinary application. Nanotechnology includes all research area where various materials in nano (10^{-9}) scale are involved. Nano-sized materials have drawn much attention for their specific features (such as electrical, optical properties) distinguished from those of the bulk sources. Despite

its short history compared to other research area, nanotechnology is now drawing much attention for their unique properties advantageous for diverse biological applications. Such attempts include the development of biofunctional nanodevices such as biosensor, intracellular delivery carrier.

Here, we introduce three representative multidisciplinary studies utilizing the nanotechnology: 1) rapid drug discovery incorporating a fluorescence-based nanobiosensor, 2) the efficient strategy for neural differentiation of the stem cell with porous particles, and 3) the non-viral direct reprogramming strategy to generate neural stem cell with carbon dot nanoreagent. In each chapter, we introduce the specific characteristics of the involved nanomaterials and describe how these features contributed to achieve the individual goals.

In the first research, we propose our achievement on the development and utilization of the fluorescence nanobiosensor to the rapid discovery of the antiviral drug against the pathogenic RNA virus. We have developed a facile, and efficient viral enzyme activity analyzing platform incorporating modified RNA and graphene oxide, named as RANGO. We utilized it to the multi-well based, high-throughput chemical screening to identify novel direct-acting antiviral agents against a specific pathogenic RNA virus named as dengue virus from the FDA-approved small molecule library. Throughout the series of validation process carried out both *in vitro* and *in vivo*, we suggest the very compound as the potent direct-acting antiviral drug candidate.

In the second research, we suggest the efficient method to mimic the neural differentiation process of mouse embryonic stem cell *in vitro* incorporating the porous silica nanoparticle as a drug delivery carrier. We selected the functionalized nanoparticle showing the maximum drug loading capacity and investigated its high capability of intracellular delivery by penetrating in the cell

cluster. We confirm that the selected nanoaparticle could effectively support the stable, sustained delivery of the retinoic acid into the mouse embryonic stem cell, which led to the efficient induction of the retinoic acid-mediated neural differentiation.

In the third research, we introduce the non-viral, direct reprogramming strategy to generate neural stem cell from somatic cell incorporating carbon dot nanocarrier. We observed that the carbon nanodot carrier with the optimized surface charge showed the higher biocompatibility and gene delivery efficiency against the human fibroblast. With sequential evaluation from the non-viral gene delivery to the induction of the neural differentiation, we suggest that the carbon nanodot could be utilized as the non-viral gene delivery carrier to facilitate the direct reprogramming of human fibroblast into neural stem cell-like cell.

We suggest that our research accomplishments could provide the fundamental ideas to overcome the limitations of classical approaches in the field of drug discovery and cell engineering.

Keywords: Nanosensor, Nanoparticle, Drug delivery, Gene delivery, Antiviral drug discovery, High-throughput screening, Stem cell, Cell engineering

Student Number: 2014-21248

Table of Contents

List of Figures

1. Introduction

2. Discovery of direct-acting antiviral agents with a graphene-based fluorescent nanosensor

3. Highly efficient and rapid neural differentiation of mouse embryonic stem cells based on retinoic acid-encapsulated porous nanoparticle

Chapter 1. Introduction

1.1 Nanotechnology for antiviral drug discovery

The emergence of the virus-associated epidemics has become a repetitive worldwide event and considered as one of the major global threats. It is generally accepted that the RNA virus is more problematic than DNA virus, due to the high chance of genetic mutation. The rapidity of genetic mutation in RNA virus acts as the main hurdle in the antiviral drug discovery and development. Once the virus-mediated disease emerged, it could be disastrous unless its global spread-out is blocked as soon as possible; it may lead to the pandemic, and even worse, may end up to the endemic (with repetitive, periodic global emergence of certain viral disease)[1-3]. It has been proven that there is a strong relationship between the fatalness of the epidemic disease and the development of therapeutics[4]. In the case of Influenza, for example, global efforts on the development of therapeutic agents (universal vaccines and antiviral drugs) has attributed to decrease the seasonal emergence of the disease[5-8].

Unfortunately, however, only little success had been achieved against those of other fatal viral diseases discovered so far. Representative viral diseases include the Ebola[9, 10], Spanish influenza[11], Severe Acute Respiratory Syndrome (SARS)[12], followed by series of health crisis by Middle East Respiratory Syndrome (MERS)[13], ZIKA in 2017[14], and the notorious COVID-19 by the SARS-CoV2 discovered in late 2019[15, 16]. While the wide spread-out of COVID-19 is still in progress, recent reports even predicted the advent of the swine influenza prone to infect humans, warning the potential of another pandemic crisis[17]. Considering that little achievement has been made on the development of antivirals or vaccines to deal with such cases, it is urgent to seek for the innovative tools for the diagnosis and therapeutics (including vaccine and drugs) to make a breakthrough

within the golden time.

While tremendous struggles have been made in the biological research area to deal with such viruses, studies on the nano-sized materials had been originally emerged in the middle of the 1900s and discussed separately from the antiviral research[18]. Each nanomaterial possesses specific functions, resulting in the possibility of a wide-range application to various research fields. It has not been long since several opinions have been discussed depicting the potential of the nanomaterials to provide the functional tools to assist efficient antiviral research[19]. Started from the utilization of the gold nanoparticle for the single molecular detection of the virus [20], the potential of the nanomaterials as the source component for the virus detection tools has been extensively evaluated.

Meanwhile, graphene, a two-dimensional, single-layered carbon sheet isolated from the graphite[21], has drawn much attention for its unique chemical and physical properties suitable for the development of sensors[22]. Various applications have been suggested to demonstrate analytic tools utilizing not only graphene itself but also its derivatives[23-25]. Among diverse graphene derivatives, graphene oxide (GO) has been extensively applied to development of biosensors as well, by utilizing its unique features including the high dispersion in water, amphiphilicity, the selective adsorption ability of the biomolecules via π-π stacking or non-covalent interaction and fluorescence quenching ability[26, 27]. Along with such functional evaluations of GO, numerous attempts have been made to extend the application of GO into the development of the diverse biosensors[28] based on colorimetric, electrochemical, and optical methods.

In terms of virus research, GO-based nanobiosensors have been evaluated for various purposes, including the virus detection and antiviral drug discovery. Here, we introduce the one significant way of the application of the specified GO

biosensor as the antiviral drug screening platform. We demonstrate the whole series of research ranging from the development of the high-throughput screening system to the discovery and therapeutic evaluation of the direct-acting antiviral drug candidate by utilization of the platform[29].

1.2 Nanotechnology for cell engineering

The concept of cell therapy has risen followed by the vigorous growth of the stem cell-mediated medical research (also connected with the regenerative medicine), as the methodological solution for the cell treatment. The first attempt of cell therapy was suggested in the late 1950s, incorporating the bone marrow transplantation[30]. As can be seen from this example, cell therapy involves the cellular delivery into either the bloodstream or the targeted tissue of matter. The purpose of cell therapy includes the stimulation of various regenerative performance, such as promotion of the vascularization and production of the signaling molecules (hormones, cytokine, etc.)[31]. It is considered as one of the most straightforward strategy used in the regenerative medicine.

Several critical limitations of cell therapy include the low survival rate of the engrafted cells and failure of the precise targeting towards the desired tissue[32-33]. In addition, the limited source for the securement of cells in demand has been considered as another bottleneck of the cell therapy. Typically, cells for the engraftment are collected from either autologous or allogeneic sources, using several methods such as tissue biopsy. Such issue has accelerated the high demand for the strategic breakthrough, leading to the utilization of the new technology named as cell engineering.

Cell engineering is the multi-disciplinary area of research connecting several distinguished fields, including medicine, biology and material science[34]. In terms of cell therapy, the ultimate purpose of cell engineering includes the generation of “rare cells” from the “common cells (in other words, easily obtained cells)”. Typical cell engineering process requires the incorporation of various biomolecules (genes, proteins, etc. into the cells. For such purpose, vectors derived from the virus had been the most widely used delivery vehicle[35]. The

advantage of viral vectors includes the high delivery efficiency and reliability based on the numerous case studies reported. However, there still have been several issues constantly depicted, such as the genetic instability (also known as insertional mutagenesis[36]) derived from the intrinsic characteristics of the viral origin[37].

Meanwhile, it has not been long since the nano-sized intracellular reagents have drawn attention in the field of cell engineering. In prospect of cell engineering, nanotechnology is considered as relatively new, yet promising strategic source for the future research[38]. Utilization of nanotechnology may provide various improved tools for drug delivery, detection, and diagnostics. Several features of the nanomaterials which derived from their size factor, such as high surface area/volume ratio and flexibility, were considered attractive to be applied for such purpose[39].

In this regard, one of the noticeable future achievements expected by the application of nanomaterials may be the non-viral cell engineering. Typical non-viral vectors used for such purpose have involved the liposomes or cationic polymers[40]. Although several commercialized reagents have been widely used in the laboratory, conventional non-viral reagents have shown distinct limitations on guaranteeing either the stable transfection efficiency or low cytotoxicity. For liposome-based vectors, for example, the transfection efficiency and cytotoxicity are highly dependent to various factors including the degree of unsaturation, configuration of the hydrophobic chain, and the overall morphology of the complex[41-43]. For polymer-based vectors, numerous studies have been carried out to design a new, functional polymer ensuring both high transfection efficiency and low cytotoxicity, yet improvements are required for practical use[44]. Utilization of the nanomaterials could be one of the promising strategies to overcome such issues.

Nanomaterials possess highly modular features, by the wide variety of biochemical functionalization to endow the desired characteristics[45]. To date, numerous applications have been suggested to demonstrate the non-viral cell engineering by the nanomaterial-mediated delivery of various functional biomolecules[46-48].

Here, we introduce two representative demonstration of the nanomaterial-based cell engineering. First, we demonstrate the *in vitro* imitation of the neuronal differentiation process of mouse embryonic stem cell with enhanced turnover efficiency, incorporating the small molecule delivery with silica nanoparticle[49]. Next, we introduce the carbon-sourced nanoparticle as an improved non-viral gene delivery vehicle and its application to demonstrate the direct reprogramming of human fibroblast into neural stem cell-like form[50].

1.3 Description of Research

1.3.1 Discovery of direct-acting antiviral agents with a graphene-based fluorescent nanosensor

Direct-acting agents against viral components are considered as one of the most promising candidates for the successful antiviral therapeutics. To date, no direct-acting drugs exist for the treatment against dengue virus (DV) infection, which can develop into life-threatening diseases. RNA-dependent RNA polymerase (RdRp), an RNA virus-specific enzyme highly conserved among various viral families, has been known as the broad-range antiviral drug target. Here, we developed an RNA-based graphene biosensor system (RNA-Nano-Graphene Oxide system, RANGO) to enable the fluorescence-based quantitative analysis of the RdRp enzyme activity. We employed the RANGO system to a high-throughput chemical screening to identify novel direct-acting antiviral drug candidates targeting DV RdRp from the FDA-approved small molecule library. RANGO accelerated the massive selection of the drug candidates. We found that one of the selected hit compounds, montelukast, clearly showed anti-viral activity in vitro and in vivo by directly inhibiting replication of DV and thus relieved related symptoms.

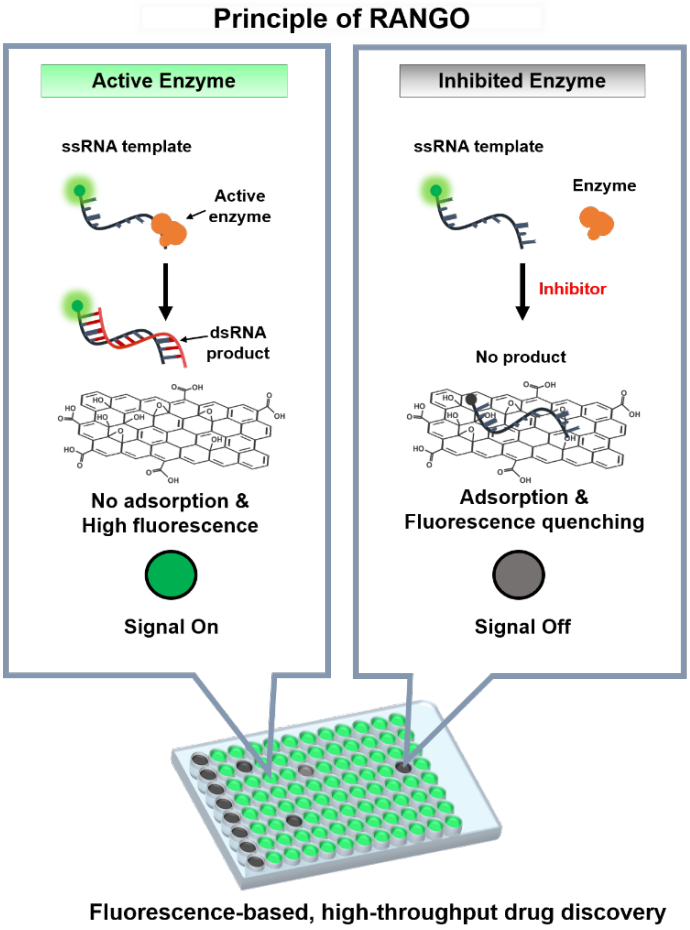

Scheme 1.1 Strategy for the development of the RANGO system for high-throughput screening of anti-viral drug candidates.

1.3.2 Highly efficient and rapid neural differentiation of mouse embryonic stem cells based on retinoic acid encapsulated porous nanoparticle

An improved cell conversion strategy for neural differentiation of mouse embryonic stem (mES) cells is developed by incorporating functionalized mesoporous silica nanoparticle (MSN) as an efficient delivery carrier of retinoic acid (RA), which is pleiotropic factor required for initiation of neural differentiation. Traditional RA-mediated neural differentiation methods required either pre-activation of the cells to the differentiating state by embryoid body (EB) formation or repetitive treatment of the differentiation factor. Our modified cell conversion system involves only singular treatment of RA/MSN complex, which simplified the whole process and accelerated neural induction to be finished within 6 days with high quality. With our new method, neural cells were successfully derived from mES cells with stable expression of neurite marker gene.

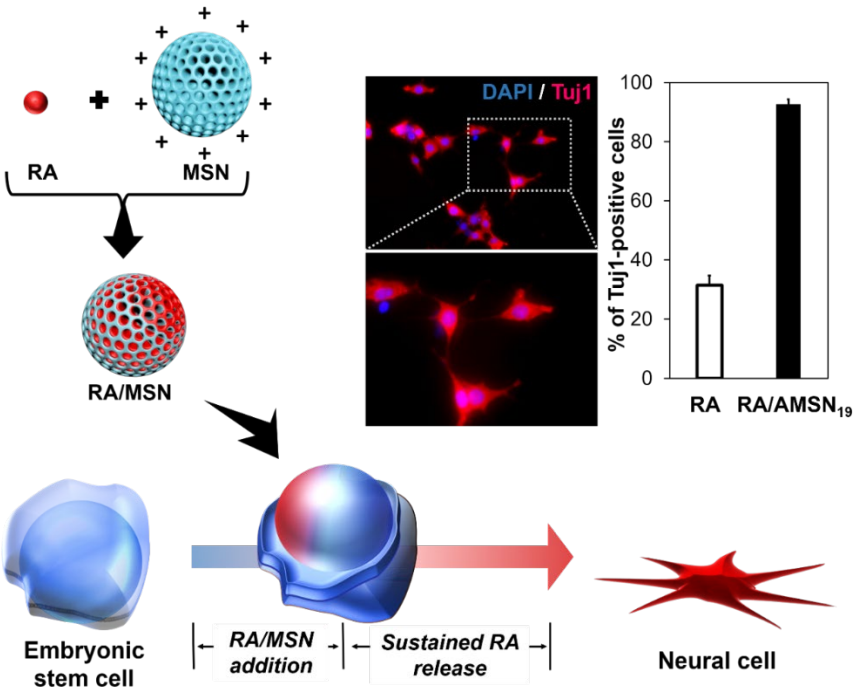

Scheme 1.2 Strategy for the efficient neural differentiation of mouse embryonic stem cell incorporating the porous silica nanoparticle.

1.3.3 Non-viral, direct neuronal reprogramming from human fibroblast using a polymer-functionalized nanodot

Among various strategies to treat neurodegenerative disorders, cell replacement therapies have drawn much attention recently. Such a trend led to the increase in demand for the rare and specialized cells, followed by the outburst development of various cell reprogramming strategies. However, several limitations on these conventional methods remain to be solved, including the genetic instability of the viral vectors and the high cytotoxicity or poor performance of the non-viral carriers. Therefore, non-viral methods need to be developed to ensure safe and efficient cell reprogramming. Here, we introduce a polymer-modified nano-reagent (Polymer-functionalized Nanodot, PolyN) for the safe and efficient, non-viral direct cell reprogramming. PolyN facilitated the highly efficient contemporary overexpression of the transgene compared to the conventional reagent. With our nano-reagent, we demonstrated the SOX2-mediated cell reprogramming and successfully generate the neuron-like cell from the human fibroblast.

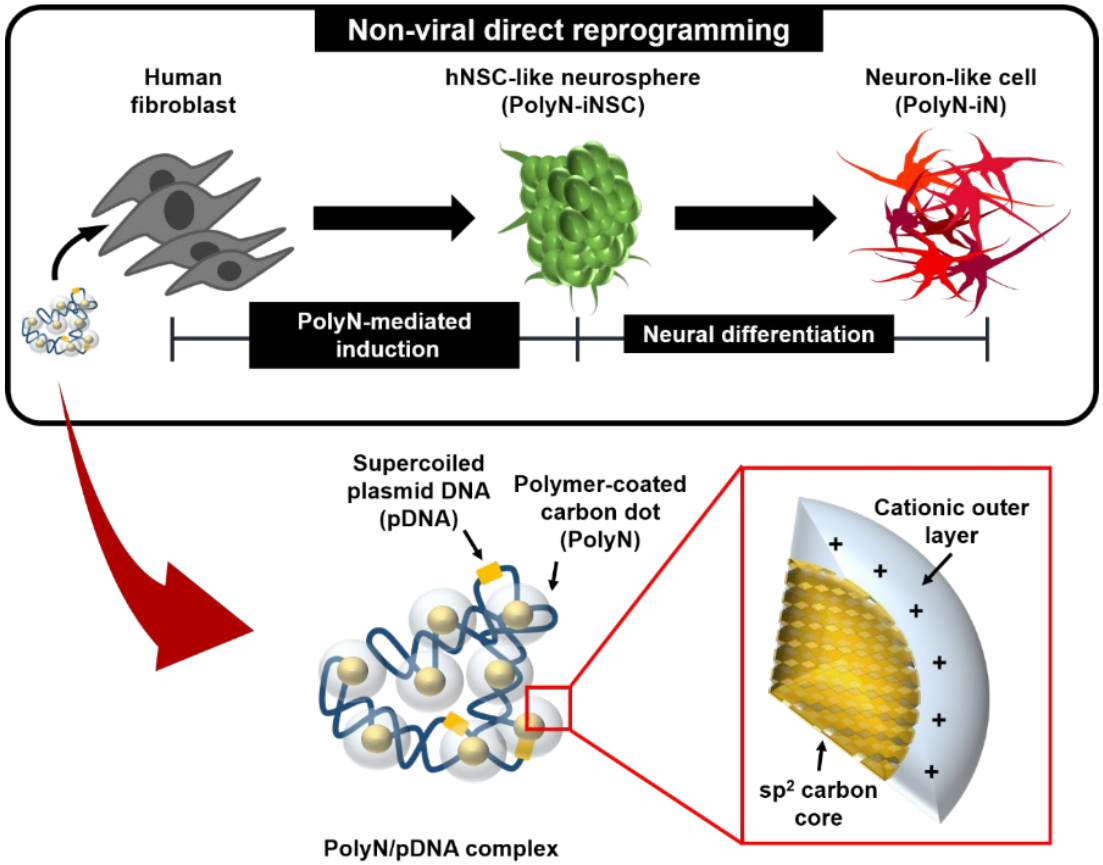

Scheme 1.3 Non-viral strategy for the direct reprogramming of human fibroblast to neural stem cell-like cell incorporating biocompatible polymer-functionalized carbon nanodot

1.4 Reference

1. Jones, K. E.; Patel, N. G.; Levy, M. A.; Storeygard, A.; Balk, D.; Gittleman, J. L.; Daszak, P., *Nature* **2008,** *451* (7181), 990-993.

2. Kilbourne, E. D., *Emerg Infect Dis* **2006,** *12* (1), 9-14.

3. Li, K. S.; Guan, Y.; Wang, J.; Smith, G. J.; Xu, K. M.; Duan, L.; Rahardjo, A. P.; Puthavathana, P.; Buranathai, C.; Nguyen, T. D.; Estoepangestie, A. T.; Chaisingh, A.; Auewarakul, P.; Long, H. T.; Hanh, N. T.; Webby, R. J.; Poon, L. L.; Chen, H.; Shortridge, K. F.; Yuen, K. Y.; Webster, R. G.; Peiris, J. S., *Nature* **2004,** *430* (6996), 209-13.

4. Ferguson, N. M.; Cummings, D. A.; Fraser, C.; Cajka, J. C.; Cooley, P. C.; Burke, D. S., *Nature* **2006,** *442* (7101), 448-52.

5. Webster, R. G.; Bean, W. J.; Gorman, O. T.; Chambers, T. M.; Kawaoka, Y., *Microbiol Rev* **1992,** *56* (1), 152-79.

6. Fraser, C.; Donnelly, C. A.; Cauchemez, S.; Hanage, W. P.; Van Kerkhove, M. D.; Hollingsworth, T. D.; Griffin, J.; Baggaley, R. F.; Jenkins, H. E.; Lyons, E. J.; Jombart, T.; Hinsley, W. R.; Grassly, N. C.; Balloux, F.; Ghani, A. C.; Ferguson, N. M.; Rambaut, A.; Pybus, O. G.; Lopez-Gatell, H.; Alpuche-Aranda, C. M.; Chapela, I. B.; Zavala, E. P.; Guevara, D. M.; Checchi, F.; Garcia, E.; Hugonnet, S.; Roth, C., *Science* **2009,** *324* (5934), 1557-61.

7. Jain, S.; Kamimoto, L.; Bramley, A. M.; Schmitz, A. M.; Benoit, S. R.; Louie, J.; Sugerman, D. E.; Druckenmiller, J. K.; Ritger, K. A.; Chugh, R.; Jasuja, S.; Deutscher, M.; Chen, S.; Walker, J. D.; Duchin, J. S.; Lett, S.; Soliva, S.; Wells, E. V.; Swerdlow, D.; Uyeki, T. M.; Fiore, A. E.; Olsen, S. J.; Fry, A. M.; Bridges, C. B.; Finelli, L., *N Engl J Med* **2009,**

361 (20), 1935-44.

8. Smith, G. J.; Vijaykrishna, D.; Bahl, J.; Lycett, S. J.; Worobey, M.; Pybus, O. G.; Ma, S. K.; Cheung, C. L.; Raghwani, J.; Bhatt, S.; Peiris, J. S.; Guan, Y.; Rambaut, A., *Nature* **2009,** *459* (7250), 1122-5.

9. Dye, C.; Team, W. H. O. E. R., *The New England journal of medicine* **2015,** *372* (2), 189.

10. Feldmann, H.; Geisbert, T. W., *Lancet* **2011,** *377* (9768), 849-62.

11. Tumpey, T. M.; Basler, C. F.; Aguilar, P. V.; Zeng, H.; Solórzano, A.; Swayne, D. E.; Cox, N. J.; Katz, J. M.; Taubenberger, J. K.; Palese, P.; García-Sastre, A., *Science* **2005,** *310* (5745), 77-80.

12. Anderson, R. M.; Fraser, C.; Ghani, A. C.; Donnelly, C. A.; Riley, S.; Ferguson, N. M.; Leung, G. M.; Lam, T. H.; Hedley, A. J., *Philos Trans R Soc Lond B Biol Sci* **2004,** *359* (1447), 1091-105.

13. Al-Omari, A.; Rabaan, A. A.; Salih, S.; Al-Tawfiq, J. A.; Memish, Z. A., *Diagnostic microbiology and infectious disease* **2019,** *93* (3), 265-285.

14. Mehrjardi, M. Z., *Virology (Auckl)* **2017,** *8*, 1178122X17708993-1178122X17708993.

15. Abd El-Aziz, T. M.; Stockand, J. D., *Infection, Genetics and Evolution* **2020,** *83*, 104327.

16. Harapan, H.; Itoh, N.; Yufika, A.; Winardi, W.; Keam, S.; Te, H.; Megawati, D.; Hayati, Z.; Wagner, A. L.; Mudatsir, M., *Journal of Infection and Public Health* **2020,** *13* (5), 667-673.

17. Sun, H.; Xiao, Y.; Liu, J.; Wang, D.; Li, F.; Wang, C.; Li, C.; Zhu, J.; Song, J.; Sun, H.; Jiang, Z.; Liu, L.; Zhang, X.; Wei, K.; Hou, D.; Pu, J.; Sun, Y.; Tong, Q.; Bi, Y.; Chang, K.-C.; Liu, S.; Gao, G. F.; Liu, J., *Proceedings of the National Academy of Sciences* **2020**, 201921186.

18. Feyman, R., *California: California Institute Of Technology* **1960**.

19. Gansukh, E.; Anthonydhason, V.; Jung, S.; Kim, D.; Muthu, M.; Gopal, J.; Chun, S., *Including Nanoclusters and Nanoparticles* **2018,** *29* (6), 933-941.

20. Zehbe, I.; Hacker, G. W.; Su, H.; Hauser-Kronberger, C.; Hainfeld, J. F.; Tubbs, R., *The American journal of pathology* **1997,** *150* (5), 1553.

21. Novoselov, K. S.; Geim, A. K.; Morozov, S. V.; Jiang, D.; Zhang, Y.; Dubonos, S. V.; Grigorieva, I. V.; Firsov, A. A., *Science* **2004,** *306* (5696), 666-9.

22. Allen, M. J.; Tung, V. C.; Kaner, R. B., *Chem Rev* **2010,** *110* (1), 132-45.

23. Kim, K. S.; Zhao, Y.; Jang, H.; Lee, S. Y.; Kim, J. M.; Kim, K. S.; Ahn, J. H.; Kim, P.; Choi, J. Y.; Hong, B. H., *Nature* **2009,** *457* (7230), 706-10.

24. Liu, Y.; Dong, X.; Chen, P., *Chem Soc Rev* **2012,** *41* (6), 2283-307.

25. Choi, W.; Lahiri, I.; Seelaboyina, R.; Kang, Y. S., *Critical Reviews in Solid State and Materials Sciences* **2010,** *35* (1), 52-71.

26. Lu, C. H.; Yang, H. H.; Zhu, C. L.; Chen, X.; Chen, G. N., *Angew Chem Int Ed Engl* **2009,** *48* (26), 4785-7.

27. Zhu, Y.; Murali, S.; Cai, W.; Li, X.; Suk, J. W.; Potts, J. R.; Ruoff, R. S., *Advanced Materials* **2010,** *22* (35), 3906-3924.

28. Joshi, S. R.; Sharma, A.; Kim, G. H.; Jang, J., *Materials Science & Engineering C-Materials for Biological Applications* **2020,** 108.

29. Park, S. J.; Kim, J.; Kang, S.; Cha, H. J.; Shin, H.; Park, J.; Jang, Y. S.; Woo, J. S.; Won, C.; Min, D. H., *Sci Adv* **2020**, *6 (22)*, eaaz8201.

30. Thomas, E. D.; Lochte, H. L., Jr.; Cannon, J. H.; Sahler, O. D.; Ferrebee, J. W., *J Clin Invest* **1959,** *38*, 1709-16.

31. Tabata, Y., *Reprod Biomed Online* **2008,** *16* (1), 70-80.

32. Barbash, I. M.; Chouraqui, P.; Baron, J.; Feinberg, M. S.; Etzion, S.; Tessone, A.; Miller, L.; Guetta, E.; Zipori, D.; Kedes, L. H.; Kloner, R. A.; Leor, J., *Circulation* **2003,** *108* (7), 863-8.

33. Welsch, C. A.; Rust, W. L.; Csete, M., *Stem Cells Transl Med* **2019,** *8* (3), 209-214.

34. Olson, J. L.; Atala, A.; Yoo, J. J., *Chonnam Med J* **2011,** *47* (1), 1-13.

35. Seow, Y.; Wood, M. J., *Mol Ther* **2009,** *17* (5), 767-777.

36. Howe, S. J.; Mansour, M. R.; Schwarzwaelder, K.; Bartholomae, C.; Hubank, M.; Kempski, H.; Brugman, M. H.; Pike-Overzet, K.; Chatters, S. J.; De Ridder, D., *The Journal of clinical investigation* **2008,** *118* (9).

37. Ramamoorth, M.; Narvekar, A., *J Clin Diagn Res* **2015,** *9* (1), GE01-GE6.

38. Patra, J. K.; Das, G.; Fraceto, L. F.; Campos, E. V. R.; Rodriguez-Torres, M. D. P.; Acosta-Torres, L. S.; Diaz-Torres, L. A.; Grillo, R.; Swamy, M. K.; Sharma, S.; Habtemariam, S.; Shin, H.-S., *J Nanobiotechnology* **2018,** *16* (1), 71-71.

39. Martinelli, M.; Strumia, M. C., *Molecules* **2017,** *22* (2).

40. Durymanov, M.; Reineke, J., *Frontiers in Pharmacology* **2018,** *9* (971).

41. Ma, B.; Zhang, S.; Jiang, H.; Zhao, B.; Lv, H., *J Control Release* **2007,** *123* (3), 184-94.

42. Szule, J. A.; Fuller, N. L.; Rand, R. P., *Biophys J* **2002,** *83* (2), 977-84.

43. Zhu, L.; Lu, Y.; Miller, D. D.; Mahato, R. I., *Bioconjug Chem* **2008,** *19* (12), 2499-512.

44. Zhu, L.; Mahato, R. I., *Expert Opin Drug Deliv* **2010,** *7* (10), 1209-1226.

45. de Dios, A. S.; Díaz-García, M. E., *Anal Chim Acta* **2010,** *666* (1-2), 1-22.

46. Ren, Q.; Ga, L.; Lu, Z.; Ai, J.; Wang, T., *Materials Chemistry Frontiers*

2020, *4* (6), 1569-1585.

47. Riley, M. K.; Vermerris, W., *Nanomaterials (Basel)* **2017,** *7* (5), 94.

48. Xiao, Y.; Shi, K.; Qu, Y.; Chu, B.; Qian, Z., *Mol Ther Methods Clin Dev* **2019,** *12*, 1-18.

49. Park, S. J.; Kim, S.; Kim, S. Y.; Jeon, N. L.; Song, J. M.; Won, C.; Min, D. H., *ACS Appl Mater Interfaces* **2017,** *9* (40), 34634-34640.

50. Park, S.-J.; Shin, H.; Won, C.; Min, D.-H., *Nanomedicine: Nanotechnology, Biology and Medicine* **2021,** *32*, 102316.

Chapter 2. Discovery of direct-acting antiviral agents with a graphene-based fluorescent nanosensor

2.1 Introduction

Acceleration of the global outbreak of viral diseases has been an inevitable event recently, due to the rapid climate change and frequent intercontinental travel[1]. Dengue virus (DV) is one of the most prevalent arthropod-borne viral pathogens that belongs to the family of *Flaviviridae*, which consists of Zika and West Nile viruses. Currently, about 390 million people get infected by DV annually and as many as 4 billion people are at risk of potential DV infections worldwide[2]. DV infection can progress into severe diseases such as hemorrhagic fever and dengue shock syndrome, which could be life-threatening with symptoms of rapid decline in platelet counts and severe bleeding. However, there is no specific medicine to treat dengue infection other than pain-relievers such as acetaminophen and supportive care in a hospital.

Non-selective, broad-spectrum antivirals such as interferon-γ and ribavirin are infamous for serious adverse effects including seizures and hemolytic anemia[3]. Therefore, it is important to develop direct-acting antivirals to treat specific virus infections to increase therapeutic efficacy with fewer adverse effects. Strategies to develop direct-acting antiviral drugs have drawn much attention to deal with such viruses, which focused on targeting the virus-originated components such as enzymes associated with the viral genomic replication[4]. The main goal of such approach is to reduce the viral load circulating the whole body and therefore shorten the duration of the febrile illness[5]. While partial progress has been made against several flaviviruses such as HCV[6], yet there has not been successful

development of the direct-acting antiviral therapeutics available against DV. Although several antiviral drug candidates had entered the clinical trials against DV[7, 8], they failed to show sufficient viremia reduction or NS1 antigen clearance. Considering the rapid spread-out of the viral outbreak, it is urgent to come up with strategies to accelerate the antiviral drug discovery.

To date, conventional *in vitro* assays designed for the antiviral drug discovery has mainly focused on the identification of the target-independent antiviral activities which were restricted to the cell-based assays incorporating either live virus[9-11], artificial virus-like components such as viral subgenomic replicons[12] or their mimics[13]. Such methods are limited to the evaluation of the antiviral efficacy or the partial inhibitory effect associated with the viral replication cycle, which is not well-suited for high throughput screening of direct-acting antiviral drug candidates against virus-specific biomolecular targets. In addition, such methods require high cost, intensive labor and complicated procedures.

Among the various RNA-virus specific enzyme, RNA-dependent RNA polymerase (RdRp) has drawn extraordinary attention as the direct-acting antiviral drug target, for its critical function associated with the viral genome replication and high structural conservation across numerous RNA viruses[14]. However, only very limited methods exist which are compatible with high-throughput screening to discover RdRp inhibitors as direct-acting antiviral agents. Conventional RdRp assays include gel electrophoresis or radioactive labels, which are not compatible with high throughput screening due to laborious procedures and high cost.

Recent reports have also depicted fluorescence-based RdRp activity analyzing strategy, by introducing a nucleic acid intercalating dye to distinguish double-

strand RNA (dsRNA, product of the enzyme activity) from single-strand RNA (ssRNA, enzyme substrate). Due to its simple tactics, there have been some efforts to perform high-throughput screening with this method[15]. However, the method itself has not been inspected for its validity and suitability as the high-throughput screening. Thus, it is yet questionable that such method guarantees the reproducibility and reliability of the screened drug candidates. Moreover, there are several concerns to be clarified when using the intercalating dye, including the possibility of the signal interference by the various component other than pure nucleic acid (such as the presence of the enzyme protein, cofactor metal ions, etc.), which may lead to false signals.

Meanwhile, graphene oxide (GO), a two-dimensional carbon-based nanomaterial possessing oxygen-containing functional groups, has been proven its unique features suitable for sensor development. Such properties include the capability of various surface functionalization chemistry, controllable selectivity towards single-stranded nucleotides, and fluorescence quenching ability[16, 17]. Due to its conspicuous characteristics, GO has been utilized for various fluorescence-based biosensors[18-20] with high specificity. However, only very limited examples of GO-based sensors have been reported for the application to high-throughput screening for antiviral drug discovery.

Here, we developed a selective quenching fluorescent nanosensor (**R**N**A**-**N**ano-**G**raphene **O**xide system, abbreviated as **RANGO**) to enable the quantitative analysis of the DV RdRp activity and its application to the high-throughput chemical screening for the rapid discovery of the viral RdRp inhibitor candidates (Scheme 2.1). With high specificity and robustness of GO, RANGO was experimentally validated with its reliability as the high-throughput screening

platform. As a result of the RANGO-based, extensive screening against 2,400 FDA-approved drug library, we selected an RdRp inhibitor candidate which showed the highest RNA replication inhibitory property. Throughout the series of cell and animal-based evaluation, we suggest montelukast, primarily known as a leukotriene antagonist, could function as an antiviral drug candidate against DV by directly inhibiting the viral replication.

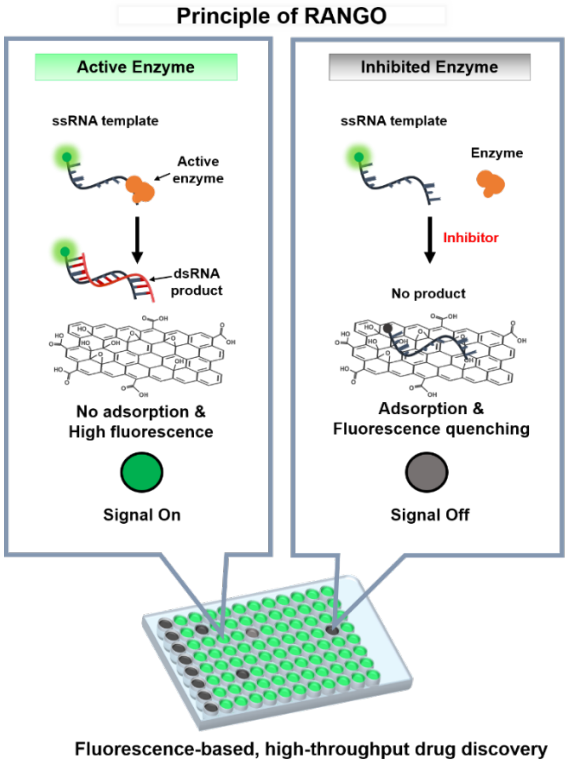

Scheme 2. 1 Strategy for the development of RANGO system for high-throughput screening of anti-viral drug candidates.

2.2 Result

We first developed the RdRp activity analysis technology named as RANGO based on the detection of the difference in the fluorescence signal which is proportional to the concentration of the newly synthesized RNA product mediated by active RdRp. The RANGO system consists of the recombinant DV RdRp, its target RNA template conjugated with a fluorescent dye, and nano-sized graphene oxide (NGO) as a selective quencher (Figure 2.1). In the RANGO system, NGO plays its role as a quencher of the fluorescence from the dye conjugated to the RNA template. The interaction between NGO and RNA is highly dependent on the structure of the substrate. In general, it is known that the interaction of NGO with the ssRNA is much stronger than that of the dsRNA[21]. The strong interaction between NGO and ssRNA is based on π-π stacking interaction and hydrogen bonding, resulting in a sufficiently short distance which induces NGO-mediated quenching of the fluorescence. When the active RdRp synthesizes a complementary RNA sequence against the template RNA, the two RNA strands form a double-stranded structure. Then, nucleobases in the double-stranded RNA are hidden inside the helical structure, which decreases the chance of the intermolecular hydrogen bonding between NGO and RNA bases. Such phenomena lead to inhibition of the fluorescence quenching that could be induced by close interaction of RNA with NGO.

We synthesized NGO by using a modified Hummers' method[19], which showed characteristic height and dimension profile corresponding to the nano-sheet form of GO in AFM analysis (Figure 2.1A, B). As shown in the IR spectra, the nanostructure consisted of the oxygen functional groups corresponding to each characteristic peak (Figure 2.1C). Altogether with Raman spectra analysis showing the co-existence of D- and G-band (Figure 2.1D), the overall analytical

data indicate the successful synthesis of NGO.

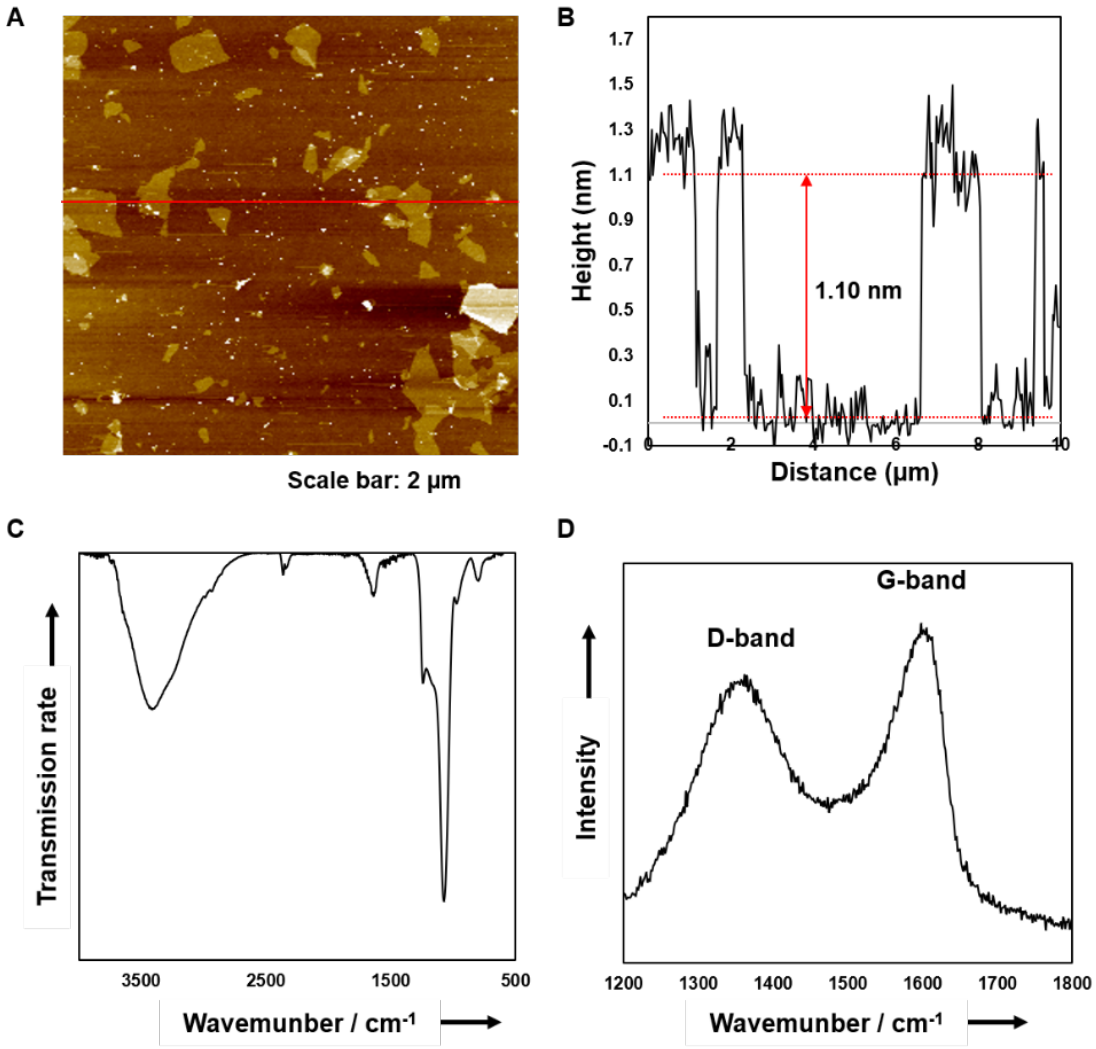

Figure 2.2.1 Characterization of GO. (a) AFM image of GO and (b) corresponding height and dimension profile of GO. (c) IR spectra of GO which clearly shows the peaks corresponding to the oxygen functional groups. (d) Raman spectra of GO showing the co-existence of D-band and G-band, which indicates the formation of GO.

For the preparation of RNA template specific to DV RdRp, overall structure, size, and the specific sequence motifs were considered. Specifically, the template was designed to include the seed sequence motif derived from 3'UTR or 5'UTR of DV genome to guide the activation of RdRp[14]. The inclusion of the secondary structure was not favorable, as the presence of the non-linear conformation in the RNA can lead to the significant decrease of the interaction between the substrate

RNA itself and NGO. Such phenomena would induce the failure of the quenching of the fluorescence conjugated to the template, resulting in the false signal. In this regard, the RNA template was designed to exclude any secondary structure (Figure 2.2A).

Recombinant DV NS5 RdRp enzyme was obtained *via* the mammalian expression system. The obtained RdRp showed the expected replication activity against the designed template RNA under the appropriate buffer condition, including divalent cations (Mg^{2+} and Mn^{2+}) at specific NTP ratio of ATP:CTP:UTP:GTP=1:5:5:5 with pH 7.5 HEPES buffer (Figure 2.2B). In the development of RANGO, it was critical to confirm the optimal range of NGO content to ensure the selective quenching property against ssRNA (representing the unreacted substrate) over dsRNA (representing the product by enzyme). The quenching capability of NGO in various concentrations was investigated in presence of either fluorescence-conjugated ssRNA or the complementary dsRNA (Figure 2.2C). The fluorescence intensity was measured individually for each concentration of NGO. To determine the optimal NGO concentration with the highest selective quenching capability, the difference of the fluorescence intensity (ΔFL) between in presence of ssRNA and that of dsRNA was calculated (Figure 2.2D). It was identified that the appropriate concentration of NGO is 1.5 μg/mL for the optimized RANGO system, which showed the highest selective quenching ability toward ssRNA over dsRNA.

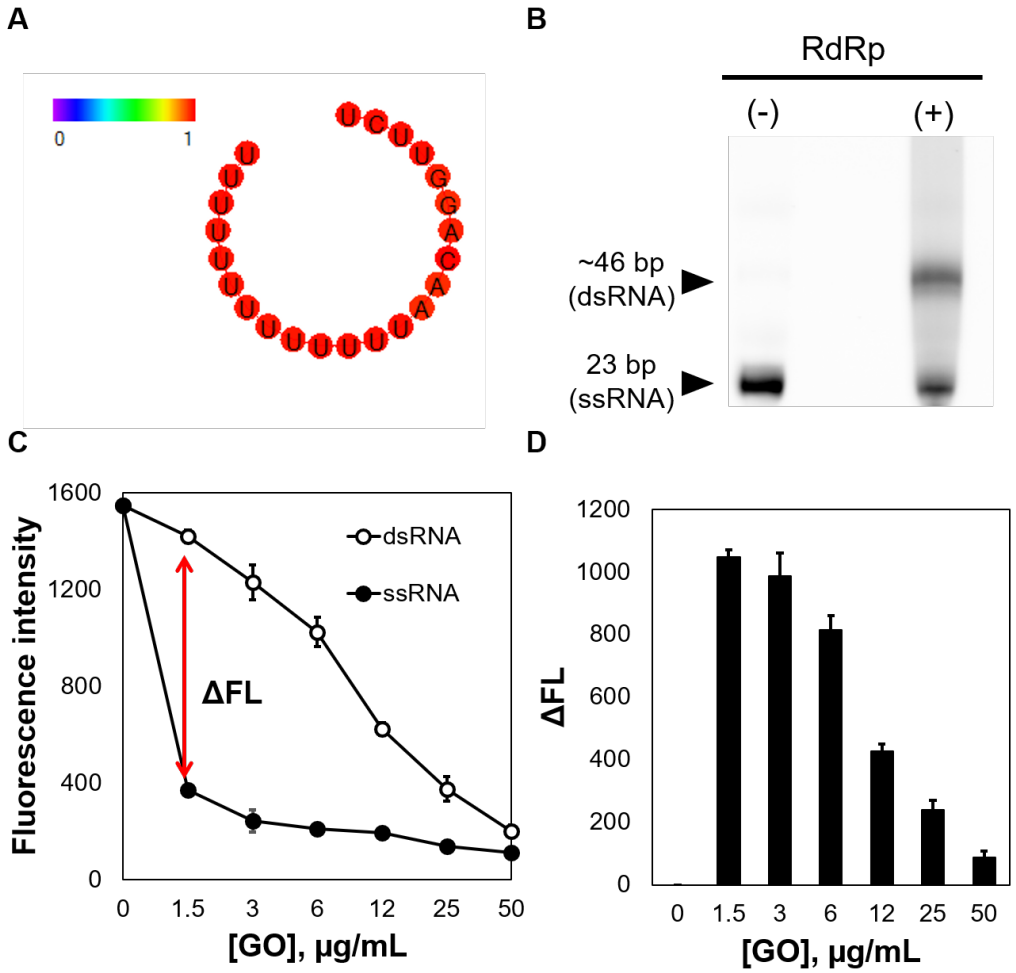

Figure 2. 2 Optimization of the RANGO system. (A) Target substrate design specific for DV serotype 2 RdRp. The color scale represents the probability of each nucleotide (from blue to red, probability increases from 0 to 1), which is used to determine the possibility of the linearity or any chance of the internal secondary structural formation. The substrate was designed to not to generate secondary structures simultaneously. (B) Enzyme activity of the model RdRp protein, induced by adding 3 pmole of RNA substrate, 3.5 pmole DV2 RdRp and 0.1 mM ATP, 0.5 mM C/U/GTP in the RdRp buffer. The lower band (22bp) represents the ssRNA, and the upper band (~46 bp) is assumed to be the dsRNA, synthesized by RdRp. (C) NGO concentration-dependent quenching test against the fluorescence dye conjugated to the substrate, to derive the optimal concentration. The original single-strand RNA (ssRNA) represents the enzyme substrate, while the corresponding double strand RNA (dsRNA) represents the mimic of the polymerization product by enzyme. The red arrow indicates the difference of the fluorescence intensity (Δ FL) between the measured value of the fluorescence dye conjugated to ssRNA and that of dsRNA in presence of GO at each point. Bars indicate mean ± SEM, from three individual groups for each concentration (n=3). (D) Determination of the quenching efficiency of GO by analyzing the ΔFL at each concentration of GO. Bars indicate mean ± SEM, from three individual groups for each concentration (n=3).

To determine whether the practical operation of the RANGO system is valid,

we prepared two RdRp buffer groups in the solution phase, which consisted of either active RdRp and inactivated RdRp. The samples were incubated under same condition required for the enzyme activity induction, and then the NGO was added to each sample in the optimized concentration. A simple fluorescence measurement revealed the distinct difference of the fluorescence intensity between the group of active RdRp and that of inactive RdRp (Figure 2.3), indicating the capability of RANGO for the fluorescence based RdRp activity analysis.

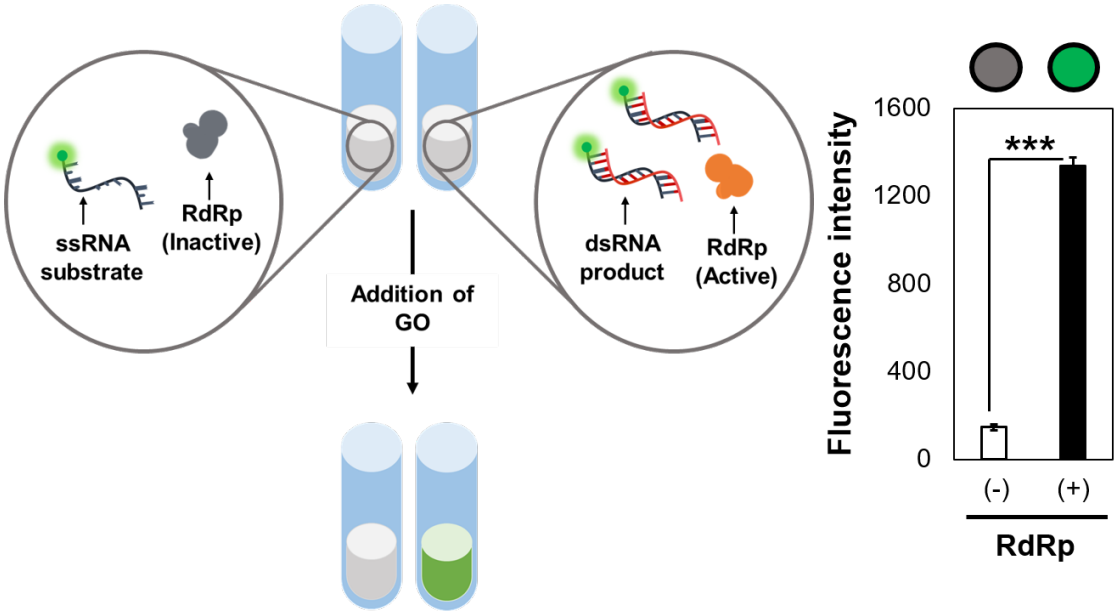

Figure 2. 3 Schematic illustration of the RANGO-based RdRp assay platform (left) and its corresponding data depicting the difference of the fluorescence intensity between inactive RdRp and active RdRp (right). Bars indicate mean ± SEM, from three individual experiments for each group (n=3). To determine the significance of the data, Student's *t*-test was performed to derive *p*-value. *** indicates a significance in the change compared to the inactive RdRp control; *** for $p \leq 0.001$.

Followed by the preliminary demonstration of the RANGO system, the platform was validated with its suitability for the high-throughput enzyme inhibitor screening assay. As the determinant standard for the reliability of assay, Z'-factor was derived against the RANGO system. Z'-factor is a generally accepted parameter used for system evaluation to determine the quality of high-throughput

assay platform, of which 0.75 or higher value indicates a robust assay suitable for high-throughput screening[22]. Z'-factor of the RANGO system was calculated as 0.79, suggesting that the system is reliable and suitable as a high-throughput assay (Figure 2.4A). To confirm its validity for the quantitative enzyme inhibition analysis, an inhibition assay was performed with a previously known RdRp inhibitor (aurintricarboxylic acid, ATA[23]) based on RANGO. With RANGO system, we observed the inhibitor concentration-dependent decrease of the fluorescence signal intensity, indicating that the system enabled the quantitative analysis of the model inhibitor in a dose-dependent manner (Figure 2.4B).

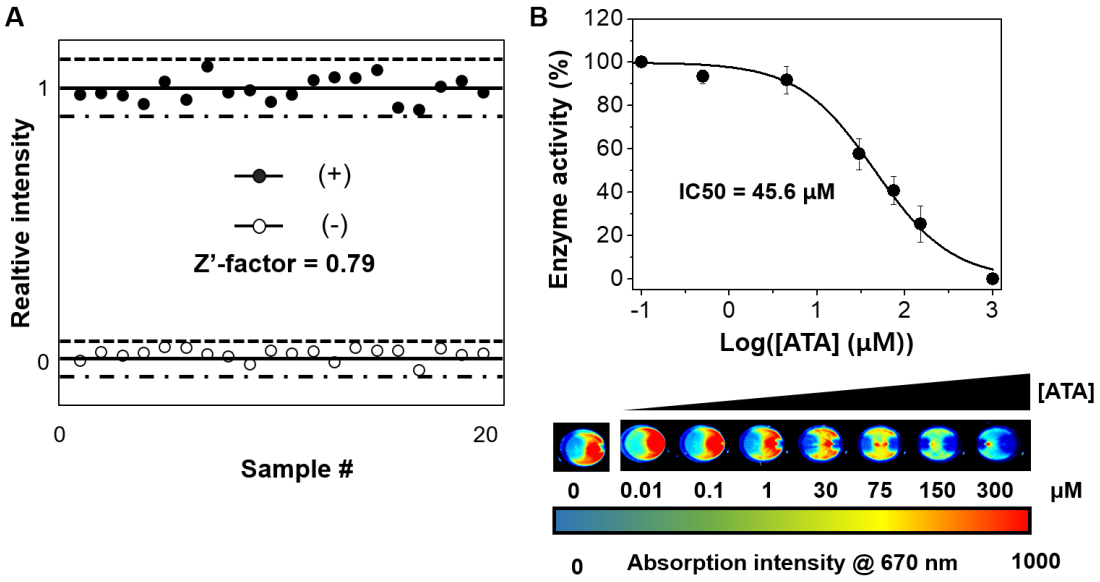

Figure 2. 4 Validation of RANGO for the application to high-throughput RdRp inhibitor screening. (A) Significance of RANGO as a screening platform, calculated as Z'-factor against the 20 individual replications (n=20). (B) Fluorescence-based quantitative analysis of the representative enzyme inhibitor activity demonstrated with RANGO system. Aurintricarboxylic acid (ATA) was used as a model enzyme inhibitor. Bars indicate mean ± SEM, from three individual groups for each concentration (n=3).

Prior to the main screening, the performance of RANGO was compared with the conventional gel-based RdRp activity assay. A random chemical library

consisted of 80 analytes was examined by their RdRp inhibitory effect by using either RANGO or the gel-based RNA assay. Under the experimental condition of using 96-well, black-bottom plate, a single round of RANGO-based analysis was capable of the evaluation of all the analytes in 5~10 minutes. On the contrary, a single round of the conventional gel-based RNA assay allowed up to ~20 chemicals and required approximately an hour (which is the summation of the time demanded for the sample transfer to gels, electrophoresis, staining, and measurement). As a result, it took roughly ~4 hours to analyze the same numbers of analytes with the typical gel-based assay. Such comparison indicates that the utilization of RANGO system could significantly reduce the time and labor required for the screening process (Figure 2.5).

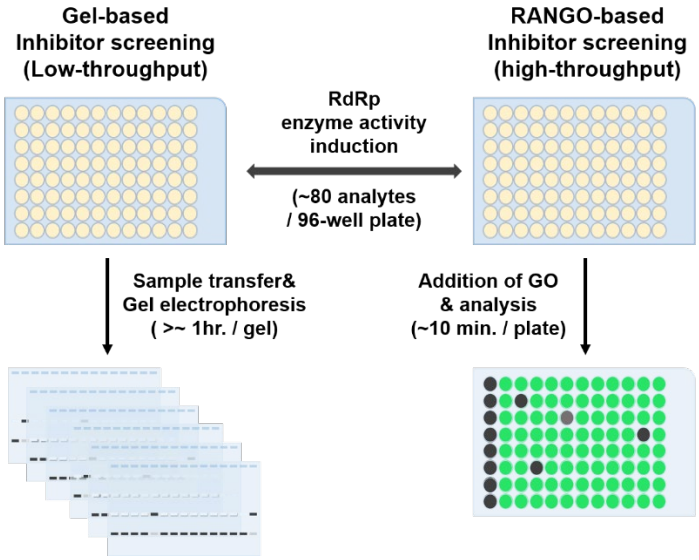

Figure 2. 5 Schematic comparison of the performance as the inhibitor drug screening platform between the conventional gel-based RNA assay and RANGO-based RdRp assay.

With regard to the previous data, RANGO-based high-throughput RdRp inhibitor screening was performed against FDA-approved chemical library consisting of 2,400 compounds (Figure 2.6). Throughout the first selection from

the screening, we revealed the inhibitor candidate, montelukast, which showed ~ 90% of enzyme inhibitory efficiency at 200 μM, as the most potent RdRp inhibitor.

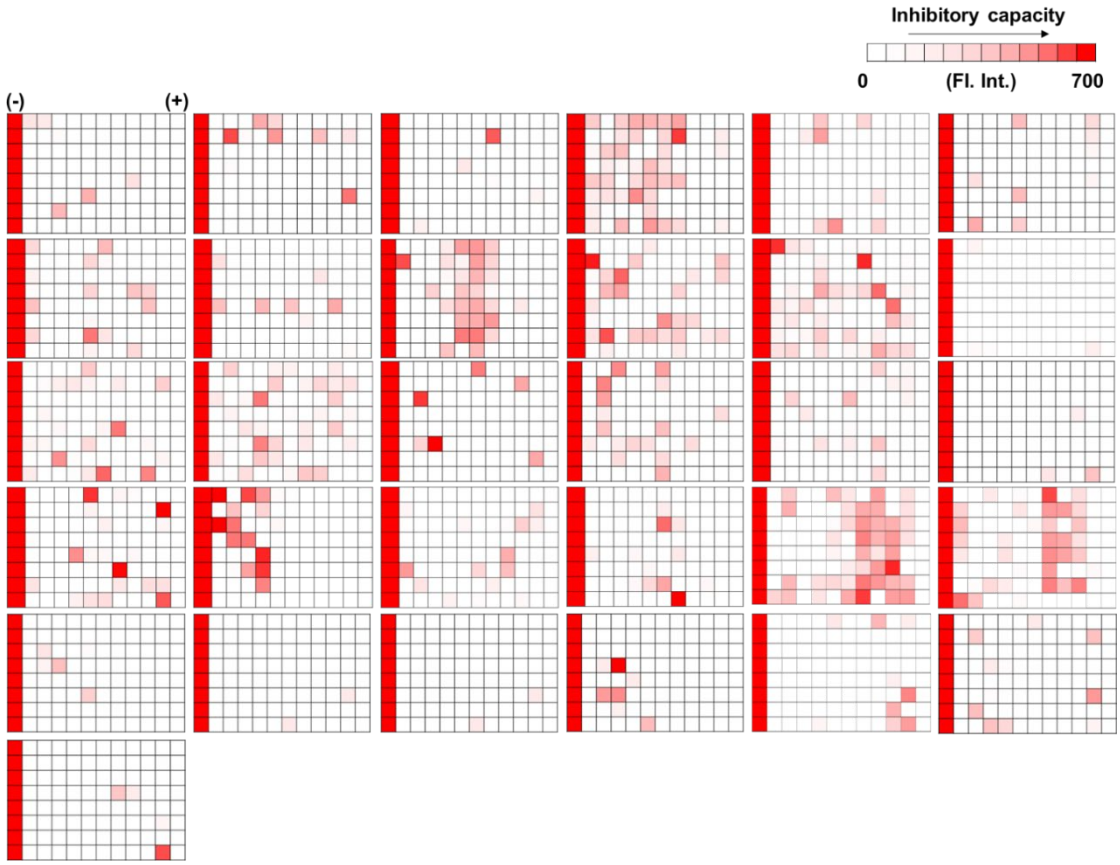

Figure 2. 6 RANGO system enables the high-throughput RdRp inhibitor screening against FDA-approved chemical library. To simplify the analysis, the received data was reversely converted so that the difference in the fluorescence intensity can be easily visualized by the representative color (from white to red, corresponding to 0 to maximum 700, respectively). First lane (symbolized by (-), red) and the last lane (symbolized by (+), white) of each plate represent the negative control (inactive RdRp) and the positive control (active RdRp), respectively.

The inhibitory property of montelukast was then quantitatively measured with various concentrations of montelukast by the RANGO system (Figure 2.7A). The inhibition of RdRp activity by montelukast was revealed as concentration-dependent, showing sigmoidal curve with the calculated half-inhibitory concentration (IC_{50}) of 38.6 μM.

To insist on the practical significance of RANGO to sort out the hit compound

in desire, it was required to prove whether the selected RdRp inhibitor candidate also possessed the potential as an anti-viral agent. We first designed a dose-dependent antiviral efficacy analysis based on focus forming assay (FFA) in a model cell, VeroE6 (monkey kidney cell), infected with DV serotype 2 (Figure 2.7B). Foci is a general unit for viral quantification, which is created by restricting the mobility of virus with semi-solid overlay medium on cells. The focus forming unit (FFU) was calculated individually for each group treated with the serially diluted inhibitor to derive a dose-dependent sigmoidal plot similar to that of the aforementioned enzyme inhibition assay. The half-effective concentration (EC_{50}) for the antiviral function was calculated according to the plot, with value of 5.52 μM. Such data was highly correlative with the relative expression level of the viral RNA genome normalized by the endogenous control (GAPDH), which resulted as a drug concentration-dependent decrease of the viral RNA concentration (Figure 2.7C). In addition, the number of foci, which represents the severity of the viral replication and infection, significantly decreased as the concentration of the treated montelukast increases (Figure 2.7D). The overall data support that montelukast not only functions as a DV RdRp inhibitor but also serves as an antiviral agent by inhibiting DV replication in the virus infection cell model.

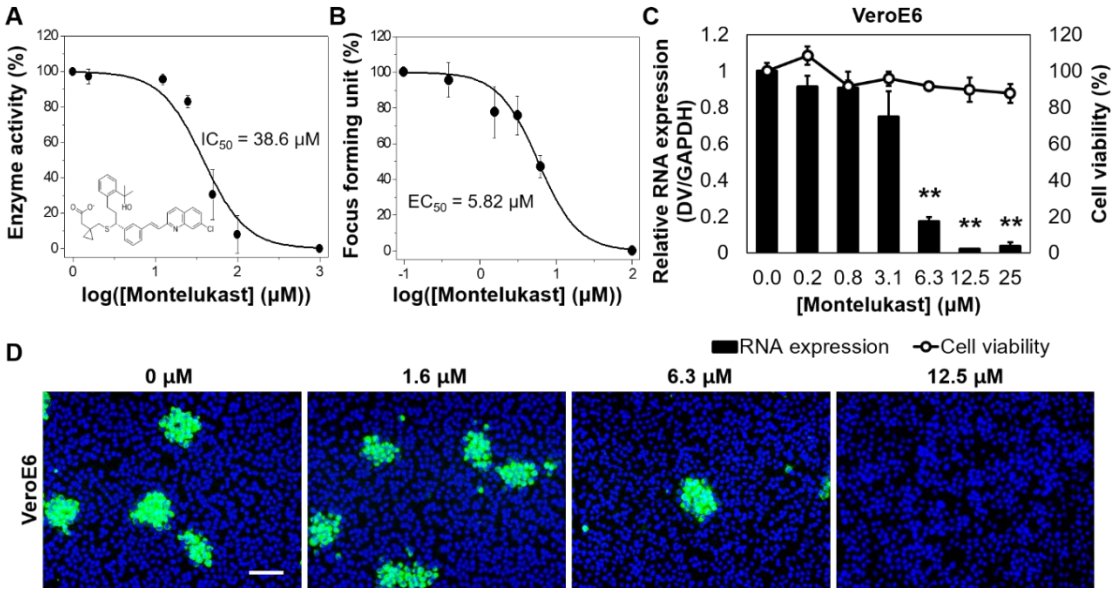

Figure 2. 7 The hit compound, montelukast, shows *in vitro* antiviral therapeutic effect against the DV2-infected cells. (A) Chemical structure of the hit compound, montelukast and investigation of the concentration-dependent enzyme inhibitory effect against DV RdRp via RANGO assay. Dose-responsive sigmoidal curve with the calculated half-inhibitory concentration (IC_{50}) value is shown. Bars indicate mean ± SEM, from four individual groups for each concentration (n=4). (B) Investigation of concentration-dependent antiviral effect on the hit compound *via in vitro* viral focus forming assay on VeroE6 cells. Dose-responsive sigmoidal curve with the calculated half-effective concentration (EC_{50}) value is shown. Bars indicate mean ± SEM, from three individual groups for each concentration (n=3). (C) Semi-quantitative RNA expression analysis on the concentration-dependent antiviral effect of the hit compound and the corresponding cytotoxicity. (D) The corresponding images of the viral focus of those treated with the representative concentration of the hit compound are shown. Bars indicate mean ± SEM, from three independent groups for each concentration (n=3).

To further validate its inhibitory activity against DV replication, we selected two human cell lines, Huh7[24] and A549[25] as hosts for the DV infection. Both cells were first infected with DV serotype 2 and then, treated with the serially-diluted montelukast. As these cells were not prone to the formation of the viral foci, the antiviral efficacy was quantified by the comparison of the viral RNA level (Figure 2.8A). The treatment of the montelukast reduced the viral RNA genome level in both cell lines, dose-dependently. In addition, immuno-staining of the viral NS1 protein also indicated the decrease in viral replication with increasing

concentration of the treated montelukast (Figure 2.8B). Taken together, montelukast effectively reduced DV replication in two human cell lines by showing the significantly reduced level of DV RNA and viral protein NS1 upon treatment of montelukast.

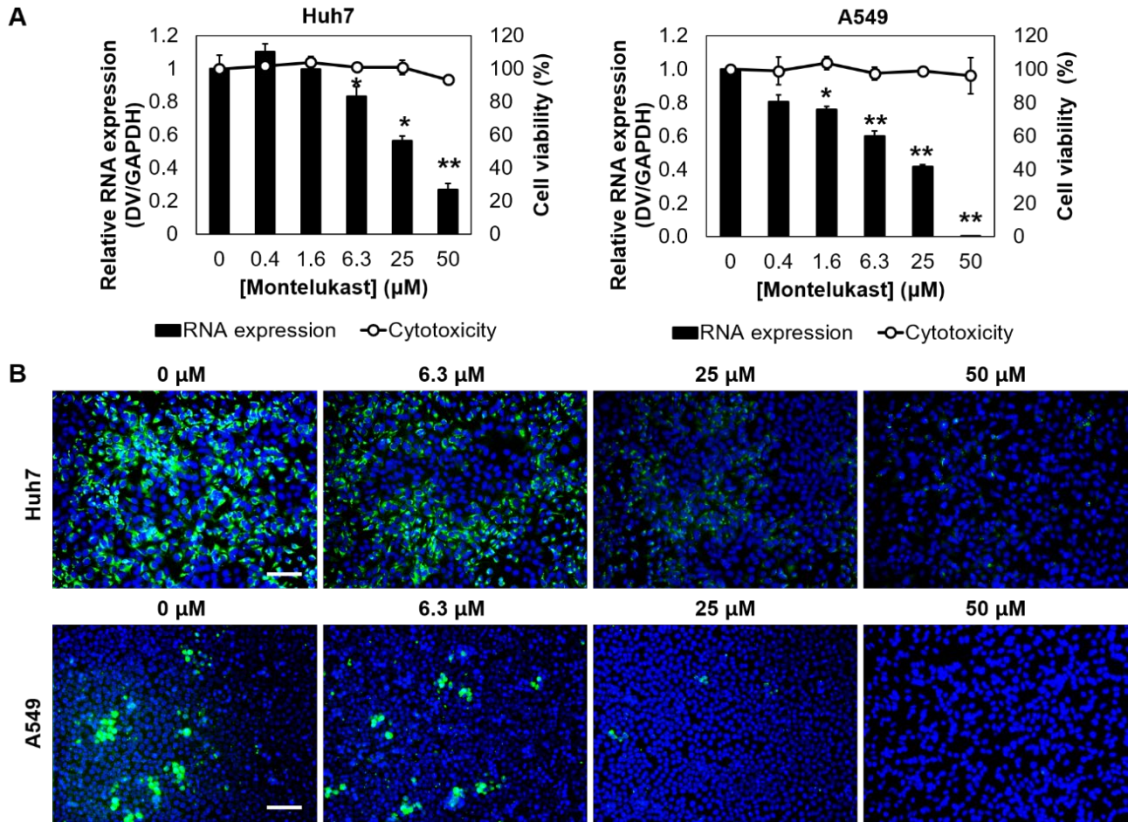

Figure 2. 8 (A) Relative viral RNA expression analysis of the concentration-dependent antiviral effect of the hit compound on the virus-infected human cells. Bars indicate mean ± SEM, from three individual groups for each concentration (n=3). To determine the significance of the data, Student's *t*-test was performed to derive *p*-value. * or ** indicates a significance in the change compared to the vehicle (PBS) control; * for $p \leq 0.05$ and ** for $p \leq 0.01$. (B) Investigation of concentration-dependent antiviral effect on the hit compound via immunocytochemistry on human liver (Huh7) and lung carcinoma (A549) cells. Bars indicate mean ± SEM, from three independent groups for each concentration (n = 3).

Encouraged by the promising data obtained in the cell-based inhibition assays, we next tested the systemic antiviral effect of montelukast *in vivo*. In general, IFNα/β/γR-/- (AG129) mice, a transgenic mouse model highly susceptible to virus infection, widely harnessed for infectious virus research[26, 27]. Nevertheless, the

sensitivity of this model varies among the different DV strains. Since the DV strain we use (KUMC-29) has not been examined for its lethality against the animal model in previous studies, it was required to investigate whether the combination of AG129 and KUMC-29 strain is appropriate for the generation of the 'lethal mouse model' that we desired for the further research. We first examined the correlation between the quantity of the inoculated viral titer and induction of lethality. Viral infection was induced by administration of $1x10^6$, $5x10^6$, and $1x10^7$ FFU of DV serotype 2 by intraperitoneal (IP) injection. According to the evaluation, the virus strain KUMC-29 showed lethality within ~10 days after administration at a dose of ~$1x10^7$ FFU (Figure 2.9). Therefore, we successfully generated the lethal DV infection mouse model by using KUMC-29 DV strain using AG129 mice.

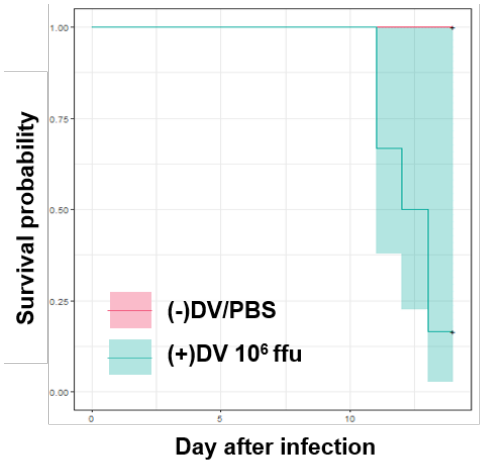

DV infection at 10^6 ffu

Time	Survival	Std.err	95% lower CI	95% upper CI
11	0.6667	0.1925	0.3786	1
12	0.5	0.2041	0.2246	1
13	0.1667	0.1521	0.0278	0.9974

	Chisq	DF	P-value
1	7.9418	1	0.0048

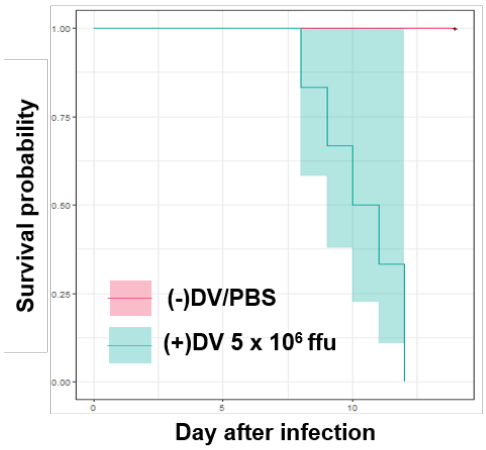

DV infection at 5x 10^6 ffu

Time	Survival	Std.err	95% lower CI	95% upper CI
8	0.8333	0.1521	0.5827	1
9	0.6667	0.1925	0.3786	1
10	0.5	0.2041	0.2246	1
11	0.3333	0.1925	0.1075	1
12	0			

	Chisq	DF	P-value
1	10.8493	1	0.001

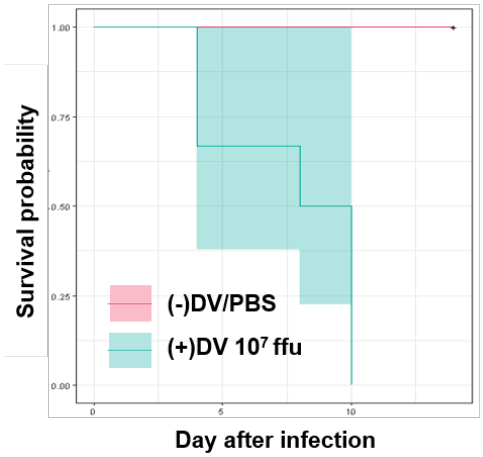

DV infection at 10^7 ffu

Time	Survival	Std.err	95% lower CI	95% upper CI
4	0.6667	0.1925	0.3786	1
8	0.5	0.2041	0.2246	1
10	0	NAN	NA	NA

	Chisq	DF	P-value
1	10.8493	1	0.001

Figure 2. 9 Quantitative lethality analysis of the viral titer-dependent infection on the mouse model against DV serotype2. AG129 mice was administrated with the DV serotype 2 strain KUMC-29 in various titers, to determine the optimal condition for the generation of a lethal infection mouse model. Bars indicate mean ± SEM, from six individual groups for each concentration (n=6). Virus titer was determined within the range from 10^6 to 10^7 FFU. Analysis of the group treated with each virus titer was described in blue line with the highlight indicating the 95% confidence interval, while that of the untreated group in red. Life table provides the individual statistical analysis of the survival rate at each representative time point. Pearson's chi-squared test was performed to determine the significance of the survival model. Degree of freedom (DF) and the p-value were calculated by the Log-rank test.

We next tested the antiviral drug efficacy of montelukast in the DV mouse model we generated as above. Montelukast was administered by IP injection to the lethal AG129 mouse model generated by injection of DV, in a daily dose of 10 mg/kg/day for 10 experimental days. The positive control group was daily administered with an equal volume of sterilized PBS by IP injection. We then investigated whether the injected montelukast could alleviate the symptoms of viral infection associated with lethality. As one of the well-known symptoms, severe weight loss was observed in the lethal mouse model infected with DV prior to death[28]. Compared to the infected control group, administration of montelukast induced the consistent maintenance of mice body weight (Figure 2.10).

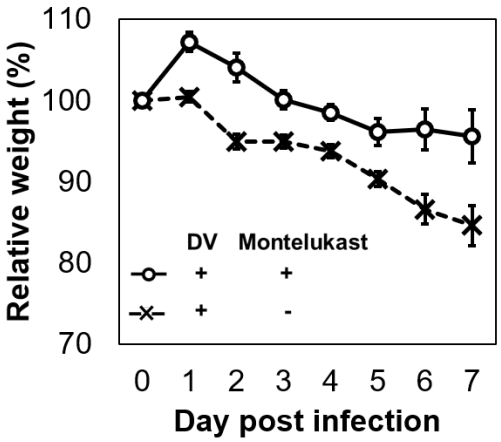

Figure 2. 10 Relative weight change after the DV2 infection followed by the administration of vehicle or montelukast. The analysis includes data obtained upto day 7, as the number of mice in the negative control group (vehicle treated) fell below 2 (which was insufficient to derive standard deviation) at day 8. Bars indicate mean ± SEM.

Next, the montelukast treatment-dependent survival probability was calculated according to the Kaplan-Meier estimate model (Figure 2.11A, B). As shown in the graph, the injection of montelukast to the DV infected mice significantly decreased lethality and improved survival rate (p value = 0.023). Such result was highly correlative to the decreasing tendency in viremia (virus titer in plasma),

clearly indicating the inhibition of the viral replication after the systemic administration of montelukast (Figure 2.8C).

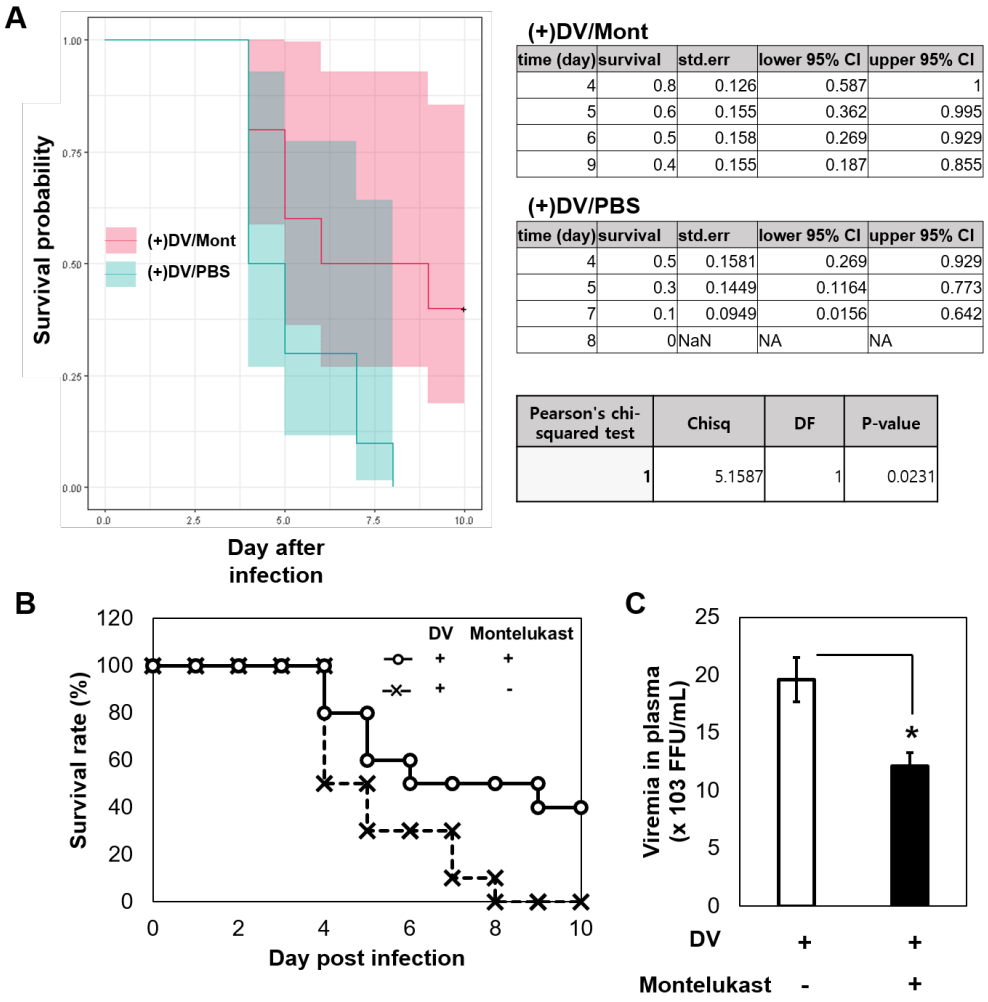

Figure 2. 11 (A) Statistical significance analysis of the drug treatment-dependent survival rate. The dose-dependent survival curve was plotted according to the Kaplan-Meier estimate model. Virus-infected AG129 mice were administered with either montelukast (Mont) or PBS (n=10 for each group). Analysis of the group treated with montelukast was described in red line with the highlight indicating the 95% confidence interval, while that of the untreated group in blue. Life table shown on the right side provides the individual statistical analysis of the survival rate at each representative time point. Pearson's chi-squared test was performed to determine the significance of the survival model. Degree of freedom (DF) and the p-value were calculated by the Log-rank test. (B) Survival rate analysis of DV infected AG129 mice after daily IP administration of montelukast. Statistical significance was estimated by log-rank test (p=0.023). (C) Relative peak viremia reduction analysis in plasma, performed at day 3 post infection (p.i.).

When the viral replication propagates in the host, it is expected to induce massive production of inflammatory cytokines from the host defense system, of which phenomena known as a cytokine storm[29]. As montelukast showed therapeutic efficacy as a direct-acting antiviral agent against DV infection by increasing the survival rate in a mouse model, we further investigated whether the compound could reduce the immune response related to DV infection. Indeed, the administration of montelukast decreased the level of representative inflammatory cytokines including TNF, IL-6 and IFN-γ as measured on the day when the virus titer in plasma was estimated to be at the highest level (Figure 2.12).

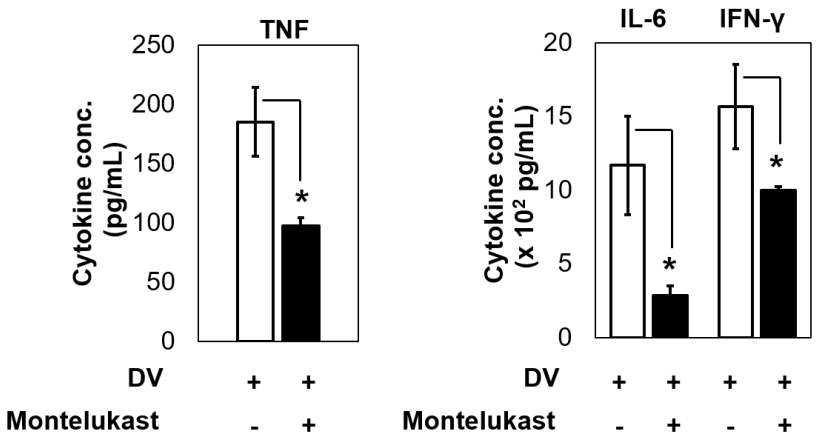

Figure 2. 12 Cytokine analysis against inflammatory cytokines; (TNF, IL-6, IFN-γ). * for $p \leq 0.05$.

In addition, complete blood count (CBC) analysis was performed in which the overall change in the blood components induced by the DV infection was attenuated, such as decrease of hematocrit at severe infection, increase of neutrophils and lymphocytes, and decrease of platelets[30] (Figure 2.13).

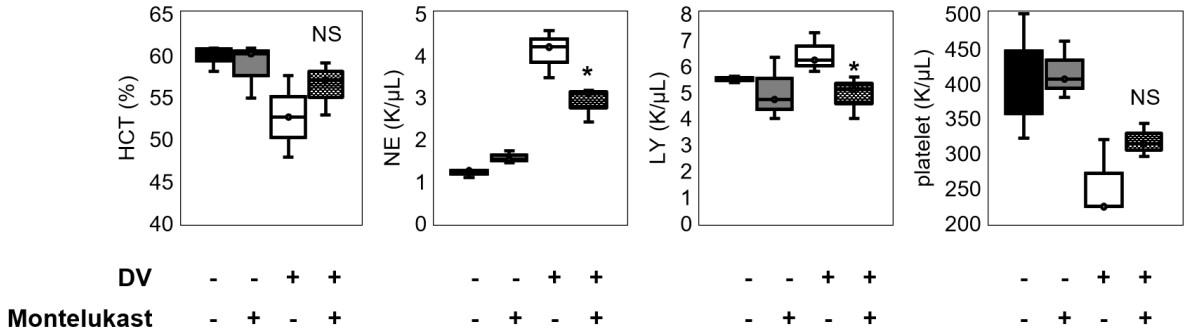

Figure 2. 13 The treatment of montelukast relieved abnormality in complete blood count analysis. Bars indicate mean ± SEM, from four individual groups for each concentration (n=4). (HCT; hematocrit, NE; neutrophil, Ly; lymphocyte) To determine the significance of the data, Student's t-test was performed to derive p-value. * or ** indicates a significant change compared to the vehicle (PBS) control; * for $p \leq 0.05$, ** for $p \leq 0.01$ and NS (not significant) for $p > 0.05$.

In addition to the investigation of the systemic antiviral effect of montelukast, the specific, local therapeutic impact on the peripheral organs was also examined. Five representative organs (spleen, liver, lung, small intestine, and large intestine) were collected and analyzed to estimate the changes in viral load and tissue morphology. As shown in Figure 2.14, administration of montelukast significantly reduced the virus RNA concentration in each organ and in whole blood as well, although the degree of the viral RNA concentration decrease is different from organ to organ.

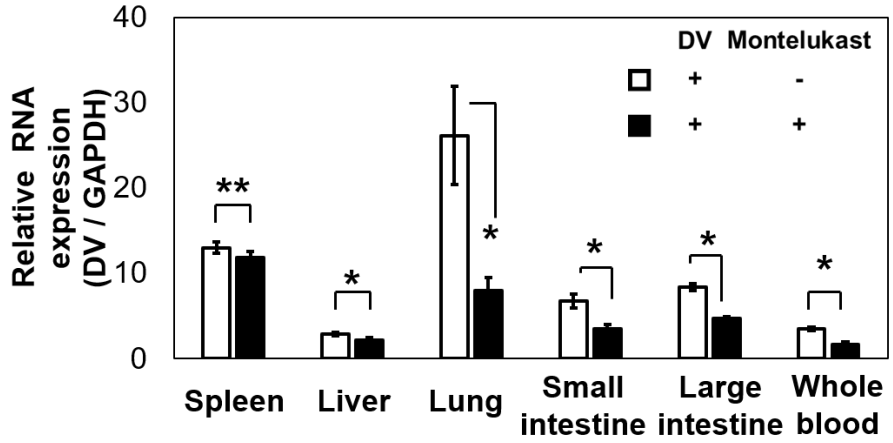

Figure 2. 14 Relative DV RNA expression level analysis was performed with each representative tissue sample (spleen, liver, lung, small intestine, large intestine and whole blood). The overall semi-quantification of RNA expression was

normalized by endogenous control (GAPDH) and compared against each other. Bars indicate mean ± SEM, from six independent mice (n=6). To determine the significance of the data, student's *t*-test was performed to derive *p*-value. * or ** indicates a significant change compared to the vehicle (PBS) control; * for $p \leq 0.05$ and ** for $p \leq 0.01$.

To determine whether the change in viral RNA concentration in each organ is sufficient to relieve the infectious symptoms, the representative histopathology study on liver was performed, of which the unique symptoms of viral infection are well known[31, 32] (Figure 2.15). Several pathological features of the infection specific to liver are cell integrity loss, enlargement of the sinusoidal space and the escalation of focal necrosis. It is generally known that the overall features of the cytopathic effect by the viral infection would eventually lead to the generation of the focal necrosis and apoptosis, resulting in the sinusoidal and lobular collapse to induce liver malfunctioning. It turned out that the administration of montelukast supported the significant maintenance of the cell integrity or the sinusoidal space, which resulted in the sufficient density of hepatocytes similar to that of the uninfected liver tissue. In addition, focal necrosis (labeled in black arrows) was also diminished by size and area in the liver tissue.

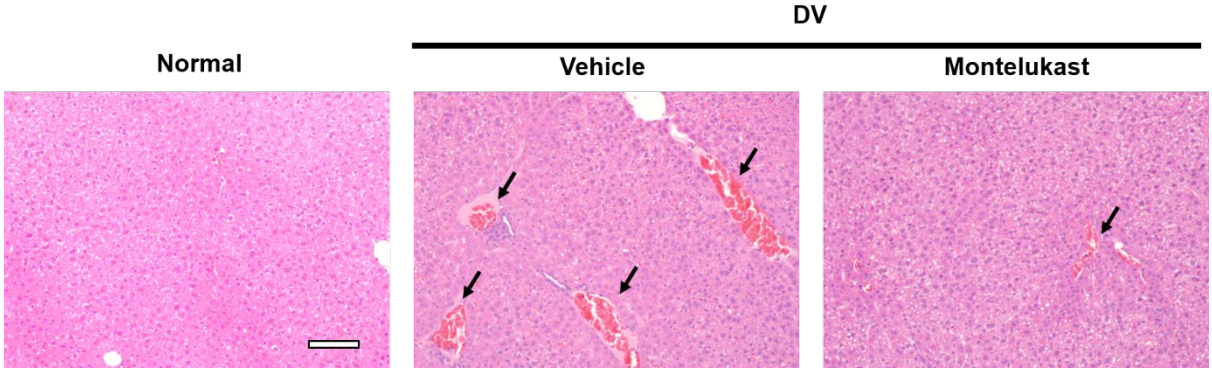

Figure 2. 15 Pathology analysis data. H&E stained images of liver section are shown. Scale bar=100 μm.

Other organ-specific changes occur in spleen, of which size and weight increases upon virus infection (known as splenomegaly)[33]. We found that administration of montelukast alleviated the development of splenomegaly compared to that of the untreated group (Figure 2.16). Collectively, the data indicate that the inhibition of DV replication by montelukast could significantly relieve various symptoms of DV infection and achieve the comprehensive, systemic antiviral therapeutic effect *in vivo*.

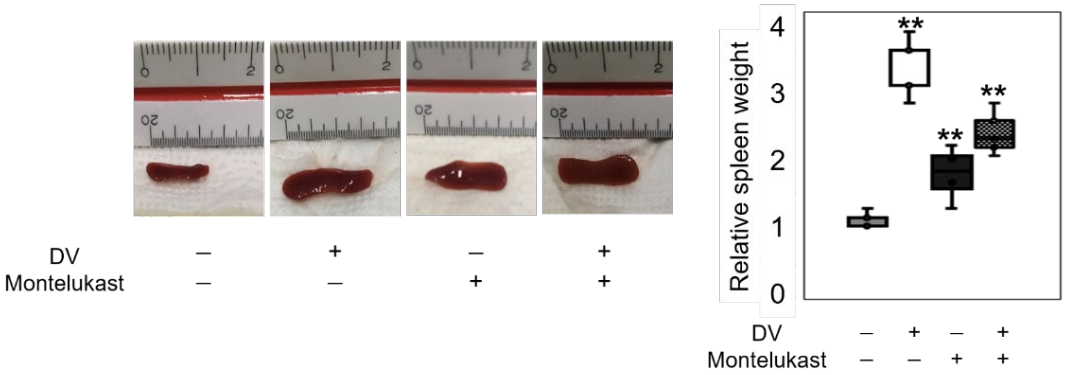

Figure 2. 16 Montelukast attenuated enlargement of spleen caused by DV infection. Presented images are representative of each group. Bars of the graph on the right indicate mean ± SEM, from three individual groups for each concentration (n=3). To determine the significance of the data, Student's t-test was performed to derive p-value. * or ** indicates a significant change compared to the vehicle (PBS) control; * for $p \leq 0.05$, ** for $p \leq 0.01$.

2.3 Discussion

Being aware of the tedious and laborious procedure and the complex handling required for the enzyme-involved parallel screening, our research was initiated with the aim to develop a facile platform to enhance the convenience and efficacy in the anti-viral agent discovery. To do so, we first devised the strategy to adopt the advantage of the GO-based biosensor to convert the enzyme activity into the quantitatively analyzable fluorescence intensity. Then we utilized the detailed protocol of RANGO to maintain its analytic validity when applied to the high-throughput screening. Due to the chemical stability of GO in conventional room conditions, it provides not only convenience in the storage and management but also the reduction of the experimental burden when operating RANGO. Throughout Z'-factor derivation and model inhibitor analysis, our system proved the reproducibility and reliability as the tool for the high-throughput screening of RdRp inhibitors. As the demonstration of the practical application of RANGO, we performed the multi-well based, high-throughput chemical screening to identify a novel direct-acting antiviral agent against DV from the FDA-approved small molecule library.

Categorized as an arbovirus, generally known mechanism for DV infection starts from the mosquito bite and the virus intrudes into the bloodstream of the host, which chronologically infects the epidermal tissues and tissue-residing immune cells, lymph node, and then spreads out to induce systemic infection toward peripheral organs[34]. It has been reported that DV shows tissue tropism after the infection to the host, including the bone marrow, lymph node, spleen, liver, and lung[35]. To prove that the RdRp inhibitor candidate we sorted out could eventually become anti-DV drug, it was required to determine whether the drug candidate is capable of practical viral reduction in at least one of these tissues

stated above. We used various approaches involving series of cell and animal-based models to evaluate the antiviral efficacy of the RdRp inhibitor selected from RANGO-based screening. Along with the most abundant monkey kidney cell model, we conducted additional cell experiments with the representative human cell models as well. It was inevitable to examine whether the RdRp inhibitor candidate we sorted out could show the practical antiviral effect in the human tissue. After the cell-based validation, we then conducted the animal-based study to eventually investigate the capability of the drug candidate to block the systemic spread-out of the viral infection. We managed to consider as many factors as possible to derive the conclusion, including the external symptoms (weight loss and survival rate), viral reduction in whole blood and each representative peripheral tissues, the relief of tissue-specific symptoms, cytokine level and changes in the blood cells. Throughout the series of verification, we concluded that the very compound, montelukast, showed a significant potential as a direct-acting antiviral drug candidate.

Previously, montelukast is known as a leukotriene receptor antagonist[36] and is approved by the FDA for the oral administration to treat chronic asthma. Related to viral infection, one previous report only showed that montelukast might possibly induce the partial reduction of the vascular leakage occurred by severe viral infection due to blocking mast cell-derived factors.[37] However, no evidence was shown to claim that the compound could inhibit virus replication in any way and the proof-of-concept was limited to the effect of the compound toward immune system as a leukotriene receptor antagonist. In the present study, we performed RANGO-based massive screening and identified montelukast as a highly potent DV RdRp inhibitor. We further performed a series of experiments to reveal the clear pieces of evidence supporting the role of montelukast as an anti-

viral agent. Based on the *in vitro* and *in vivo* data, we suggest that montelukast could be adopted as a direct-acting antiviral drug targeting the DV RdRp. As far as we know, such mechanism of action (MoA) has not been proposed in previous studies regarding the antiviral effect of the compound. In viewpoint of antiviral drug, montelukast may enjoy its high efficacy as an anti-DV drug by dual MoAs as i) a direct-acting anti-viral agent by inhibiting DV RdRp and therefore, inhibiting viral replication to directly reduce viral titer in the body, and ii) a leukotriene receptor antagonist to reduce the vascular leakage related symptoms as well.

One of the biggest bottlenecks on the antiviral drug development is the rapid evolution of the target virus. It is generally accepted that RNA viruses are more problematic due to their contribution to the epidemic diseases and threaten global health. The genetic instability of RNA virus leads to the continuous generation of variants alongside the spread-out from one host to another. The speed of such progression is much faster than other pathogens. The future development of antiviral drugs, therefore, should be in a swift and strategic manner, with limited sources (time, labor, and money). Regarding such situation, it is urgent to develop the drug screening platform which is validated with its performance and efficiency. In terms of the drug screening system, the overall data indicates that our RANGO system is capable of rapid and reliable evaluation of the potent direct-acting antiviral drug candidates in a high-throughput manner, which is the superior feature compared to those of the conventional gel-based methods. Yet, regarding that our current system is based on the laboratory-scale, the maximum number of the analytes in a single analysis is highly dependent to the experimental apparatus (e.g. in case of utilizing 96 multi-well plates, a single analysis is capable of the maximum of ~80 analytes, which takes approximately 5~10 minutes for the

quantitative analysis). Thus, future investigations for the improvement of RANGO may consider the strategy to be applied for the massive, industrial-scale analysis to further increase the efficacy of the screening. One of the approaches may include the adoption of the systemic automation process, which would contribute to the reduction of the analytical fluctuation. Also, in terms of the validity of the repurposed drug candidate, our current results from the animal-based studies only indicate the antiviral effect of montelukast when administered by IP injection method in a single dose/day. Though montelukast is known to be treatable by both IP and oral, it had been widely transcribed orally for humans, which is accepted as more favorable treatment method. Thus, further investigation is required for this drug to confirm both the antiviral effect via oral delivery and the optimized dose condition in clinical trials. Hopefully, as it is generally accepted that the systemic drug absorbance is greater by oral delivery than that of the IP, the antiviral effect featuring the oral treatment of montelukast is indeed expected to be positive.

In summary, we developed the RANGO system, which is cost-effective, simple and robust RdRp activity analysis technology for the discovery of viral RdRp inhibitor. Its application to the high-throughput screening against the FDA-approved drug library enabled the rapid selection of the potent RdRp-specific inhibitors. Throughout the series of studies carried out *in vitro* and *in vivo*, we identified a highly potent compound, montelukast, as a direct-acting antiviral drug candidate by inhibiting DV RdRp activity and subsequently, DV replication mediated by the enzyme. Based on the significance of the preliminary data, we suggest that this small molecule selected by RANGO possesses a great potential to be further investigated for the practical use to combat against the DV-associated diseases. Considering the validity of the hit compound, we insist that our system

could provide the accelerating option for sorting out the potent direct-acting antiviral drug candidates at the initial stage of the drug discovery process.

2.4 Material and Methods

Materials & Reagents

Graphite powder was purchased from Graphit Kropfmühl AG (Hauzenberg, Germany). Sulfuric acid (H_2SO_4) and hydrogen peroxide (30% in water) (H_2O_2) were purchased from Daejung (Gyeonggi do, Korea). RNase A, Potassium permanganate ($KMnO_4$) and sodium nitrate ($NaNO_3$), Hoechst 33342, anti-mouse IgG, and methylcellulose were purchased from Sigma-Aldrich (St. Louis, MO). Whatman filter paper was purchased from GE healthcare (Illinois, USA). All reagents were used ad received without further purification. DMEM (Dulbecco's Modified Eagle's Medium), RPMI, 0.25% trypsin-EDTA solution and PBS (pH 7.4) were purchased from WelGENE Inc. (Daegu, Korea). CCK-8 (Cell Counting Kit-8) was purchased from Dojindo Molecular Technologies, Inc. (Rockville, MD, USA). MLV-RT™ reverse transcriptase was purchased from Elpis Biotech (Daejeon, Korea). Protease inhibitor cocktail, GlutaMAX™, 10x MEM, sodium bicarbonate were purchased from Thermo Fisher Scientific Inc. (Waltham, MA, USA). Primers for RT-PCR were purchased from Bioneer Inc. (Seoul, Korea). Montelukast sodium was purchased from TCI Inc (Tokyo, Japan). NTP solutions were purchased from NEB (Messachusetts, USA). SYBR green master mix was purchased from Applied Biosystems Inc. (California, USA).

Cloning, expression and purification of the RdRp recombinant protein

The coding sequence of the full-length NS5 protein from dengue virus serotype 2 (DENV-2) was synthesized by Integrated DNA Technologies (IDT, USA). The DENV-2 NS5 sequence was fused to the coding sequence of the N-terminal 10 His-tagged superfolder GFP (sfGFP) and inserted into the pX vector. The expression plasmid was amplified in the *E. coli* strain JM109, and the purified

plasmids were transfected into HEK293E cells. The transfected cells were harvested four days after transfection and resuspended in the prepared buffer supplemented with RNase A, Staphylococcal nuclease, $CaCl_2$, PMSF and protease inhibitor cocktail. The resuspended cells were lysed by sonication. The supernatant was collected and the desired protein was primarily purified by Ni-NTA column. The eluted proteins were further purified using a HiLoad 16/600 Superdex 200 pg column (GE healthcare, USA). The peak fractions were pooled and concentrated to approximately 1 mg/mL. The concentrated proteins were flash-frozen in liquid nitrogen and stored at −80°C prior to use in inhibitor screening assay.

Synthesis of graphene oxide

Graphene oxide was made according to the modified Hummers' method. Graphite, sodium nitrate, and sulfuric acid were mixed in round bottom flask and vigorous stirring in an ice bath. After stabilization, slowly added $KMnO_4$. The flask was transferred to an oil bath and heated at 35℃ for 1 hr. Distilled water 40 mL was slowly dropped in the round flask in an ice bath. Then, the flask was placed in an oil bath at 95℃ for 30 min. Reactive substances remaining in the flask were quenched by adding 5 mL of H_2O_2, and the graphene oxide solution was purified by filtration using Buchner funnel. The purified graphene oxide was lyophilized and finally dispersed in distilled water to a concentration of 1 mg/mL.

Characterization of graphene oxide

Size and morphology of graphene oxides were characterized by atomic force microscope NX-10 (Park Systems, Korea). UV-Vis spectrophotometer Lambda 465 (PerkinElmer, USA) was used to obtain UV-Vis spectra. Zeta potential and DLS analysis were performed by using Zetasizer NanoS (Malvern instruments, UK). Raman spectra was measured by LabRAM HR UV-vis-NIR (Horiba Jobin

Yvon, France) using an Ar ion CW laser (514.5 nm) as an excitation source focused through a BXFM confocal microscope with an objective lens (50x, numerical aperture = 0.50). The measurement of FT-IR spectra was performed with an EQUINOX55 (Bruker, Germany).

Development of RNA-nano-graphene oxide based viral RdRp activity assay (RANGO)

To prepare DV serotype 2 RdRp substrate, a single strand RNA labeled with Cy5 was prepared (5'- UUUUUUUUUUUUUACUAACAACU -3', Bioneer, Korea) in buffer solution. Reaction mixture for measuring RdRp activity was prepared by mixing 3 pmole of RNA substrate, 3.5 pmole DV2 RdRp and 0.1 mM ATP, 0.5 mM C/U/GTP in the RdRp buffer in 60 μL and incubated for 1 hour at 37℃. NGO solution was prepared at 2.5 μg/mL in distilled water right before use from a 1 mg/mL stock solution. After the incubation, NGO was added to each sample at the final concentration of 1.5 μg/mL. Reactants were transferred to a 96-well black-bottom microplate and the eventual RdRp activity was measured by monitoring fluorescence intensity at Ex/Em = 650 nm/670 nm with SynergyMx fluorometer (BioTek, UK).

Z'-factor determination

The experiment was conducted in 96 well plate scale. For the positive control, RdRp activity was induced by addition of 3 pmole of RNA substrate, 3.5 pmole of DV serotype 2 RdRp and 0.1mM ATP, 0.5mM C/U/GTP in the RdRp buffer (60 μL). For the negative control, same volume of nuclease-free water (NFW) was added instead of NTP solution. After 1 hour of incubation at 37℃, NGO was added to each well at final concentration of 1.5 μg/mL. Right after the addition of NGO, the fluorescence intensity was measured at Ex/Em = 650 nm/670 nm (n=20). Z'-factor was derived according to the equation as follows:

$$Z' = 1 - \frac{(3\sigma_{c+} + 3\sigma_{c-})}{|\mu_{c+} - \mu_{c-}|}$$

σ_{c+} : standard deviation of the positive control

σ_{c-} : standard deviation of the negative control

μ_{c+} : average of the positive control

μ_{c-} : average of the negative control

RANGO-based chemical library screening

High-throughput chemical library screening was performed against 2,400 candidate molecules from the FDA-approved chemical library (Selleckchem, USA) with incorporation of RANGO system under the optimized condition as described above. Each chemical was added to the RdRp activity-induced buffer solution at the final concentration of 200 μM. For negative control, NTP was replaced with NFW. After 1 hour of incubation at 37℃, NGO was added to each well at final concentration of 1.5 μg/mL. Right after the addition of NGO, the fluorescence intensity was measured at Ex/Em = 650 nm/670 nm.

Quantitative enzyme inhibition analysis

The experimental procedures were performed in 96 well plate. For evaluation of the RdRp inhibition property of montelukast with RANGO system, the compound solution was added to the RdRp activity-induced buffer solution in serially diluted concentration from 0 to 1,000 μM. After 1 hour of incubation at 37℃, NGO was added to each well at final concentration of 1.5 μg/mL. Right after the addition of NGO, the fluorescence intensity was measured at Ex/Em = 650 nm/67 nm. Relative RdRp activity correlative to the difference in the fluorescence signal was plotted versus the treated drug concentration, and the IC_{50} was calculated according to the logistic curve-fit method applied with OriginPro 8 (OriginLab, USA).

Virus and cell culture

DV serotype 2 (strain KUMC-29) was kindly provided from Korea Bank for Pathogenic Viruses in Korea University, Seoul, Korea. Monkey kidney cell line (VeroE6) was kindly provided by Professor K. Ahn from Department of Biological Sciences, Seoul National University. Liver carcinoma cell line (Huh-7) and lung carcinoma cell line (A549) were purchased from ATCC Inc. (USA). The virus stock propagation and expansion for the concentration was proceeded in VeroE6 cells. After harvest, the viruses were concentrated by ultracentrifugation at 36,000 rpm, 4℃ for 3 hours. The concentrated titer was quantified by focus forming assay. Virus titer was shown as focus forming units (FFU) per mL. VeroE6, Huh-7 cell lines were cultured with complete DMEM medium in 5% CO_2, 37℃. A549 cell line was cultured with complete RPMI medium (RPMI with 10% FBS, 1% P/S) in 5% CO_2, 37℃.

Cell viability test

CCK-8 assay was performed according to the manufacturer's instruction. Prior to the experiment, VeroE6, Huh-7 and A549 cells were seeded in densities of 10.5 x10^4, 7.0 x 10^4 and 7.0 x 10^4 cells/cm^2, respectively. After 24 hours of incubation in 5% CO_2, 37℃, montelukast was treated in serially diluted concentration for 48 hours. CCK-8 reagent was treated at concentrations of 10% v/v to each group and incubated for 1~4 hours in the conventional cell culture condition. The quantitative analysis of the change in colorimetric intensity was performed by measuring the optical density of formazan salt at 450nm with a microplate reader (Molecular Devices, Inc., USA). The experiment was carried out in triplicate, of which data were shown as mean ± SEM.

In vitro virus infection test

Prior to the experiment, VeroE6, Huh-7, and A549 cells were seeded in densities

of 10.5 x10^4, 7.0 x 10^4 and 7.0 x 10^4 cells/cm^2, respectively. After 24 hours of incubation under 5% CO_2, 37℃, DV serotype 2 was inoculated to each cell culture by MOI of 0.1, 0.5, and 2.5, respectively under serum-free culture media for 2 hours. The culture plates were gently rocked every 30 minutes for even distribution of the virus to the cells. Montelukast solutions were prepared with serially diluted concentration in each complete culture medium containing 0.75% methylcellulose. After the incubation, virus media was removed and the cells were washed with sterilized PBS once, followed by the treatment of the chemical solutions. Cells were incubated under the culture chamber for 48 hours. After the incubation, each group was prepared for the focus forming assay (FFA) and relative viral RNA expression analysis. For FFA, chemical solutions were removed and the cells were washed with sterilized PBS, followed by fixation with 4 % paraformaldehyde. For viral RNA expression analysis, cells were treated with TRIZOL after the washing process and stored at -70℃ for further analysis.

Focus forming assay (FFA)

FFA was performed against NS1 protein of DV serotype 2. Cells fixed with 4% paraformaldehyde were rinsed with PBS for 3 times. Blocking solution was treated for 1 hour at RT. After washing with PBS, primary antibody (mouse anti-Flavivirus NS1, 1:2000) was treated to each group for 2 hours at RT or overnight at 4℃. After washing with PBS, secondary antibody (anti-mouse IgG-FITC, 1:500) was applied to each group for 1 hour at RT. After rinsing, PBS containing 10 μg/ mL of Hoechst 33342 was treated to each group for nuclear staining. Viral focus forming units stained in fluorescence were observed and analyzed by microscope (Olympus, Japan).

Animal experiments

AG129 mice (129/Sv IFN-α/β, -γ receptor deficient) were purchased from

Marshall BioResources (UK). All experimental procedures were preapproved by IACUC of Seoul National University (Korea) and Chonbuk National University (Korea), and were performed according to the guidelines of the recommendations from Association for Assessment and Accreditation of Laboratory Animal Care. As the DV is epidemic by mosquitoes, the cages with filter cover was used to avoid any unexpected contact and contamination.

Experimental groups for in vivo virus infection test

For determination of the appropriate virus titer for infection, AG129 mice (10~12 weeks) were inoculated by intraperitoneal injection with various viral titer: 10^6, 5 x 10^6 and 10^7 FFU. For evaluation of the antiviral properties of montelukast, AG129 mice (10~12 weeks) were intraperitonially (IP) injected with DV (10^7 FFU), followed by IP administration of either 200 μL of montelukast (10 mg/kg/day) or PBS. Drug treatment was performed once a day. Negative control (uninfected group) was administered with 300μL PBS instead of virus. For drug control group, 200μL of montelukast (10 mg/kg/day) was administered solely to the non-infected AG129 mice.

Mouse weight loss & survival rate analysis

Weight loss and mortality state were monitored daily. In the survival analysis, euthanized mice exhibiting severe disease-associated symptoms or rapid weight loss were counted as moribund state at the moment of the exhibition. Each weight was analyzed in relative percentage against that of day 0.

Complete blood count, viremia analysis, whole blood RNA expression analysis, and cytokine bead assay

At day 3 post infection (p.i), blood was collected from each mouse and transferred into EDTA-coated anti-coagulant tubes. After gentle mix by rocking for 10 minutes, 20 μL of each sample was analyzed for complete blood counts with

HEMAVET 950FS (Drew Scientific, USA). Measured value of each factor was semi-quantitatively analyzed against that of the uninfected control. For analysis of viremia and expression change in cytokines, plasma was separated by centrifugation at 8000 g, 4ºC for 15 minutes. Virus titer in the plasma (viremia) and viral RNA expression in whole blood was analyzed by quantitative real-time PCR (qRT-PCR). To examine change in the expression of inflammatory cytokines (TNF, IL-6, IFN-γ), cytokine bead assay (CBA) was performed. All samples were analyzed according to the manufacturer's instruction (BD Biosciences, USA).

Mouse necropsy

At day 3 p.i., mice were sacrificed from each group (n=6). Organ samples (spleen, liver, lung, small intestine, and large intestine) were collected and prepared for the virus RNA expression analysis and histopathology analysis. Spleens were weighed to determine splenomegaly. For the virus RNA expression analysis, half of the spleen, liver, and lung were homogenized and treated with TRIZOL reagent and stored at -70℃ for further analysis. The same procedures were applied to the whole samples of small intestine and large intestine. The other half of the spleen, liver, and lung were submerged to 4% paraformaldehyde for fixation and stored at 4 ºC.

Relative viral RNA expression level analysis

For investigation of viral RNA expression change in the collected specimens, RNA was isolated from each cell-based and animal-based sample treated with TRIZOL reagent, followed by cDNA synthesis aided by MLVRT™ reverse transcriptase according to the instruction manual. For target gene amplification, each primer was designed in consideration of GC content less than 50% and overlapping between two exons of the target genes with the expected amplicon size of ~100 bps. Quantitative real-time PCR (qRT-PCR) was conducted to quantify viral RNA.

Each reaction was conducted in a 20 μL volume, with SYBR green master mix. Quantstudio3™ (Applied Biosystems Inc., USA) was utilized in this study in two-step amplification process. For analysis of viremia, a linear correlative standard curve was established between the virus titer (FFU/mL) and the corresponding threshold cycle (CT) value. Virus in plasma was calculated according to the equation of the standard curve. Standard curve was derived against serially diluted viral titer. For cell-based groups and mice organ samples (including whole blood), semi-quantitative viral RNA was analyzed against that of the endogenous control, GAPDH.

Primer sequence information

Gene	Forward primer (5'- … -3')	Reverse primer (5'- … -3')	Amplicon size (bp)
Human GAPDH	TCACTGCCACCCAGAAGACTG	GGATGACCTTGCCCACAGC	123
Mouse GAPDH	TGACCTCAACTACATGGTCTACA	CTTCCCATTCTCGGCCTTG	85
DV2 NS1	GCTCCTTCAATGACAATGCGCTGTA	CCTGAAACC CCTTCCACGAAGTC	65

Table 2. 1 Primer sequence information of human GAPDH, Mouse GAPDH, and DV2 NS1

Pathology analysis

Organ samples fixed in 4% paraformaldehyde went through series of procedures as follows: paraffin embedding, section, and stain with hematoxylin and eosin (H&E) at the pathology core facility in Center for Medical Innovation, Seoul National University Hospital (SNUH-CMI), Korea.

Statistical analysis

Data plots with concentration-dependent assays were analyzed by OriginPro 8. In brief, logarithmic sigmoidal curves were fitted according to each data set. Error bars indicate ± SEM unless stated otherwise. Statistical significance of the *in vitro* and *in vivo* antiviral efficacy analysis was evaluated by two-tailed *t*-test. Statistical

significance of the survival rate was analyzed by log-rank test with R (R Foundation for Statistical Computing, Austria).

2.5 Reference

1. Mackenzie, J. S.; Gubler, D. J.; Petersen, L. R., *Nat Med* **2004,** *10* (12 Suppl), S98-109.

2. Rathore, A. P. S.; St John, A. L., *Open Biol* **2018,** *8* (8).

3. Janai, H. K.; Marks, M. I.; Zaleska, M.; Stutman, H. R., *Pediatr Infect Dis J* **1990,** *9* (3), 209-11.

4. De Clercq, E.; Li, G. D., *Clin Microbiol Rev* **2016,** *29* (3), 695-747.

5. Low, J. G.; Ooi, E. E.; Vasudevan, S. G., *J Infect Dis* **2017,** *215* (suppl_2), S96-S102.

6. Baumert, T. F.; Berg, T.; Lim, J. K.; Nelson, D. R., *Gastroenterology* **2019,** *156* (2), 431-445.

7. Low, J. G.; Sung, C.; Wijaya, L.; Wei, Y.; Rathore, A. P. S.; Watanabe, S.; Tan, B. H.; Toh, L.; Chua, L. T.; Hou, Y.; Chow, A.; Howe, S.; Chan, W. K.; Tan, K. H.; Chung, J. S.; Cherng, B. P.; Lye, D. C.; Tambayah, P. A.; Ng, L. C.; Connolly, J.; Hibberd, M. L.; Leo, Y. S.; Cheung, Y. B.; Ooi, E. E.; Vasudevan, S. G., *Lancet Infect Dis* **2014,** *14* (8), 706-715.

8. Nguyen, N. M.; Tran, C. N.; Phung, L. K.; Duong, K. T.; Huynh Hle, A.; Farrar, J.; Nguyen, Q. T.; Tran, H. T.; Nguyen, C. V.; Merson, L.; Hoang, L. T.; Hibberd, M. L.; Aw, P. P.; Wilm, A.; Nagarajan, N.; Nguyen, D. T.; Pham, M. P.; Nguyen, T. T.; Javanbakht, H.; Klumpp, K.; Hammond, J.; Petric, R.; Wolbers, M.; Nguyen, C. T.; Simmons, C. P., *J Infect Dis* **2013,** *207* (9), 1442-50.

9. Dulbecco, R., *Proc Natl Acad Sci U S A* **1952,** *38* (8), 747-52.

10. Guo, F.; Zhao, X.; Gill, T.; Zhou, Y.; Campagna, M.; Wang, L.; Liu, F.; Zhang, P.; DiPaolo, L.; Du, Y.; Xu, X.; Jiang, D.; Wei, L.; Cuconati, A.; Block, T. M.; Guo, J. T.; Chang, J., *Antiviral Res* **2014,** *107*, 56-65.

11. Qing, M.; Liu, W.; Yuan, Z. M.; Gu, F.; Shi, P. Y., *Antivir Res* **2010,** *86* (2),

163-171.

12. Byrd, C. M.; Grosenbach, D. W.; Berhanu, A.; Dai, D. C.; Jones, K. F.; Cardwell, K. B.; Schneider, C.; Yang, G.; Tyavanagimatt, S.; Harver, C.; Wineinger, K. A.; Page, J.; Stavale, E.; Stone, M. A.; Fuller, K. P.; Lovejoy, C.; Leeds, J. M.; Hruby, D. E.; Jordan, R., *Antimicrob Agents Ch* **2013,** *57* (4), 1902-1912.

13. Yang, C. C.; Hu, H. S.; Wu, R. H.; Wu, S. H.; Lee, S. J.; Jiaang, W. T.; Chern, J. H.; Huang, Z. S.; Wu, H. N.; Chang, C. M.; Yueh, A., *Antimicrob Agents Ch* **2014,** *58* (1), 110-119.

14. Lu, G. L.; Gong, P., *Virus Res* **2017,** *234*, 34-43.

15. Shimizu, H.; Saito, A.; Mikuni, J.; Nakayama, E. E.; Koyama, H.; Honma, T.; Shirouzu, M.; Sekine, S. I.; Shioda, T., *PLoS Negl Trop Dis* **2019,** *13* (11), e0007894.

16. Zhu, Y. W.; Murali, S.; Cai, W. W.; Li, X. S.; Suk, J. W.; Potts, J. R.; Ruoff, R. S., *Adv Mater* **2010,** *22* (35), 3906-3924.

17. Lu, C. H.; Yang, H. H.; Zhu, C. L.; Chen, X.; Chen, G. N., *Angew Chem Int Edit* **2009,** *48* (26), 4785-4787.

18. Kim, J.; Park, S. J.; Min, D. H., *Anal Chem* **2017,** *89* (1), 232-248.

19. Jang, H.; Ryoo, S. R.; Lee, M. J.; Han, S. W.; Min, D. H., *Mol Cells* **2013,** *35* (4), 269-273.

20. Lee, J.; Park, I. S.; Park, G.; Cho, K.; Park, H. S.; Min, D. H., *Chem Commun* **2016,** *52* (81), 12112-12115.

21. Li, D. P.; Zhang, W. S.; Yu, X. Q.; Wang, Z. P.; Su, Z. Q.; Wei, G., *Nanoscale* **2016,** *8* (47), 19491-19509.

22. Zhang, J. H.; Chung, T. D. Y.; Oldenburg, K. R., *J Biomol Screen* **1999,** *4* (2), 67-73.

23. Chen, Y.; Bopda-Waffo, A.; Basu, A.; Krishnan, R.; Silberstein, E.; Taylor, D. R.; Talele, T. T.; Arora, P.; Kaushik-Basu, N., *Antivir Chem Chemother* **2009,** *20* (1), 19-36.

24. Balsitis, S. J.; Coloma, J.; Castro, G.; Alava, A.; Flores, D.; McKerrow, J. H.; Beatty, P. R.; Harris, E., *Am J Trop Med Hyg* **2009,** *80* (3), 416-24.

25. Lee, Y. R.; Su, C. Y.; Chow, N. H.; Lai, W. W.; Lei, H. Y.; Chang, C. L.; Chang, T. Y.; Chen, S. H.; Lin, Y. S.; Yeh, T. M.; Liu, H. S., *Virus Res* **2007,** *126* (1-2), 216-225.

26. Xu, H.-Y.; Vasudevan, S. G.; Liu, W.; Schul, W.; Flamand, M., *The Journal of Infectious Diseases* **2007,** *195* (5), 665-674.

27. Williams, K. L.; Zompi, S.; Beatty, P. R.; Harris, E., *Ann N Y Acad Sci* **2009,** *1171 Suppl 1*, E12-23.

28. Sarathy, V. V.; White, M.; Li, L.; Gorder, S. R.; Pyles, R. B.; Campbell, G. A.; Milligan, G. N.; Bourne, N.; Barrett, A. D., *J Virol* **2015,** *89* (2), 1254-66.

29. Rothman, A. L., *Nat Rev Immunol* **2011,** *11* (8), 532-43.

30. Bozza, F. A.; Cruz, O. G.; Zagne, S. M.; Azeredo, E. L.; Nogueira, R. M.; Assis, E. F.; Bozza, P. T.; Kubelka, C. F., *BMC Infect Dis* **2008,** *8*, 86.

31. Shresta, S.; Sharar, K. L.; Prigozhin, D. M.; Beatty, P. R.; Harris, E., *J Virol* **2006,** *80* (20), 10208-17.

32. Barreto, D. F.; Takiya, C. M.; Schatzmayr, H. G.; Nogueira, R. M.; Farias-Filho Jda, C.; Barth, O. M., *Mem Inst Oswaldo Cruz* **2007,** *102* (2), 175-82.

33. Povoa, T. F.; Alves, A. M.; Oliveira, C. A.; Nuovo, G. J.; Chagas, V. L.; Paes, M. V., *PLoS One* **2014,** *9* (4), e83386.

34. Martina, B. E.; Koraka, P.; Osterhaus, A. D., *Clin Microbiol Rev* **2009,** *22* (4), 564-81.

35. Kyle, J. L.; Beatty, P. R.; Harris, E., *J Infect Dis* **2007,** *195* (12), 1808-17.

36. Reiss, T. F.; Chervinsky, P.; Dockhorn, R. J.; Shingo, S.; Seidenberg, B.; Edwards, T. B., *Arch Intern Med* **1998,** *158* (11), 1213-20.

37. St John, A. L.; Rathore, A. P.; Raghavan, B.; Ng, M. L.; Abraham, S. N., *Elife* **2013,** *2*, e00481.

Chapter 3. Highly efficient and rapid neural differentiation of mouse embryonic stem cells based on retinoic acid encapsulated porous nanoparticle

3.1 Introduction

Neural differentiation method mediated by retinoic acid (RA) is one of the well-known cell conversion method incorporating small molecules for the mouse embryonic stem (mES) cell. When administered into the cytoplasm, RA binds to RA receptor (RAR) heterodimers localized at nuclear membrane, of which complex then activates the downstream signaling pathways to induce neural generation and axon outgrowth[1-3]. Several distinct strategies have been introduced to generate neural differentiation from mES cell. One of the most common methods is -4/+4 RA method, which involved 4 days of embryoid body (EB) formation to activate the cells in differentiation state, followed by another 4 days of RA treatment for neural induction[4-6]. The wide application had been made with a variety of modifications to the method. Yet, several disadvantages exist in terms of the hanging drop culture process to induce the formation of EB, such as limited EB volume, impracticable media change, and complicated procedure[7]. Another RA-based method was also introduced with consistent addition of RA to monolayer culture of mES cells[8]. Although the system successfully generated neural differentiation from adherent mES cell colony, yet several limitations exist. The repetitive addition of RA, for example, indicates a requirement for a constant supply of enough amount of RA to interact with RAR for neural induction of inactivated mES cells.

Although RA acts as one of the key factors for neural differentiation, some drawbacks must be overcome, such as its low solubility in aqueous solution and

rapid degradation by cellular metabolism[9]. Moreover, a fine-tuned control of the RA concentration is required for the desired cell conversion. It is reported that the induced cell fate mediated by RA, ranging from neuron to cardiomyocyte differentiation, is highly dependent on its concentration[10]. In addition, since RA is incorporated into cell membrane via diffusion, the stochastic kinetics associated with RA-RAR interaction would also be concentration-dependent. However, the amount of RA treated cannot be increased infinitely, since the addition of RA higher than its pharmacological concentration (>10 μM) during neural differentiation may result in a dramatic decrease in cell viability[11]. For successful neural differentiation, therefore, it is required to enhance intracellular delivery with minimal loss of RA and mediate its sustained, sufficient supplement to fulfill the needs of the induction process.

Recently, considerable investigations have been made to improve the quality of the cell conversion by incorporating various micro/nano-sized particles as intracellular delivery carrier[12-15]. Despite several notable demonstrations of their functional performance, yet limitations are expected with such polymeric particles regarding on bulk synthesis for routine applications, due to considerable labor and time required to prepare the particles with the desired characteristics. Also, it has not been proven whether such particles would even manage higher functions such as sustained supply of RA-sufficient enough to ensure stable neural differentiation of the fully undifferentiated embryonic stem cells during the induction period.

Meanwhile, mesoporous silica nanoparticle (MSN) has been developed to become one of the greatest examples of highly functionalized intracellular delivery candidates with several unique characteristics from its own porous structure. The tunable pore with a high loading capacity of MSN is suitable for encapsulating numerous categories of compounds ranging from small chemical compounds or

nucleic acids to large, hindered biomacromolecules such as protein ternary complex without losing their functions[16-18]. Moreover, the encapsulated molecules would be released from the nanoparticle in a sustained manner, which makes MSN much more powerful delivery carrier. Along with high biocompatibility, MSN can be considered as one of the most promising intracellular delivery candidates applicable to the various strategies in the field of cell conversion technology.

Here, we suggest an alternative cell conversion system incorporating MSN, to derive rapid and efficient neural differentiation of mES cells with RA (Scheme 3.1). By introducing chemically modified MSN to mediate intracellular delivery, the functional RA molecules would be concentrated around and within MSN, to result in enhancement of their intracellular incorporation without cytotoxic side effects. The RA molecules were sustainably released from the nanoparticle during the whole induction period, which ensured stable generation of the RA-RAR mediated, neural differentiation signal pathway. With the single treatment of RA/MSN complex during the induction period, we successfully obtained neural cells from mES cells with enhanced conversion efficiency, showing rapid and stable expression of neural marker gene within 6 days.

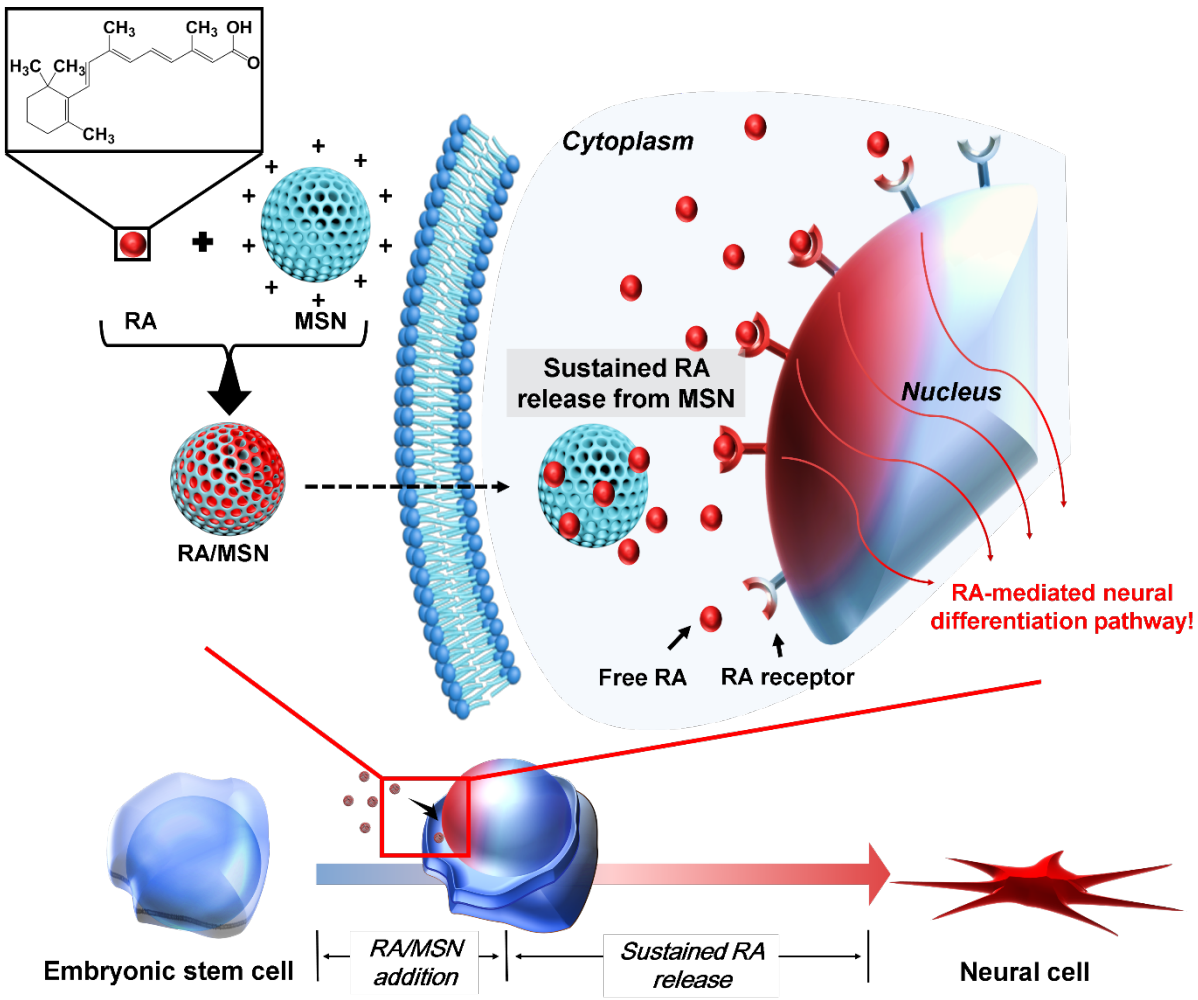

Scheme 3.1 Schematic strategy for neural differentiation of mouse embryonic stem (mES) cell, incorporating mesoporous silica nanoparticle (MSN) and retinoic acid (RA).

3.2 Result

We first prepared nanoparticle carrier candidates for intracellular delivery of RA. Though conventional MSN is known for their porous structure, its general pore size has been limited to ~2 nm in diameter. For maximum loading capacity, we prepared MSN to possess large pores (~19 nm in diameter) with accord to the previously reported method[17]. Moreover, as RA is known as negatively charged small molecule[14], the nanoparticles were required to be positively charged for ease of the complexation via electrostatic interaction. To determine the most suitably modified nanoparticle, four distinct nanoparticles were prepared, which either went on pore expansion process (to get ~19 nm from ~2 nm) or ammination process (to generate a positively charged surface from the negatively charged surface at neutral pH). In this paper, the synthesized particles are abbreviated as followed: MSN_2 for non-amminated MSN with 2 nm pore; $AMSN_2$ for amminated MSN with 2 nm pore; MSN_{19} for non-amminated MSN with 19 nm pore; and $AMSN_{19}$ for ammintated MSN with 19 nm pore (Figure 3.1A).

The synthesized nanoparticles were analyzed by their mean pore size, surface area, pore volume and surface charge (Figure 3.1B). First, transmission electron microscopy (TEM) images revealed the overall morphology of the synthesized nanoparticles. In brief, the spherical structure of the nanoparticles was maintained with a diameter of ~200 nm after the modification processes. Next, the mean pore size of each nanoparticle obtained from nitrogen adsorption method indicated that the nanoparticles with pore expansion consist of pores approximately 9-fold larger than that of without pore expansion. Then the specific surface area was calculated by using the Brunauer-Emmett-Teller (BET) equation, which revealed the effect of either pore expansion or amination to the surface area. Surface area was affected by both modification process, which decreased after each process. Pore volume,

which seemed to be only affected by pore expansion process, increased after the process. Finally, the net charge of the nanoparticles was analyzed by zeta potential, which revealed the effect of amination to endow positively charged surface to the particles.

A

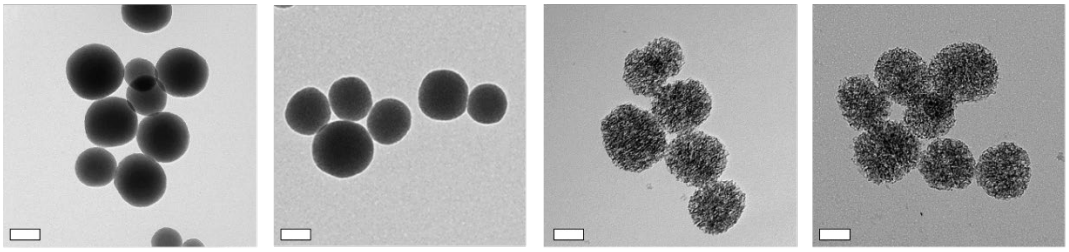

B

	Mean pore size (nm)	BET surface area (m^2/g)	Pore volume (mL/g)	Zeta-potential (mV)
MSN_2	2	1320	0.63	-21.6
$AMSN_2$	3	1253	0.64	20.9
MSN_{19}	19	465	1.22	-23.4
$AMSN_{19}$	19	437	0.97	20.4

Figure 3.1 Characterization of MSN. (A) HR-TEM images of 4 different nanoparticles. Group identification was as followed: MSN_2 for non-amminated MSN with 2 nm pore; $AMSN_2$ for amminated MSN with 2 nm pore; MSN_{19} for non-amminated MSN with 19 nm pore; and $AMSN_{19}$ for amminated MSN with 19 nm pore. Scale bars indicate 100 nm. (B) N_2 absorption/desorption analysis of nanoparticles for estimating mean pore size, BET surface area, and pore volume.

We next determined the loading capacity of the nanoparticles for encapsulation of RA (Figure 3.2A). Prior to the studies, a standard curve for RA solution was derived by plotting UV absorption peak value at 350nm versus the corresponding concentration (Figure 3.2B). For loading capacity determination, nanoparticles were soaked into RA solution in 100% ethanol and incubated up to 24 hours at room temperature, accompanied by soft rocking. The dark condition was maintained during the whole incubation process to avoid simultaneous photo-induced oxidation and isomerization of RA[19]. As a control, RA solution was incubated under the same condition without the addition of nanoparticles. Samples

were centrifuged briefly and UV absorption of the supernatant RA solution was measured at 350 nm. The concentration of remaining RA in the solution was calculated by referring to standard curve equation. Among all the nanoparticles, RA solution with $AMSN_{19}$ showed the lowest concentration of remaining RA after incubation, indicating the highest loading capacity for RA. After four hours of incubation, maximum loading capacity was calculated to be 0.18 nmole RA per 1 μg $AMSN_{19}$, which is approximately four times higher than that of $AMSN_2$.

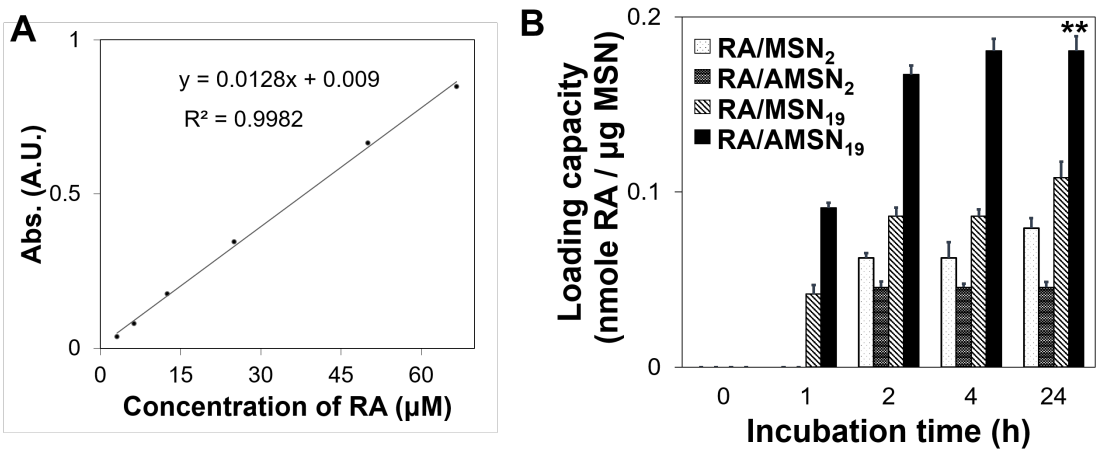

Figure 3.2 Loading capacity test of MSNs. (A) A standard curve of RA in terms of UV absorption peak value and the corresponding RA concentration. (B) Calculated RA loading capacity to nanoparticle along with incubation time. Loading capacity was determined by measuring UV absorption at 350 nm. Each of the error bar indicates standard error (n=3). ** for P< 0.001 calculated by Student's t-test.

Followed by RA loading test, the release kinetics of each nanoparticle was analyzed (Figure 3.3A, B). Each RA/MSN complex generated from 4-hour incubation in RA solution was suspended in 10% ethanol solution in PBS and incubated at 37 ℃ conditions for up to 10 days. The cumulative RA release kinetics was derived from UV absorption analysis at 350 nm of the supernatant RA solution of each sample. Compared to nanoparticles having small pores (MSN_2, $AMSN_2$), those possessing large pores (MSN_{19}, $AMSN_{19}$) showed relatively more sustained release kinetic profile, resulting in nearly 100% release within 10 days.

Such data indicate that the combination of large pores and amine functional groups of the nanoparticle could be the key factors to endow high loading capacity and sustained release feature, which makes $AMSN_{19}$ the most suitable nanoparticle candidate for intracellular delivery of RA among those we tested.

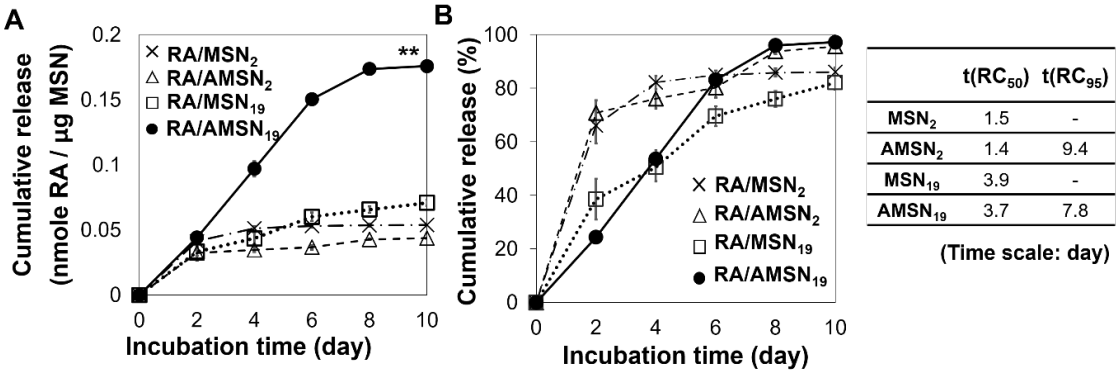

	t(RC50)	t(RC95)
MSN2	1.5	-
AMSN2	1.4	9.4
MSN19	3.9	-
AMSN19	3.7	7.8

(Time scale: day)

Figure 3.3 Release kinetics test of RA/MSNs. (A) Cumulative RA release kinetics on each nanoparticle along with incubation time. (B) Calculated percentage of RA release kinetics from each nanoparticle along with incubation time. The time period required for 50% and 95% release of RA from each RA-particle complex are indicated on the table ($t(RC_{50})$ and $t(RC_{95})$, respectively). Each of the error bar indicates standard error (n=3). ** for $P< 0.001$ calculated by Student's t-test.

Prior to the differentiation study, the viability of the mES cells was measured after treatment of the nanoparticle or its complex. $AMSN_{19}$ or $RA/AMSN_{19}$ complex was added to mES cells in various concentrations and incubated for 48 hours. Both $AMSN_{19}$ and $RA/AMSN_{19}$ hardly reduced the mES cell viability at the particle concentration much higher than required for the actual neural induction (20 μg/mL), indicating that $AMSN_{19}$ is suitable for the sensitive cells such as embryonic stem cell (Figure 3.4A, B).

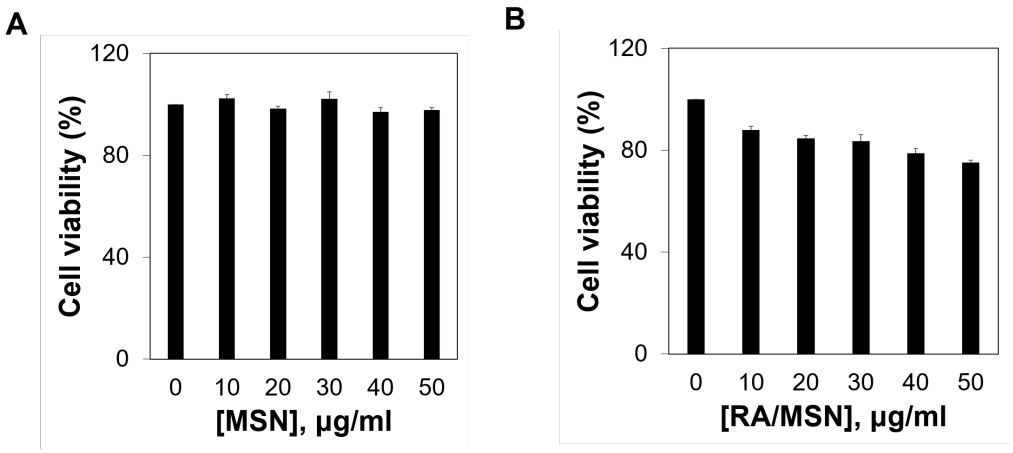

Figure 3.4 Cytotoxicity test of (A) $AMSN_{19}$ and (B)$RA/AMSN_{19}$ against mES cells

We next investigated whether $AMSN_{19}$ would be efficiently internalized by the target cells (Figure 3.5). For the convenience of trafficking, 5-carboxytetramethylrhodamine (5-TAMRA) dye-conjugated $AMSN_{19}$ ($TAMSN_{19}$) was prepared. Prior to the particle treatment, mES cells were cultured under feeder-free system aided by gelatin coating of the surface of the culture plate, which facilitated the maintenance of appropriate undifferentiating growth condition. The undifferentiated state of the cells was confirmed by the formation and maintenance of the colony-like features. The cells were treated with 20 μg/mL of $TAMSN_{19}$ and cultured with stem cell-verified serum. Under such condition, cells clearly maintained their colony-like formation and localization of $TAMSN_{19}$ was observed within the colonies.

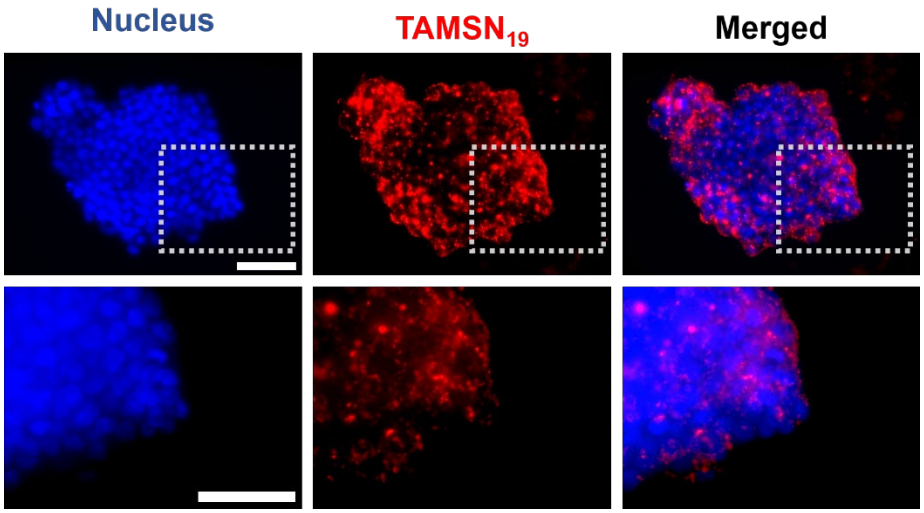

Figure 3.5 Intracellular delivery of $TAMSN_{19}$ within the mES cell colony was investigated. Fluorescence images were taken 48 hours after the particle treatment. Hoechst 33342 was treated to cells for nucleus staining. Images were taken with fluorescence microscopy. Scale bars indicate 50 μm (top) and 25 μm (bottom), respectively.

The intracellular uptake of the nanoparticle complex was revealed by fluorescence correlation analysis based on fluorescent cell images, which was enabled by z-sectioned imaging technique with Deltavision imaging equipment (Figure 3.6A). Taken the z-sectioned image within the colonies at the same planar, the nanoparticles (labeled in red) were observed mostly in the cytoplasm (labeled in blue). The successful internalization of the nanoparticles within the single mES cell was also determined by TEM image (Figure 3.6B), which revealed that the particles were successfully localized in the cytoplasmic area, approaching the perinuclear region (black, hollowed dots labeled with red arrows). Such data indicate that the nanoparticle bears the high potential to deliver the encapsulated cargos to the colonized cells.

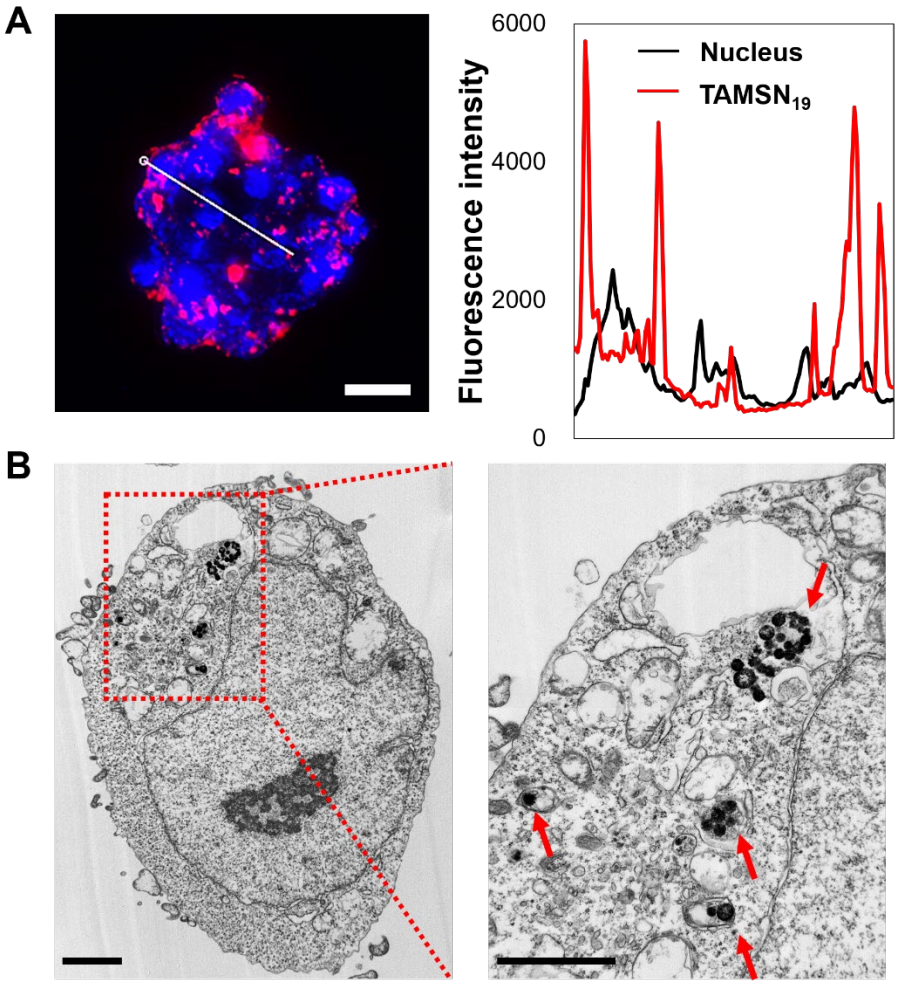

Figure 3.6 Intracolonial uptake analysis of $TAMSN_{19}$. (A) Internalization of $TAMSN_{19}$ within the cell colony revealed by fluorescence correlation analysis. Scale bar indicates 25 μm. (B) Bio-TEM image of mES cell presenting internalized $TAMSN_{19}$ inside its cytoplasm. TEM imaging was done 48 hours after the particle treatment.

To determine the effectiveness of RA/AMSN complex on the cell conversion process, neural cell conversion was demonstrated by addition of $RA/AMSN_{19}$ or RA solution to mES cells. The amount of complex to be treated was calculated regarding on the loading capacity and release kinetics. For $RA/AMSN_{19}$, the required amount was 20 μg/mL to assure sustained release of approximately 10^{-6} M in every 2 days when intracellular uptake occurs. 20 μg/mL of $RA/AMSN_{19}$ complex was added to mES cells and media were changed to N2B27 neural growth

media without RA/AMSN$_{19}$. As a control, 3 x 10^{-6} M of RA was added to induction media and applied to mES cells. After 2 days of incubation, the media containing either RA or RA/AMSN$_{19}$ was removed and changed to N2B27 without further addition of RA. The cellular morphological change was observed every other day during the whole differentiation process (Figure 3.7). When the culture condition was changed to N2B27, the majority of the cells treated with RA or RA/AMSN$_{19}$ died, while the survived ones showed a distinct, specific morphological change by an increase in cytoplasmic portion. Specifically, cells treated with RA/AMSN$_{19}$ showed more rapid and vigorous increase in cytoplasmic portion with the distinct morphological change to fibrous structure than that of the cells treated with RA only. The overall morphology of the cells treated with only RA resembles that of mES cell colonies, indicating the 2 days of induction with RA alone is not sufficient to derive significant neural differentiation. In contrast, when the mES cells were exposed to the neural cell culture condition without RA induction, none of the cells survived.

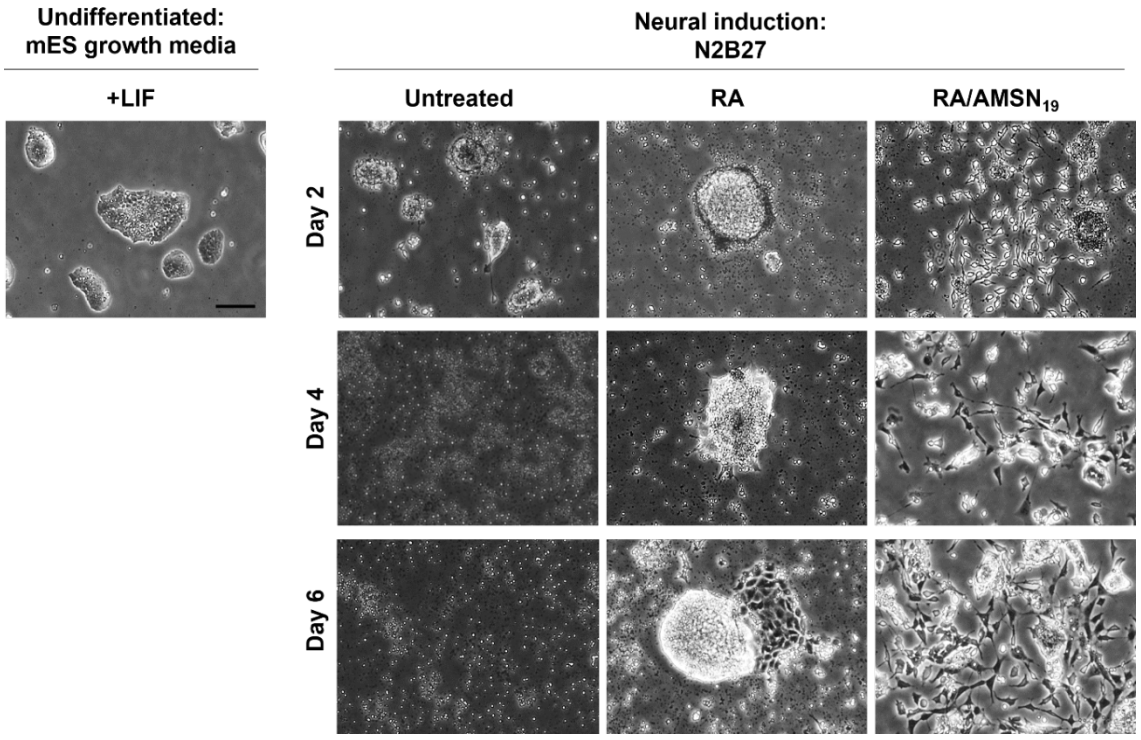

Figure 3. 7 Morphology change observation during neural induction of mES. mES cells grown under mES cell growth media supplemented with LIF was conducted as control. Neural induction samples were grown under N2B27 neural growth media, with or without supplement of RA or RA/AMSN$_{19}$. Group identification was set as followed: -RA, neural induction group without RA; +RA, neural induction group with RA; +RA/AMSN$_{19}$, neural induction group with RA/AMSN$_{19}$ complex. Scale bar indicates 500 μm.

To evaluate whether our system successfully generated neuronal cells, total RNA was isolated from each sample and gene expression of OCT4 (pluripotency marker) and β-III tubulin (also known as Tuj1, neural-specific marker) were analyzed by the RT-PCR method. Relative gene expression level analysis revealed that OCT4 was decreased in both RA and RA/AMSN$_{19}$ samples, while that of Tuj1 was increased. To be specific, the sample treated with RA/AMSN$_{19}$ for 2 days showed a dramatical increase in Tuj1 expression than that of the sample treated with only RA by approximately ~2.5 fold (Figure 3.8A, B).

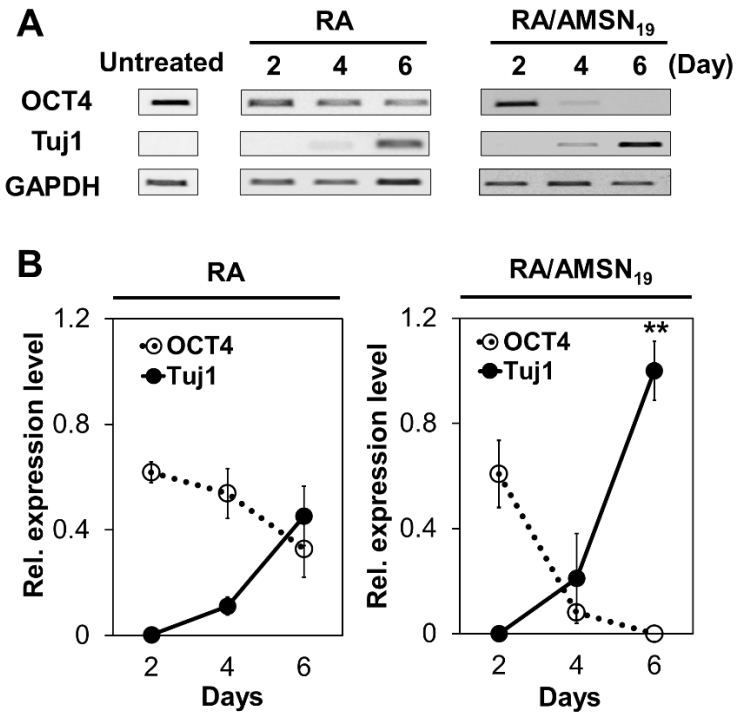

Figure 3.8 Genetic characterization of neural differentiation. (A) mRNA expression analysis along with neural induction time. The gel-based analysis was repeated 5 times and the representative images were shown. OCT4, pluripotency marker; Tuj1, neural marker; GAPDH, a housekeeping gene. Group identification was set as follows: Untreated, control mES cells without neural induction; RA, cells induced to neurological fate by the singular addition of RA; RA/AMSN$_{19}$, cells induced to neurological fate by the singular addition of RA/AMSN$_{19}$ complex. (B) Relative gene expression of OCT4 and Tuj1 against that of the housekeeping gene. Error bars indicate standard error (** for $P < 0.001$ calculated by Student's t-test, n=5).

To analyze the expression of such markers in protein level, immune staining analysis was carried out with antibodies specific to OCT4 or Tuj1. The relative marker protein expression revealed by immunocytochemistry was well correlated with the results of mRNA expression analysis. Specifically, cells treated with RA/AMSN$_{19}$ showed extremely low expression of OCT4, while that of Tuj1 was observed to be high with fibrous network-like structure (Figure 3.9). In contrast,

the cells induced with only RA maintained its colonial structures, with retained expression of OCT4. Expression of Tuj1 was observed in both the colonies and the independent single cells partially separated from the colony. Unlike that of RA/AMSN$_{19}$ treated group, Tuj1 expression was restricted to the short fibrous-structured perinuclear region of cytoplasm, with less elongating form.

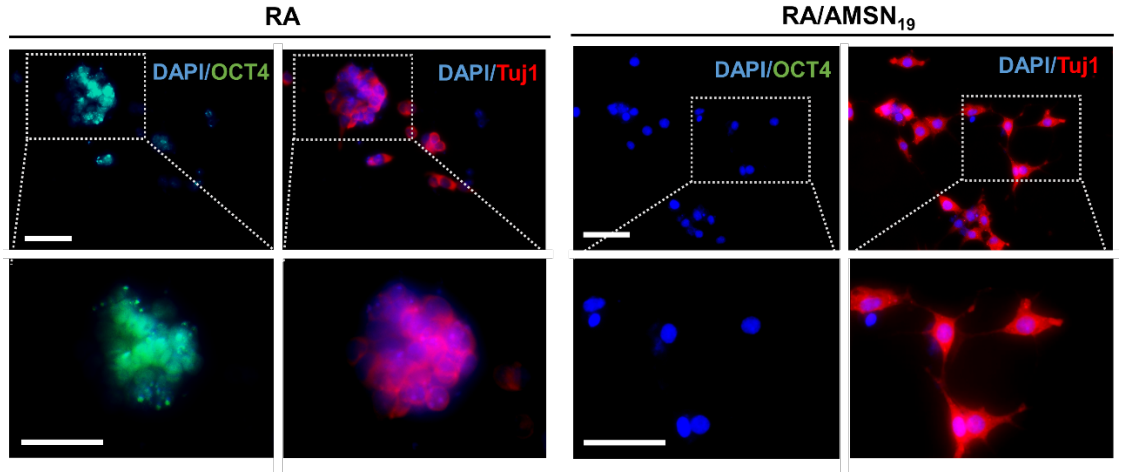

Figure 3.9 Protein-level characterization of neural differentiation. Immunocytochemistry analysis of the sample treated with only RA or RA/AMSN$_{19}$ after neural induction. Scale bars indicate 50 μm (top) and 25 μm (bottom), respectively.

Cell conversion efficiency was determined by analyzing the ratio of Tuj1-positive cells out of total cells survived after the neural induction (Figure 3.10A). Cells induced with RA/AMSN$_{19}$ showed cell conversion efficiency to nearly 90%, while that of the RA-only-treated group showed approximately 30%. Also, axonal elongation analysis revealed the quality of the converted neural cells, of which group treated with RA/AMSN$_{19}$ showed approximately 4-fold longer length of axons compared to that of the control (Figure 3.10B). Such data indicate that the singular addition of RA alone is not sufficient to meet the RA concentration threshold required to activate neural differentiation process, possibly due to a rapid clearance of free RA by media change.

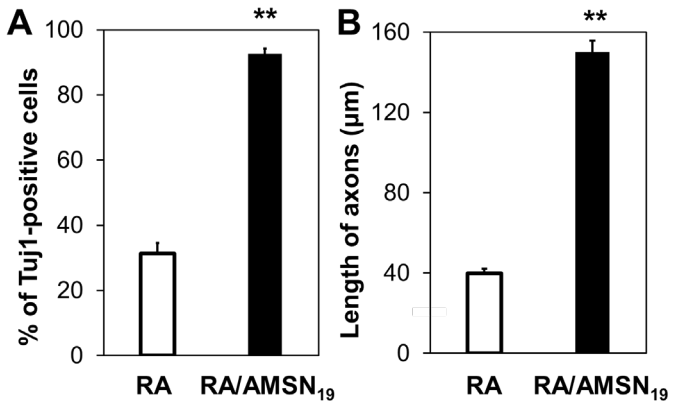

Figure 3.10 Cellular analysis of neural differentiation turnover efficiency. (A) Percentage of Tuj1-positive cells against total cells. 5 representative fluorescence images were taken for each of the experimental group and Tuj1 expression was analyzed with regard to fluorescence intensity by ImageJ program. >50 cells were counted for each image. Error bars indicate standard error (** for $P < 0.001$ calculated by Student's t-test, n=5). (B) The axonal growth of induced cells after neural differentiation. Fluorescence images were taken for each of the experimental group and axons of 50 representative cells were analyzed. The length of the axons was measured by ImageJ program with line measurement function. Error bars indicate standard error. Statistical analysis was perform with Student's t-test, ** for $P < 0.001$.

Conventional RA-mediated neural conversion methods required either labor-intensive formation of EBs or constant, repetitive addition of RA to compensate the rapid decrease in chance of interaction between RA and RAR via diffusion during the whole cell conversion process. With RA/AMSN19, however, only 2 days of incubation under complete media after a single incorporation of the complex was enough to induce neural differentiation of mES cells within 6 days. Such results indicate that with the aid of AMSN19 amount of intracellular RA supplement could be easily satisfied with the specific threshold of RA concentration required for efficient initiation of neural conversion than that of the conventional method. It is considered that AMSN19 effectively adsorbed RA on the surface and intra-pore area to derive high loading capacity, followed by stable intracellular delivery and sustained, stable release of RA nearby perinuclear region over time which led to an acceleration of neural induction. Moreover,

neurologically induced cells by RA/AMSN$_{19}$ adapted well under neural growth media and expressed neural-specific gene marker with higher expression level than that of the cells treated with RA alone by ~2.5 fold. Such data indicate that RA/AMSN$_{19}$ successfully induced initiation of neural differentiation on mES cells more efficiently than RA alone, presumably by increasing the chance of valid interaction between RA and its nucleus membrane-bound receptor with sustained RA release capability of AMSN$_{19}$ inside cells.

3.3 Discussion

The nanoparticle was synthesized from biocompatible silica via simple and cost-effective process, which possesses unique properties such as tunable pore size, high loading capacity and a broad range of modification on the surface chemistry. By use of the pore expanded, surface modified MSN, our system successfully facilitated the neural differentiation process of mES cells with the efficient intracellular delivery of the neurotrophic ligand to activate the associated neural signal pathway.

The present study is one of the various applications of our nanoparticle-based cell conversion system. Considering the wide range of intracellular-deliverable functional materials with MSN suggested from the previous studies, however, it is highly convincible that our system can also be combined with other cell conversion factors after appropriate surface modification and pore-size control of MSN. The various association may be involved with not only traditional cell conversion factors such as transgenes but also functional biomolecules, to induce specific expression of signal cascades directed to desired cell conversion. The process may require the multiple, simultaneous interactions of the chemicals and biomolecules ‘at the right place at the right time’. Considering such demand, our MSN-based system would be further evolved as an intracellular docking system for the delivery of multiple factors.

3.4 Materials and Methods

Materials and reagents

Cetyl trimethyl ammonium bromide (CTAB) was purchased from Acros (New Jersey, USA). 3-Aminopropyltriethoxysilane (APTES), tetramethyl orthosilicate (TMOS), toluene, dimethylsulfoxide (DMSO), mesitylene (trimethyl benzene, TMB), HOECHST 33342, retinoic acid (RA), and beta-mercaptoethanol, mitomycin C, primary rabbit anti-mouse Tuj1, secondary anti-rabbit IgG were purchased from Sigma-Aldrich (St.Louis, MO, USA). Sodium hydroxide was purchased from Junsei Chemical Co. (Tokyo, Japan). All reagents were used as received without further purification. DMEM (Dulbecco's Modified Eagle's Medium), 0.25% trypsin-EDTA solution and PBS (pH 7.4) were purchased from WelGENE Inc. (Daegu, Korea). CCK-8 (Cell Counting Kit-8) was purchased from Dojindo Molecular Technologies, Inc. (Rockville, MD, USA). ES-qualified FBS was purchased from Biowest (Riverside, MO, USA). Leukemia inhibitory factor (LIF) was purchased from Peprotech Inc. (Rocky Hill, NJ, USA). Superscript™ reverse transcriptase, N2 media supplement, B27 media supplement, neurobasal media, DMEM/F12, GlutaMAX™, and non-essential amino acid (NEAA) were purchased from Thermo Fisher Scientific Inc. (Waltham, MA, USA). Primers for RT-PCR were purchased from Cosmo Genetech. Inc. (Seoul, Korea). Mouse embryonic stem (mES) cell line and STO cell line were purchased from ATCC Inc. (Manassas, VA, USA). Primary rabbit anti-human/mouse OCT3/4 was purchased from R&D Systems (Minneapolis, MN, USA). Vectashield™ mounting solution containing DAPI was purchased from VWR (Radnor, PA, USA). EmbryoMAX® 0.1% gelatin solution was purchased from Millipore Inc. (Darmstadt, Germany).

Preparation of MSN_2, $AMSN_{19}$ and $TAMSN_{19}$

To prepare MSN, 3.94 g of CTAB dissolved in 1M NaOH solution was added to

methanol/water solution, followed by aging overnight after adding 1.3 mL of TMOS to a mixed solution with vigorous stirring for 10 min. The synthesized MSN was filtrated with 200 nm membrane after centrifugation and washing by using ethanol and water more than three times. The collected product MSN_2 was named after its pore size. To expand the pore size of MSN_2, 20 mL of 1:1 mixture (v/v) TMB and water were added to MSN dissolved in ethanol and then the mixed solution was placed in an autoclave at 140°C for 2 days. The resulting white powder was washed with ethanol and water 5 times each. To remove the template, 12 M of HCl was added to MSN suspension dissolved in ethanol and the mixed solution was placed in an autoclave at 140°C overnight to derive MSN_{19}. To prepare amine functionalized MSN ($AMSN_{19}$), the template extracted product was suspended in 10 mL of toluene, followed by the addition of 1 mL of APTES. The suspension was refluxed overnight and then the mixture was filtered and washed with ethanol and water. The resulting product was dried and collected with white powder. For the preparation of TAMRA-conjugated $AMSN_{19}$ ($TAMSN_{19}$), $AMSN_{19}$ was suspended in DMSO (30 mg/mL) and 10 μL of N-hydroxysuccinimyl (NHS) ester-activated carboxytetramethylrhodamine (TAMRA-NHS) solution (2.5 μg/mL) was added to the suspension. After horizontal shaking at room temperature for 3 h, the product was centrifuged and washed with ethanol and water over 5 times. The resulting product was dried and collected as pinkish powder, which was dissolved in water for $TAMSN_{19}$ working solution.

Characterization of MSN2 and $AMSN_{19}$

The pore size, surface area, and pore volume of the MSN particles were analyzed through nitrogen sorption experiments. Nitrogen adsorption isotherms were obtained by using a NOVA Surface Area Analyzer (Nova 2200e, Quantachrome instrument, USA). Prior to the measurements, the samples were degassed for 12 h

at 573 K. The specific surface area was calculated by the Brunauer-Emmett-Teller (BET) equation using the adsorption data obtained in the pressure range P/P0 = 0.05 ~ 0.2, whereas the pore size distribution was analyzed with the adsorption branch of the nitrogen adsorption isotherm according to the Barrett-Joyner-Halenda (BJH) algorithm. The morphological study was carried out by using transmission electron microscopy (TEM, LIBRA 123, Carl Zeiss) and zeta potential was measured by zeta sizer NS90 (Malvern, UK).

Preparation of RA solution

1M RA stock solution was prepared by dissolving RA powder with DMSO and its 10ul-aliquots were covered with foil to avoid photo-induced isomerization and oxidation and stored in -20 ℃. The working solution was freshly made every 2 weeks with optimized dilution process of the stock solution with 100% ethanol. For the derivation of a standard curve of UV intensity against RA concentration, various concentration of RA solution was prepared and each of their UV spectra was measured with UV spectrometer. Then the standard curve equation was derived by plotting maximum UV absorption value of each spectrum at 350 nm against the corresponding RA concentration.

RA loading test on MSNs

For investigation of RA loading capacity, 100 μg $AMSN_{19}$ was soaked into RA solutions in 100% ethanol in various concentrations and incubated at RT up to overnight. MSN_2 was treated as same as $AMSN_{19}$ for a control group. Incubation was done under the dark condition to ensure RA stability. Loading capacity was determined by comparison of UV absorption spectrum of each sample. For stability test, UV absorption analysis before and after vigorous mechanical stimulation via vortex was done.

RA release test on MSNs

For investigation of RA release kinetics, each RA/MSN complex generated from 4-hour incubation in RA solution was then suspended in 5% ethanol solution in PBS and incubated at 37 ℃ conditions for up to 10 days. The calculated value of RA released from the complex was derived by analyzing the change in UV adsorption value at 350 nm of the supernatant RA solution of each sample. The UV adsorption peak value was measured every other day, and the calculated amount of RA was summated to each of the previous data.

mES cell culture, maintenance, and preparation of feeder-free culture system

Prior to mES culture, feeder cells were prepared by treating mitomycin C to STO cell line and plated onto T-25 flask. The cells were cultured with mES culture basal media, containing ES-qualified FBS, β-mercaptoethanol, and nonessential amino acid. After 24 hours, mES cells were thawed and plated onto the feeder cells and cultured with complete mES media with the addition of LIF until the colonial formation of the cells were stabilized. mES cells were maintained under feeder-dependent culture system to ensure stable undifferentiated state during conventional culture state. For the research, mES cell culture system was changed to the feeder-free system. Cells were treated with 0.25% trypsin and plated onto 0.1% gelatin-coated 60mm culture dish, followed by repetitive subculture for every 2 days onto a gelatin-coated dish to eliminate feeder cell layer.

Cytotoxicity test

mES cells were seeded on the gelatin-coated 96-well plate and cultured with conventional mES culture media for 24 hours. $AMSN_{19}$ or $RA/AMSN_{19}$ was treated to the culture plate in a various concentration ranging from 0~50 ug/mL and incubated for 48 hours on 37℃, 5% CO_2 condition. After incubation, cells were washed twice with PBS and added to complete mES media mixed with 10% CCK-8 reagent, followed by 1~4 hour incubation in the conventional cell culture

condition. The quantitative analysis on the change in colorimetric intensity was done by measuring the optical density of formazan salt at 450nm with a microplate reader (Molecular Devices, Inc., USA). The experiment was carried out in triplicate, of which data were shown as mean ± SEM.

Intracellular uptake test

mES cells were seeded on the gelatin-coated plate and cultured with conventional mES culture media for 24 hours. For intracellular uptake test, $AMSN_{19}$ labeled with TAMRA dye ($TAMSN_{19}$) was used. $TAMSN_{19}$ was made by previously optimized methods and treated on the plated mES cells and incubated for 48 hours in 37℃, 5% CO_2. Prior to the sampling, cells were treated with HOECHST 33342 for nuclear staining, and the media was removed after 15 minutes. Then the cells were washed twice with PBS and fixed with 4% paraformaldehyde. Each colony was observed with Deltavision (GE healthcare) to verify intracellular uptake of $TAMSN_{19}$ within colonies. Images were repeatedly gained at various planar orthogonal to the z-axis. Fluorescence correlation analysis was done by line profiling of the z-sectioned image #3, which showed the clearest image of the nucleus and the nanoparticle within the colonial structure.

Neural differentiation of mES cells

Neural induction of mES cells was performed with either addition of only RA or RA/$AMSN_{19}$ complex. Specifically, 10^{-6} M RA or 25 μg RA/$AMSN_{19}$ (corresponding to 3 x 10^{-6} M of RA included) was treated with mES cells with complete mES media for 2 days. Groups without any induction were cultured as a negative control. After 2 days, the media was changed to neural cell culture media N2B27. Media was changed every other day.

RT-PCR

RNA was isolated from each sample with TRIZOL reagent, followed by cDNA

synthesis aided by Superscript™ reverse transcriptase according to the instruction manual. For target gene amplification, each primer was designed in consideration of GC content less than 50% and overlapping between two exons of the target genes. Primer sequence was confirmed as follows: for OCT4, 5'-GCTCAGCCTTAAGAACATGTGTAAGC-3' was used as forward and 5'-GCCTCATACTCTTCTCGTTGGGA-3' for reverse primer. For Tuj1 gene, 5'-TCAGCGATGAGCACGGCATA-3' for forward and 5'-CACTCTTTCCGCACGACATC-3' for reverse primer were used. PCR analysis was done with optimized annealing temperature condition ranging from 50 to 60.

Immunocytochemistry

For immunocytochemistry, mES cells were plated onto gelatin-coated cover glass and treated with either RA or RA/MSN, followed by the neural differentiation process previously stated. After fixation with 4% paraformaldehyde, cells were blocked by treating 10% (v/v) FBS and 0.01% (v/v) Tween-20 in PBS for 30 minutes, followed by overnight incubation with primary antibodies (Tuj1: Rat anti-Tuj1, 1:200 / OCT4: Rabbit anti-OCT4, 1:100) at 4℃. After washing with PBS twice, secondary antibody corresponding to each of the primary antibodies was applied (Anti-Rat IgG, 1:1000 / Anti-rabbit IgG, 1:1000). After 2-hour incubation at RT, samples were rinsed twice with PBS and each cover glass was removed from culture plate and mounted to slide glass with Vectashield™ mounting solution containing DAPI.

3.5 Conclusion

In conclusion, we introduced an improved method for the *in vitro* demonstration of the RA-mediated neuronal differentiation from the mouse embryonic stem cell colony, with the incorporation of $AMSN_{19}$ as the intracellular delivery carrier. We expect that our system would attribute to providing more options to facilitate the successful cell in the complicated cell conditions, leading to the derivation of meaningful fundamental studies in the near future.

3.6 Reference

1. Corcoran, J.; Maden, M., *Nat Neurosci* **1999,** *2* (4), 307-308.

2. Corcoran, J.; Shroot, B.; Pizzey, J.; Maden, M., *J Cell Sci* **2000,** *113* (14), 2567-2574.

3. Corcoran, J.; So, P. L.; Barber, R. D.; Vincent, K. J.; Mazarakis, N. D.; Mitrophanous, K. A.; Kingsman, S. M.; Maden, M., *J Cell Sci* **2002,** *115* (19), 3779-3786.

4. Strubing, C.; Ahnerthilger, G.; Shan, J.; Wiedenmann, B.; Hescheler, J.; Wobus, A. M., *Mech Develop* **1995,** *53* (2), 275-287.

5. Bain, G.; Kitchens, D.; Yao, M.; Huettner, J. E.; Gottlieb, D. I., *Dev Biol* **1995,** *168* (2), 342-357.

6. Fraichard, A.; Chassande, O.; Bilbaut, G.; Dehay, C.; Savatier, P.; Samarut, J., *J Cell Sci* **1995,** *108*, 3181-3188.

7. Wang, X.; Yang, P., *J Vis Exp* **2008,** (17).

8. Ying, Q. L.; Stavridis, M.; Griffiths, D.; Li, M.; Smith, A., *Nat Biotechnol* **2003,** *21* (2), 183-6.

9. Ete Z. Szuts, F. I. H., *Archives of Biochemistry and Biophysics* **1991,** *287* (2), 297-304.

10. Okada, Y.; Shimazaki, T.; Sobue, G.; Okano, H., *Dev Biol* **2004,** *275* (1), 124-42.

11. Jing Xu, H. W., Tao Liang, Xiangsheng Cai, Xiurong Rao, Zhenbo Huang, Guoqing Sheng, *Mol Biol Rep* **2012,** *39*, 789-795.

12. Tiago Santos, R. F., Joao Maia, Fabienne Agasse, Sara Xapelli, Luısa Cortes, Jose´ Braganca, Joao O. Malva, Lino Ferreira, Liliana Bernardino, *Acs Nano* **2012,** *6* (12), 10463-10474.

13. Joa˜o Maia, T. S., Sezin Aday, Fabienne Agasse, Luı´sa Cortes, Joa˜o O.

Malva, Liliana Bernardino, Lino Ferreira, *Acs Nano* **2011,** *5* (1), 97-106.

14. Ku, B.; Kim, J. E.; Chung, B. H.; Chung, B. G., *Langmuir* **2013,** *29* (31), 9857-9862.

15. Seo, H. I.; Cho, A. N.; Jang, J.; Kim, D. W.; Cho, S. W.; Chung, B. G., *Nanomedicine-Nanotechnology Biology and Medicine* **2015,** *11* (7), 1861-1869.

16. Han, D. H.; Na, H. K.; Choi, W. H.; Lee, J. H.; Kim, Y. K.; Won, C.; Lee, S. H.; Kim, K. P.; Kuret, J.; Min, D. H.; Lee, M. J., *Nat Commun* **2014,** *5*, 5633.

17. Mi-Hee Kim, H.-K. N., Young-Kwan Kim, Soo-Ryoon Ryoo, Hae Sung Cho, Kyung Eun Lee, Hyesung Jeon, Ryong Ryoo, Dal-Hee Min, *Acs Nano* **2011,** *5* (5), 3568-3576.

18. Na, H. K.; Kim, M. H.; Park, K.; Ryoo, S. R.; Lee, K. E.; Jeon, H.; Ryoo, R.; Hyeon, C.; Min, D. H., *Small* **2012,** *8* (11), 1752-61.

19. Sharow, K. A.; Temkin, B.; Asson-Batres, M. A., *Int J Dev Biol* **2012,** *56* (4), 273-8.

Chapter 4. Non-viral, direct neuronal reprogramming from human fibroblast using a polymer-functionalized nanodot

4.1 Introduction

Throughout the lifetime, the gradual loss of the neural network has been considered as an inevitable event. Severe neural loss may lead to numerous brain-associated dysfunctions, including the loss of memory and language impairments[1]. It is expected that more than 50 million people in the United States suffer from neurological dysfunction, and the expenses required for the treatment would record as high as approximately $500 billion[2]. To combat such problems, several studies have focused on the cell replacement strategy such as the replacement of the injured neurons to healthy neurons[3]. As the concept of cell reprogramming has drawn much attention recently, there have been numerous efforts to generate the rare functional cells in high demand from the abundant easy-to-obtain somatic cells[4]. Among various cell engineering strategies, direct cell reprogramming has gained much interest due to its unique cellular mechanism. Unlike transdifferentiation, which bypasses the pluripotent state to induce the desired cell fate, direct reprogramming involves the generation of the intermediate multipotent precursor cells. In other words, direct reprogramming is the cellular engineering process that involves the intermediate 'breakpoint' before the final differentiation stage[5].

To accomplish the successful artificial control of the desired cell fate, it is required to develop the promising intracellular gene delivery reagent which would ensure the stable transfection. Virus-originated vectors have been used most frequently due to their high transfection efficiency, hence the intrinsic limitations

including the tumorigenesis are yet to be overcome[6]. On the other hand, non-viral vectors with the application of the cationic polymers and liposome-like materials have drawn much attention as the alternatives, but several drawbacks have been constantly depicted including the high toxicity issues and relatively low transfection efficiency[7, 8]. Besides, although liposomal materials have been practically used, several specific concerns are still on debate considering the instability in the colloidal solution, low loading capacity, and short circulation half-life.

Regarding the history of the transfection reagent, it has not been long since the concept of the nanomaterial-based intracellular delivery carrier has emerged. When the materials turn into a nano-size, various unexpected properties that differ from those of the originals in bulk could be revealed[9, 10]. Carbon-sourced nanodot, for example, has primarily drawn attention for its unique optical properties and considered as one of the upcoming promising candidates applicable to the energy conversion [11] or optoelectronic devices [12]. Recently, various fabrication methods of the nanoparticle have been proposed to enhance the biocompatibility [13] or the loading capacity[3, 14-16]. Since then, numerous attempts have been made to apply the functionalized carbon nanodots to the fields of biotechnology, including biosensor for imaging and the drug delivery carrier biomolecules [17-23]. Nevertheless, it has not been fully guaranteed whether the carbon dot could be further utilized as the reliable transfection reagent applicable for cell engineering. Here, we developed a polymer-modified nano-reagent (**Poly**mer-functionalized **N**anodot, **PolyN**) for the safe and highly efficient, non-viral direct cell reprogramming (Scheme 4.1). We demonstrated a direct reprogramming of human fibroblast to a neuron-like cell, incorporating a single reprogramming factor *SOX2* with PolyN. PolyN enabled a highly efficient intracellular delivery and semi-long-

term expression of the functional transgene in the human fibroblast. In this paper, we discuss distinct pieces of evidence to claim that a single induction of the spontaneous, transient gene expression by PolyN is sufficient to support the whole process of the direct cell reprogramming.

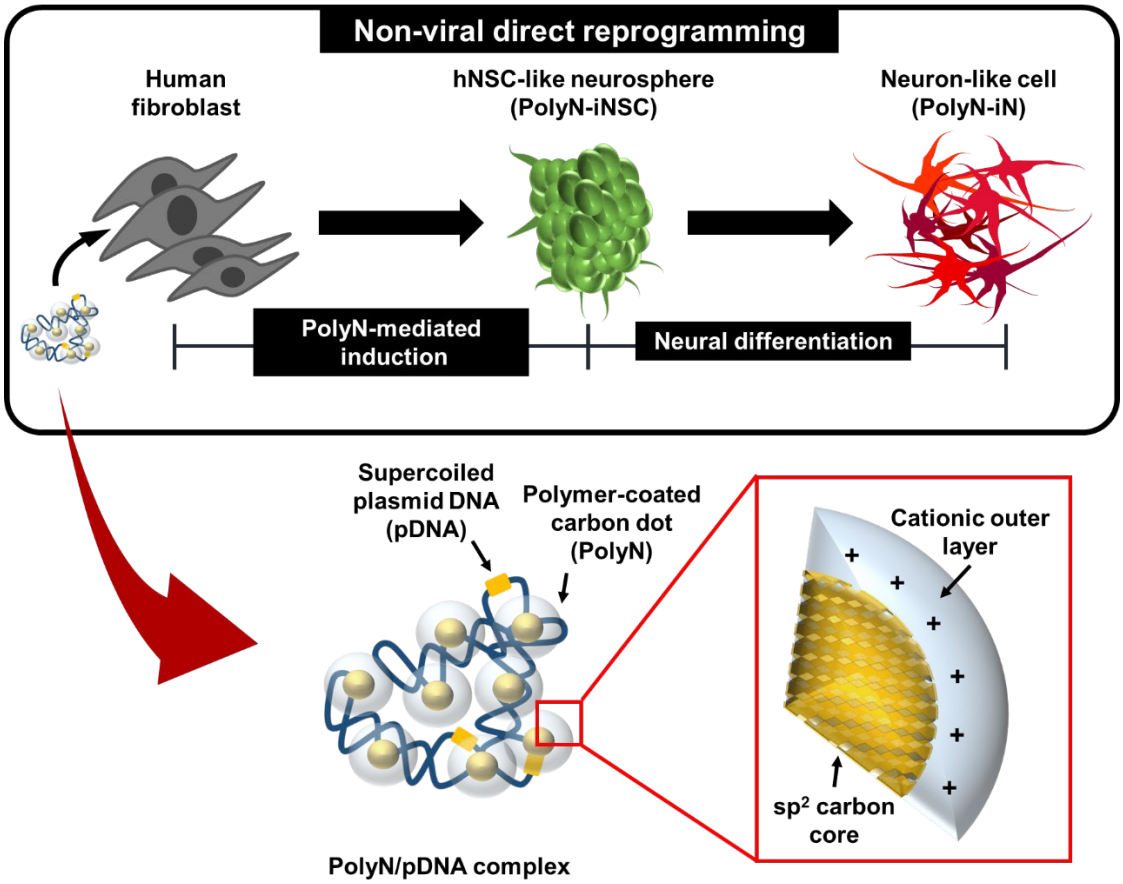

Scheme 4. 1 A novel polymer-functionalized nanodot (PolyN) showed successful performance on the stable, non-viral intracellular transgene delivery.

4.2 Result

Synthesis of PolyN consisted of a biocompatible carbon source material (citric acid), and the cationic polymer (PEI, 25 kDa) for the endowment of the surface functional groups (Scheme 4.2). It has been reported that the cytotoxicity and the endocytotic ability of a cationic polymer are directly proportional to its size (including polymer length and dimensional factors) [24]. We hypothesized that if we could functionalize the cationic polymer around the nano-sized particle, it may relieve the membrane stress while the endocytosis is proceeded and increase the cell viability. In this regard, we intended to generate a particle in size of less than ~20 nm in diameter with polymeric moieties remaining at the surface, as if the cationic polymers are surrounding the carbon core. An instant and spontaneous hydrothermal reaction associated with the carboxylic acid group and the imine group was believed to be the key to ensure the successful synthesis of the nanomaterial we desired. To realize this, we chose to adopt the microwave-based method and adjust the reaction time under 10 minutes.

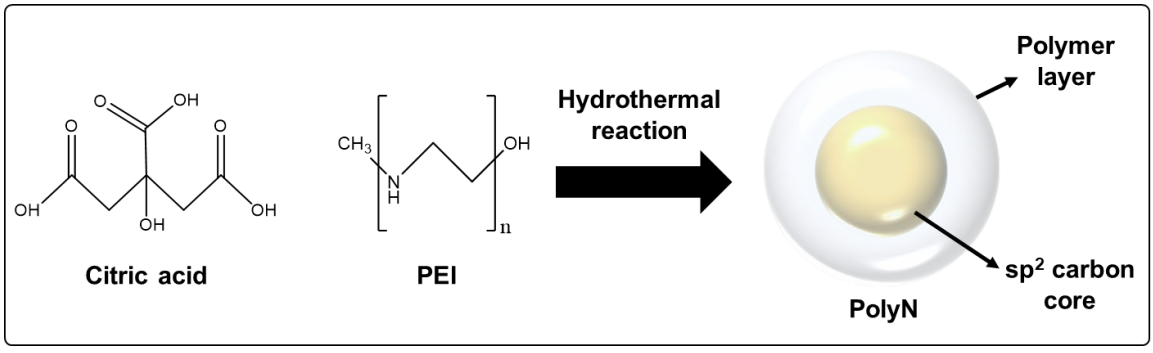

Scheme 4.2 Overall scheme illustrating the synthesis method of PolyN.

The synthesized PolyN particles were stably dissolved in the aqueous form, resulting in the transparent yellowish solution without any precipitation under room temperature. Moreover, exposure to UV light irradiation led to the distinct blue-luminescence of the particle solution. The specific optical property of PolyN

could be interpreted by the UV-Vis absorption spectra, which showed a distinct shoulder at ~230 nm associated with the π–π* transition of the carbonized core aromatic region [25], and a sharp peak at 360 nm which indicates the n- π* transition of the surface functional groups [26] (Figure 4.1A). 3D Photoluminescence profile scanning of PolyN showed distinct fluorescence peaks, which shared the same maximum emission peak around the wavelength of 450 nm (Figure 4.1B). In detail, the difference between the major and the minor peaks was shown at the maximum excitation wavelength, of which the major was recorded at 360 nm while that of the minor was around 260 nm.

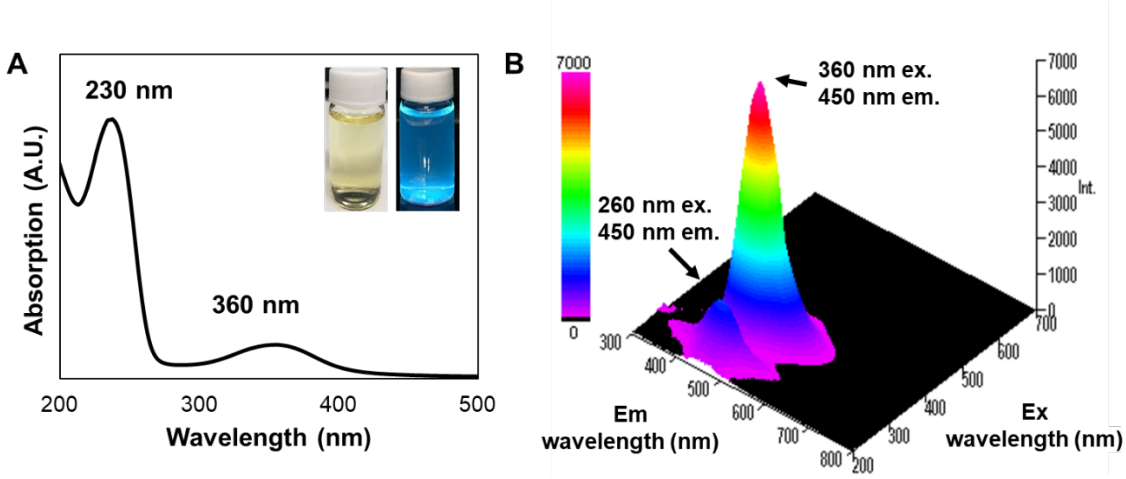

Figure 4.1 Characterization of the synthesized PolyN (I). (A) Absorption property of the PolyN under UV/VIS spectrophotometry. (B) 3D Photoluminescence profile scanning of PolyN. The wavelength range is shown as follows; 200~700 nm for the excitation, 300~800 nm for the emission.

Next, the overall spherical morphology of the particle could be observed by HR-TEM (Figure 4.2A). No signs of any lattice-like parameters were detected, indicating that the synthesized PolyN has the property of an amorphous carbon dot. The size distribution of PolyN ranged from 2 nm to approximately 10 nm (with an average of 6.04±0.23 nm), which was the ideal size range we expected. Raman spectra analysis clearly showed the D peak and G peak, which refers to the

sp^2 hybridization (Figure 4.2B).

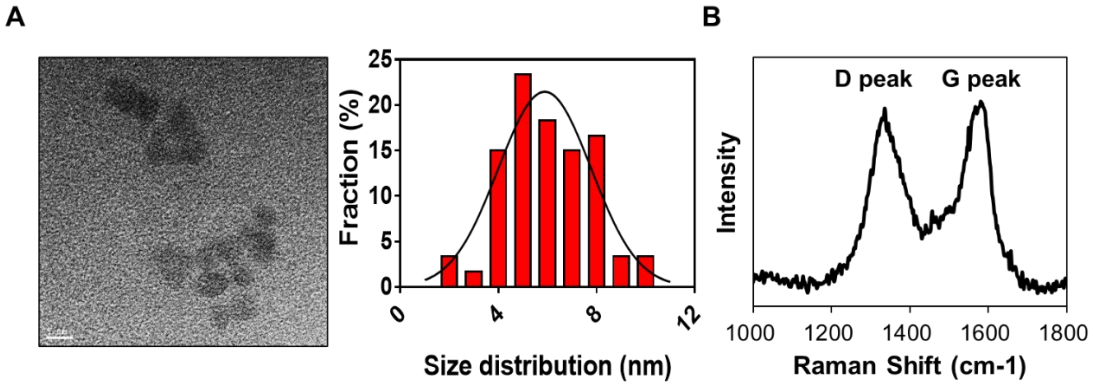

Figure 4.2 Characterization of the synthesized PolyN (II). (A) Morphological analysis of PolyN by HR-TEM. The representative image is shown. The size bar indicates 5 nm. The particle size distribution was analyzed by Image J (n=60 particles). (B) Raman spectroscopy showing the D peak and G peak indicating the formation of the sp^2 carbon.

Moreover, FT-IR spectra analysis not only revealed several representative peaks assumed to be derived from the precursor molecules such as 1020~1250, 1375, and 1705 cm^{-1} representing the C-N stretching, C-H bending, C=O stretching, respectively, but also several specific peaks including 1558 cm^{-1} indicating C=C stretching of the aromatic group and a broad absorption band at 2500-3500 cm^{-1} attributed to –OH stretching as well (Figure 4.3). The overall set of data indicates that the PolyN was proven to possess the broad features of a typical carbon-sourced nanodot, including the unique optical properties.

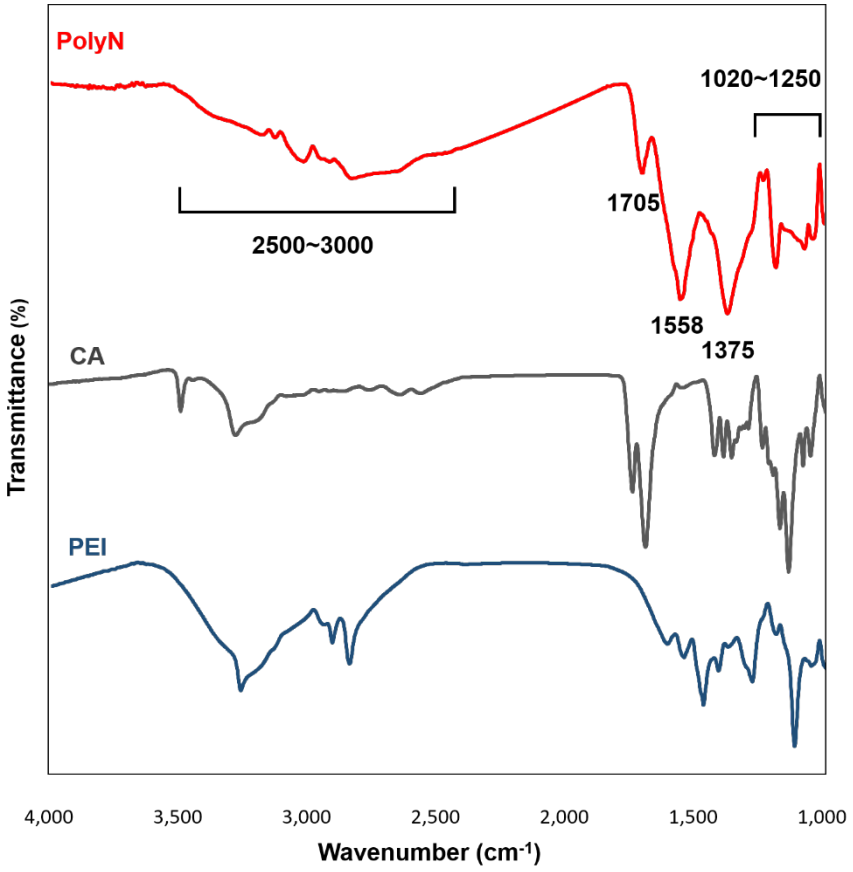

Figure 4.3 FT-IR comparison of PolyN. Comparison analysis of the FT-IR peaks of the synthesized PolyN and the precursor candidates (PEI: polyethyleneimine, CA: citric acid). Representative peaks indicating functional groups as follows: the range of 1020-1250 cm^{-1} for the C-N bond of the amine groups; 1375 cm^{-1} for the C-H bending in alkane groups; 1558 cm^{-1} for the N-H bending in the primary and secondary amine groups and C=C streching in aromatic groups; 1705 cm^{-1} for C=O in the carboxylic acid groups; and broad absorption at 2500~3000 cm^{-1} for –OH stretching in carboxylic groups.

Also, the surface charge of the carbon dot fabricated with citric acid alone (CD from CA), raw PEI, and PolyN was determined by zeta potential analysis (Figure 4.4). Compared to that of either CD from CA or raw PEI, PolyN showed moderately positive charge on average of 8.4 ± 1.2 mV. Such data indicate that the administration of PEI in the particle synthesis endowed the positive surface charge to the product (PolyN), allowing the complex formation with the negatively

charged pDNA.

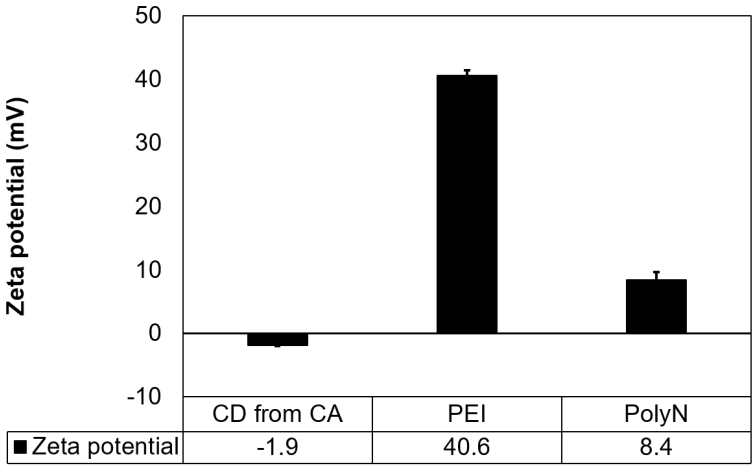

Figure 4.4 Zeta potential analysis of the particles. Comparison of the zeta potential of carbon dot fabricated from citric acid alone (CD from CA), raw PEI, and PolyN.

Followed by the characterization of the synthesized PolyN, we then investigated its potent capability as a gene carrier (Figure 4.5A). Raw PEI was used as a control, for its conventional utilization as the daily non-viral transfection reagent. A fixed amount of each reagent was used to make a complex with the reporter gene-inserted recombinant plasmid DNA (pGFP) in various ratios. It was revealed that 1 μg of PolyN was feasible to carry a maximum of 25 ng of pGFP, which was approximately 2.5-fold higher than that of the raw PEI (Figure 4.5B).

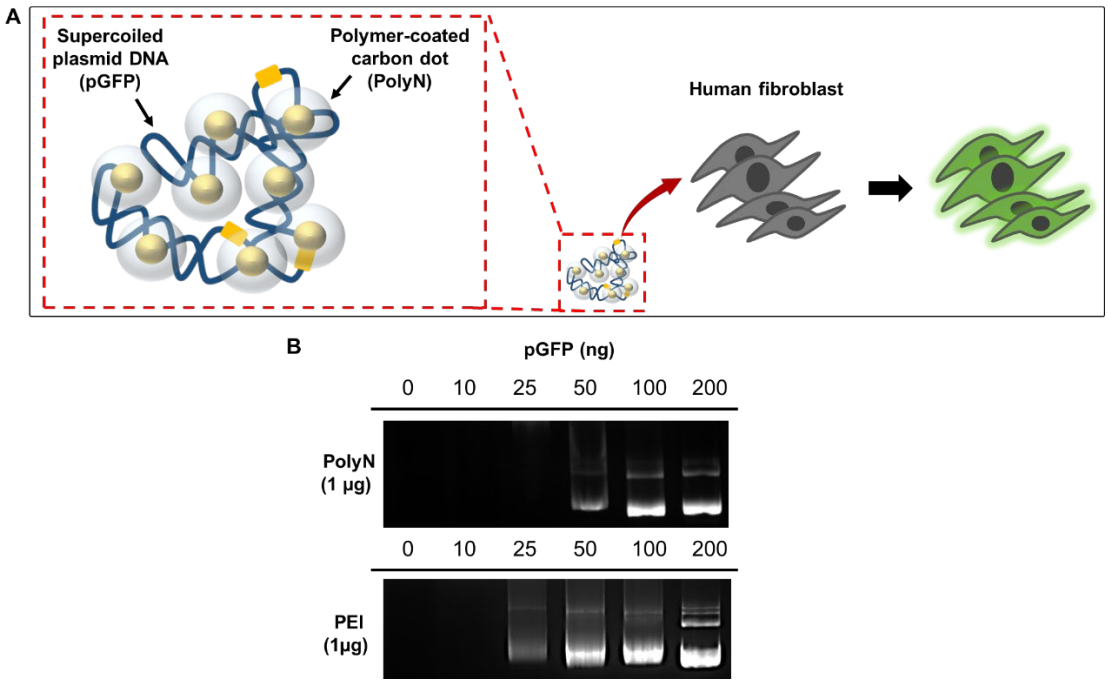

Figure 4.5 Non-viral intracellular gene delivery with PolyN. (A) Schematic illustration of the PolyN-mediated non-viral gene delivery. (B) Comparison of the loading capacity of PolyN and raw PEI against pGFP.

We made the PolyN/pGFP complex with a fixed ratio of 1:25 (μg PolyN: ng pGFP) and named it as a '1 complex unit (CU)'. The surface charge of each complex was also examined (Figure 4.6). Unlike that of PEI/pGFP, which showed a substantially positive surface charge of 35.5 ± 0.4 mV, PolyN/pGFP complex showed a nearly neutral surface charge of 0.8 ± 0.4 mV.

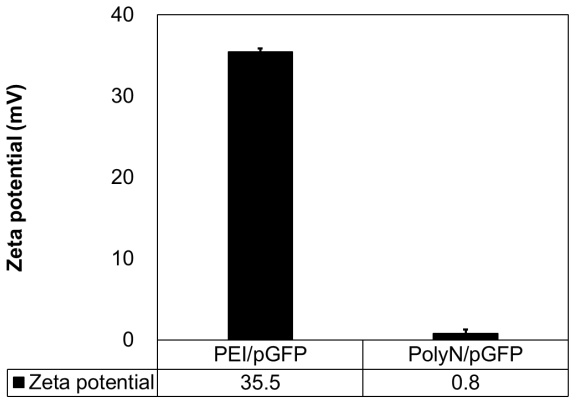

Figure 4.6 Comparison of the zeta potential between PEI/pGFP complex and PolyN/pGFP complex.

To further determine the cell viability and transfection efficiency, model cell-based tests were performed. Human fibroblast (HF) was adopted for the model cell in each test. First, for the evaluation of the cell viability, each material (raw PEI, PolyN, PEI/pGFP, and PolyN/pGFP) was treated in serial concentration to HF. It was revealed that both PolyN and PolyN/pGFP complex showed significantly higher cellular viability than those of the PEI and PEI/pGFP complex, respectively (Figure 4.7).

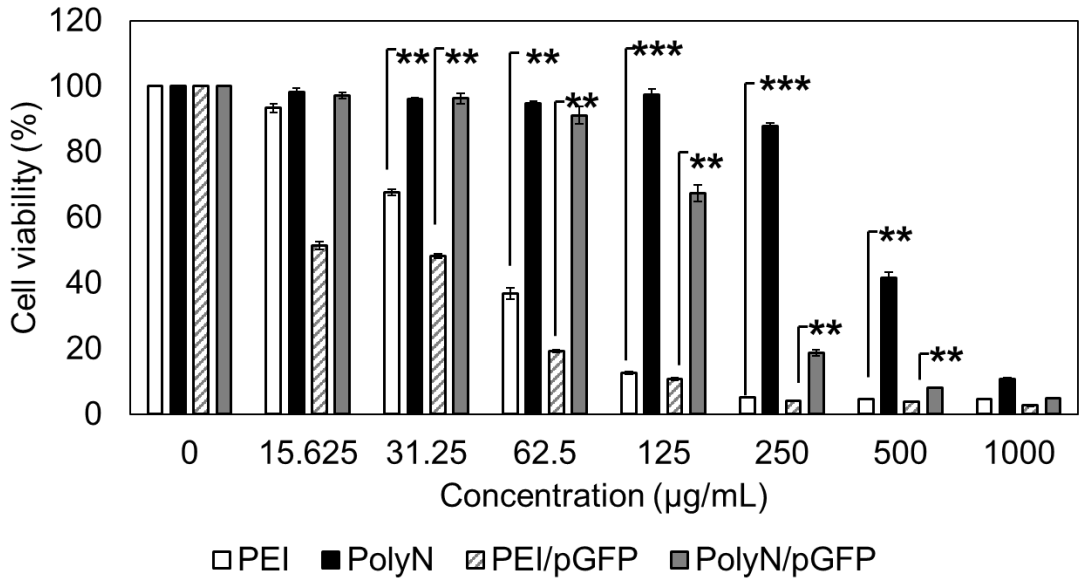

Figure 4.7 Cell viability of raw PEI, PolyN, and their complex form with pGFP (PEI/pGFP, PolyN/pGFP) administered to HF. The comparison was done between the raw PEI and PolyN, PEI/pGFP, and PolyN/pGFP complex, respectively. Bars indicate mean ± SEM, from three individual replicates in each group (n=3) unless stated otherwise. To determine the significance of the data, one-way ANOVA was performed to derive p-value. ** or *** indicates the significance of each cell viability of the PolyN and PolyN/pGFP complex compared to that of the PEI and PEI/pGFP complex as control, respectively; ** for $p \leq 0.01$ and *** for $p \leq 0.001$.

Next, for the analysis of transfection efficiency involving PolyN, a reporter gene delivery test was performed. 20 CU of PolyN/pGFP complex was treated to HF,

which showed almost 100% cell viability according to the plotted data in Figure 4.7. As a positive control, PEI/pGFP was treated in the confined condition which was preliminarily determined according to the instruction manual. After 72 hours of incubation, we observed the cells with an optical microscope to investigate the cellular morphology and qualitative gene expression (Figure 4.8A). The overall tendency of the cytotoxicity showed a high correlation with the previous cell viability analysis. In brief, compared to cells treated with raw PEI or PEI/pGFP complex, those treated with either the PolyN alone or the PolyN/pGFP complex significantly maintained their viability under each optimized transfection condition. To our surprise, when the cells were treated with PolyN/pGFP complex, the reporter gene expression was significantly enhanced compared to that of the PEI/pGFP group. Moreover, flow cytometry analysis revealed that PolyN facilitated the efficient reporter gene expression up to 40.8 %, which was over 2-fold higher than that of the PEI/pGFP group (Figure 4.8B).

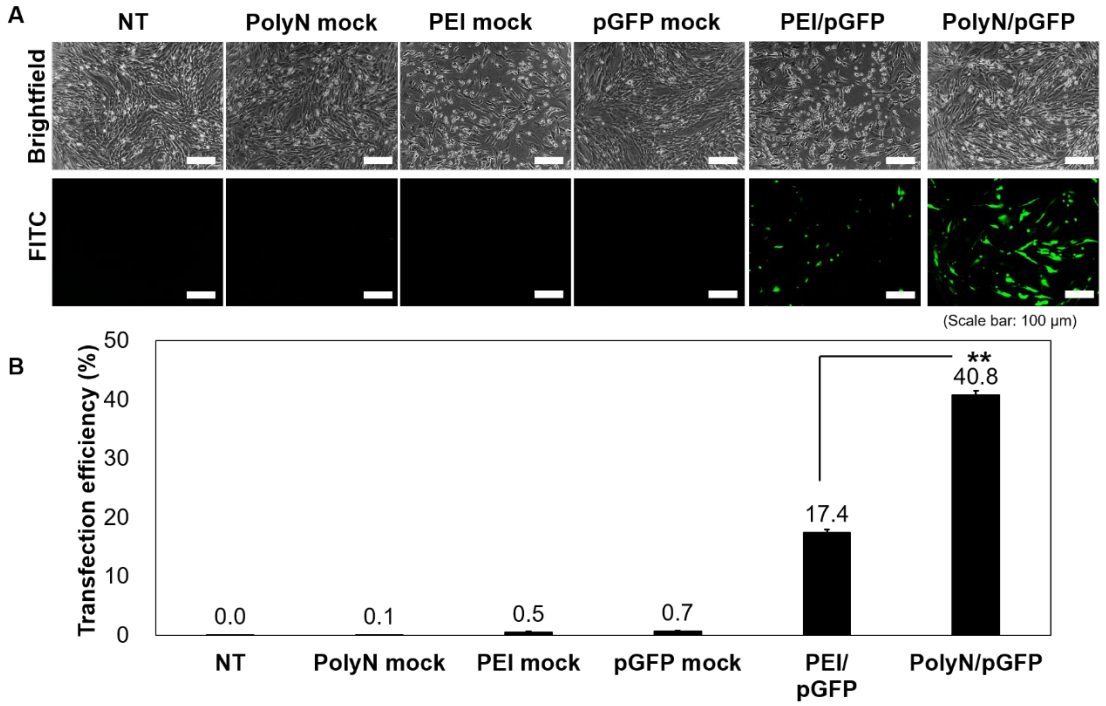

Figure 4.8 Reporter pDNA (pGFP) transfection analysis with PolyN, with comparison to PEI. (A) Optical observation of the reporter gene (GFP) expression.

NT, non-transfected control; PolyN mock, treated with only PolyN particle; PEI mock, treated with only PEI; pGFP mock, treated with only plasmid DNA encoding GFP (pGFP); PEI/pGFP, transfected with pGFP loaded on PEI; PolyN/pGFP, transfected with pGFP loaded on PolyN particle. White bars indicate 100 μm. (B) Comparison of the transfection efficiency by flow cytometry. Each value of the transfection efficiency is labeled on the graph. Bars indicate mean ± SEM, from three replicates for each group (n=3). To determine the significance of the data, one-way ANOVA was performed to derive p-value. ** indicates the significance of the transfection efficiency of the PolyN compared to the PEI control; ** for $p \leq 0.01$.

The duration of the gene expression induced by PolyN lasted up to ~2 weeks, while that of the conventional PEI completely disappeared within 4 days (Figure 4.9). Such a set of data provided the evidence that PolyN is not only biocompatible but also suitable for the efficient, semi-long-term intracellular delivery of the recombinant genes.

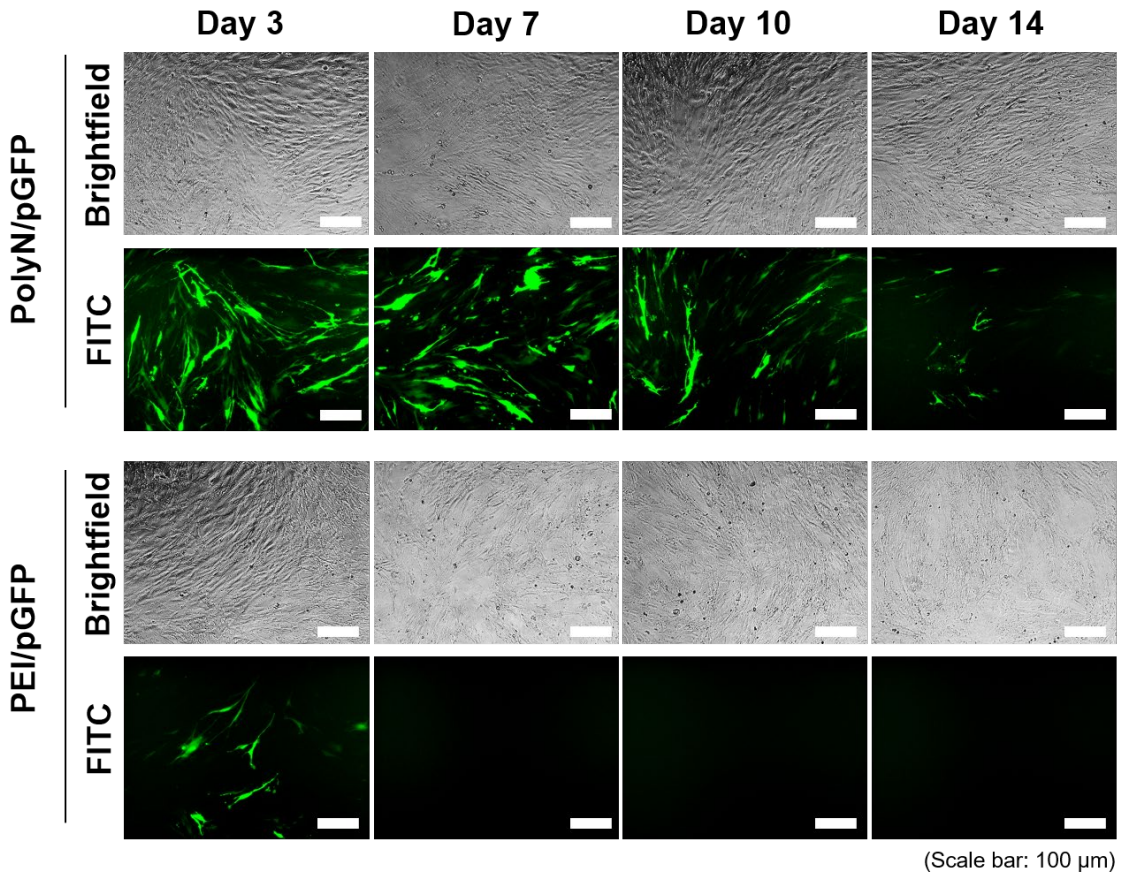

Figure 4.9 Duration of transgene expression by PolyN and conventional PEI. The duration of the reporter transgene expression induced by PolyN was compared with that of the conventional PEI. PolyN enabled the semi-long-term gene expression for up to 2 weeks, whereas PEI only facilitated the short-term gene expression up to only several days.

To further prove the potency of PolyN as a reliable transfection reagent for cell engineering, we searched for a representative cell conversion model involving the overexpression of a single gene. *SOX2*, known as the member of the Yamanaka factors [27], has been reported to play a critical role in the differentiation of the pluripotent cell to the neural progenitor state and its maintenance [28, 29]. Recent studies claimed that the overexpression of a single *SOX2* gene on the human somatic cell is enough to turn on the switch to activate the cellular plasticity and generate the neural stem cell-like precursor, which was capable of the further

differentiation into the neuron-like cell [30, 31]. In this regard, we decided to investigate whether PolyN would support the *SOX2*-mediated generation of neuron-like cells from the human fibroblasts (Scheme 4.3).

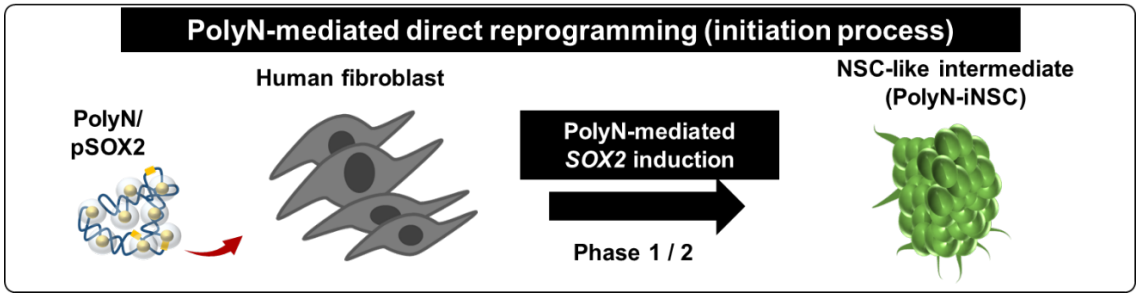

Scheme 4.3 Schematic illustration for the induction of the neural stem cell-like intermediate cells (phase 1 and 2) from human fibroblasts incorporating PolyN/SOX2.

First, pDNA with a gene insert encoding *SOX2* (pSOX2) was mixed with PolyN particle to produce the PolyN/pSOX2 complex. Human fibroblast was treated with the complex and incubated under the optimized condition suitable for the neural stem cell growth. It has been reported that several specific morphological changes would be detected during the *SOX2*-mediated cell reprogramming process, including the generation of the spherical colonies similar to that of the neurosphere [32, 33]. When the cells were treated with PolyN/pSOX2 and cultured under the neural stem cell growth condition, a gradual colony-like formation appeared during the first 7 days (phase 1) (Figure 4.10). As the colonies went on to a vigorous detachment from the bottom of the culture plate, they were collected and transferred to the uncoated plate for further growth. After a couple of days of incubation, the colonies grown in the sufficient size were picked, separated into single cells, and seeded on the laminin-coated flask to fully accomplish the intermediate state (phase 2).

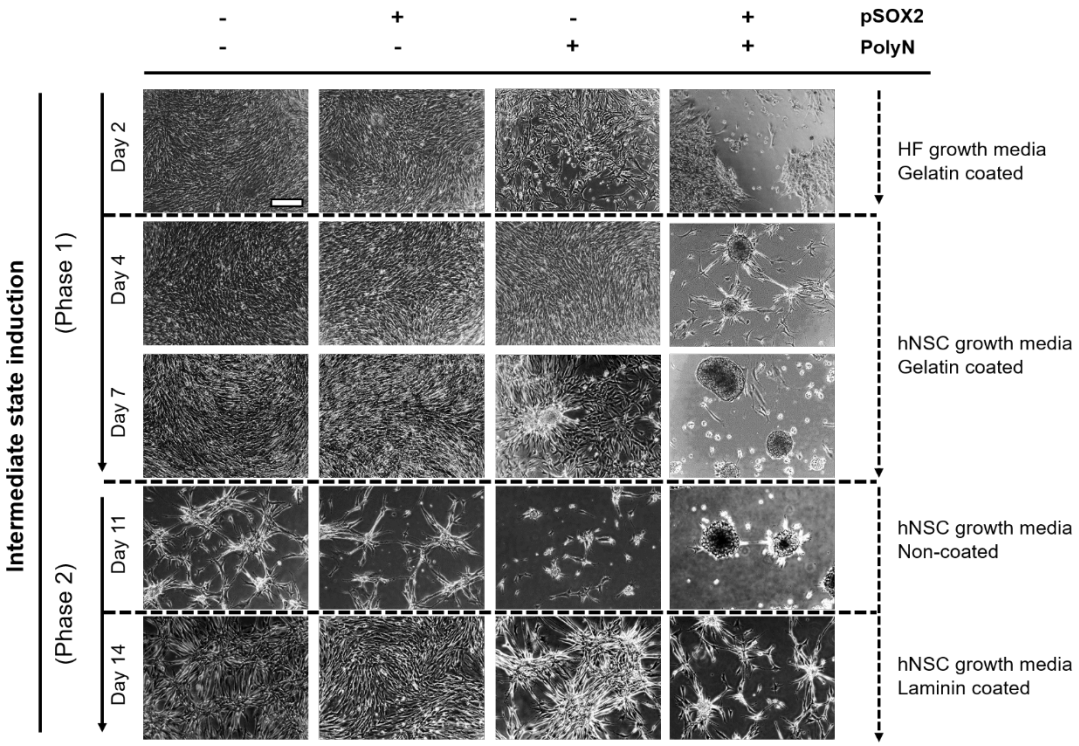

Figure 4.10 Cell morphology analysis during the overall direct cell reprogramming process (I). The first stage represents the induction of the intermediate state. To distinguish the time-point in which representative morphological change (colony-like formation) occurs, the intermediate state induction was split by two phases (phase 1 and 2). Scale bar indicates 100 μm.

To confirm whether the characteristics of the intermediate state resemble those of the neural stem cell, each cell group at the end of phase 1 and 2 (day 7 and 14, respectively) was examined by the overall mRNA expression level of the major neural stem cell markers (*SOX2*, *NESTIN*) (Figure 4.11). In the cells treated with PolyN/pSOX2, mRNA expression of *SOX2* reached its maximum level at day 7, which was approximately 100-fold higher than that of the human neural stem cell (hNSC). Though the expression of *SOX2* steeply decreased on day 14, it maintained a distinct level which was still comparable to that of the hNSC. In the case of *NESTIN*, the expression level showed a gradual increase, reaching the maximum peak of ~0.7 fold of that of the hNSC on day 14.

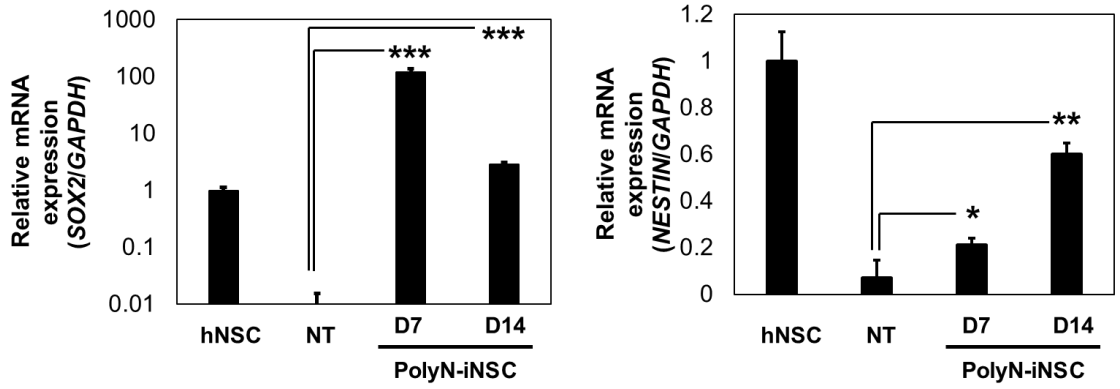

Figure 4. 11 Analysis of the degree of the overexpression of the transgene, *SOX2*, represented in a log scale (left) and comparison of the relative mRNA expression of *NESTIN* (right). *GAPDH* was used as an endogenous control for each analysis. Each gene expression level of hNSC was included in the graph to show the standard expression level, and those of untreated HF (NT) was set as the negative control.

Followed by the mRNA expression analysis, immunostaining revealed that the protein expression level of each hNSC markers of the PolyN-iNSC also correlated well with that of the mRNA expression (Figure 4.12). In detail, the expression of SOX2 was detected at the early stage of phase 1 (day 7) and maintained firmly until the end of phase 2 (day 14). In the case of NESTIN, its protein level could not be observed until phase 2, though the mRNA expression level was detected from phase 1. Referred from the previous studies, we conjectured that such 'translational delay' could be attributed to the time required for the maturation and transportation of the mRNA during the state transition [34].

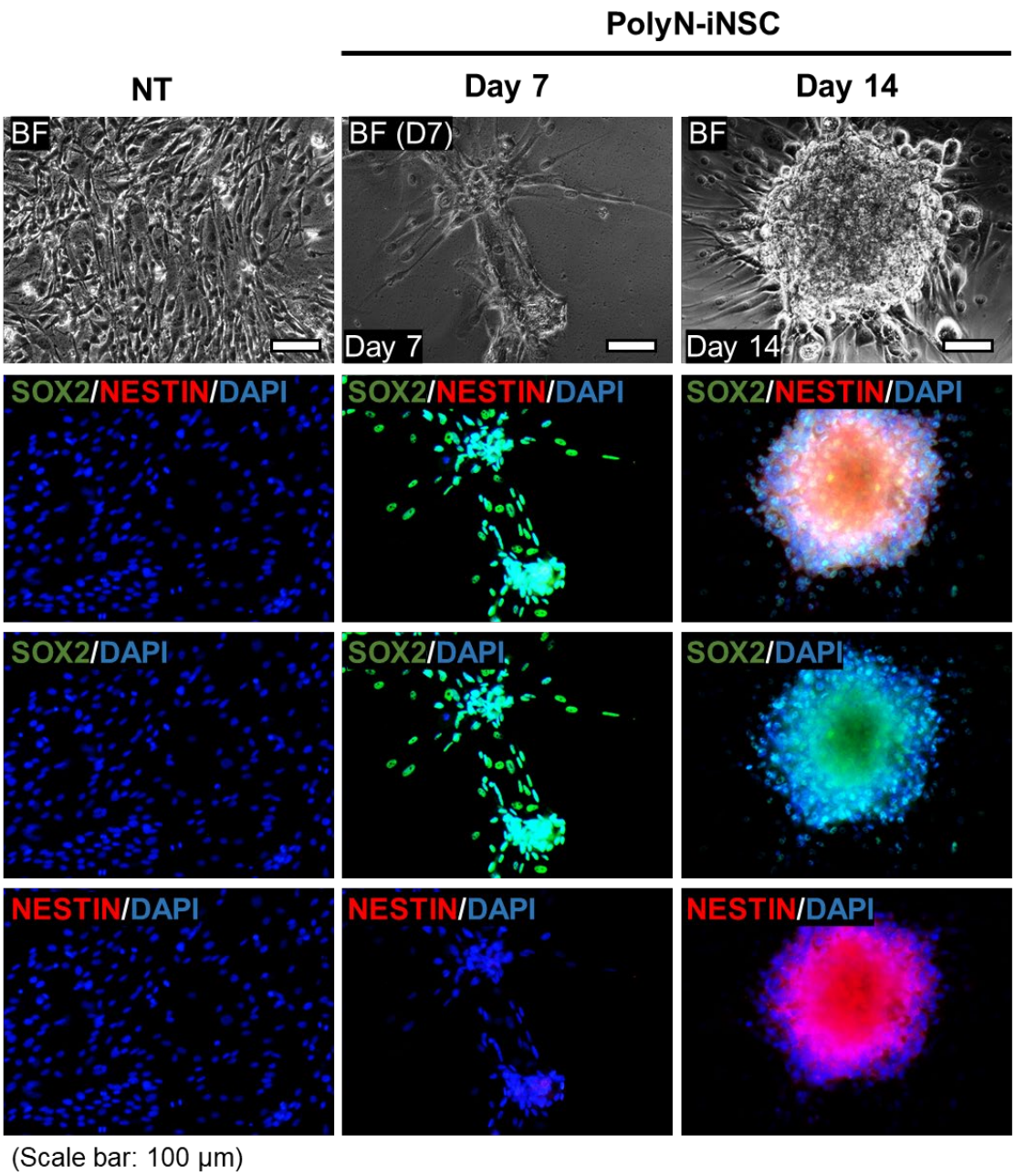

Figure 4.12 Immunocytochemistry analysis for the visualization of the expression of the representative neural stem cell markers during the generation of PolyN-iNSC.

To further determine the duration of the intermediate state, we maintained clones of PolyN-iNSC in the neural stem cell culture condition and tracked down the expression of hNSC markers up to 4 weeks (Figure 4.13). On day 28, it was observed that the expression of both SOX2 and NESTIN was completely diminished. Such data indicate that the previous claims that the upregulation of

NESTIN is highly correlated with the overexpression of *SOX2*, and that the 'cellular plasticity' endowed by the expression of both markers is not permanent in the intermediate state.

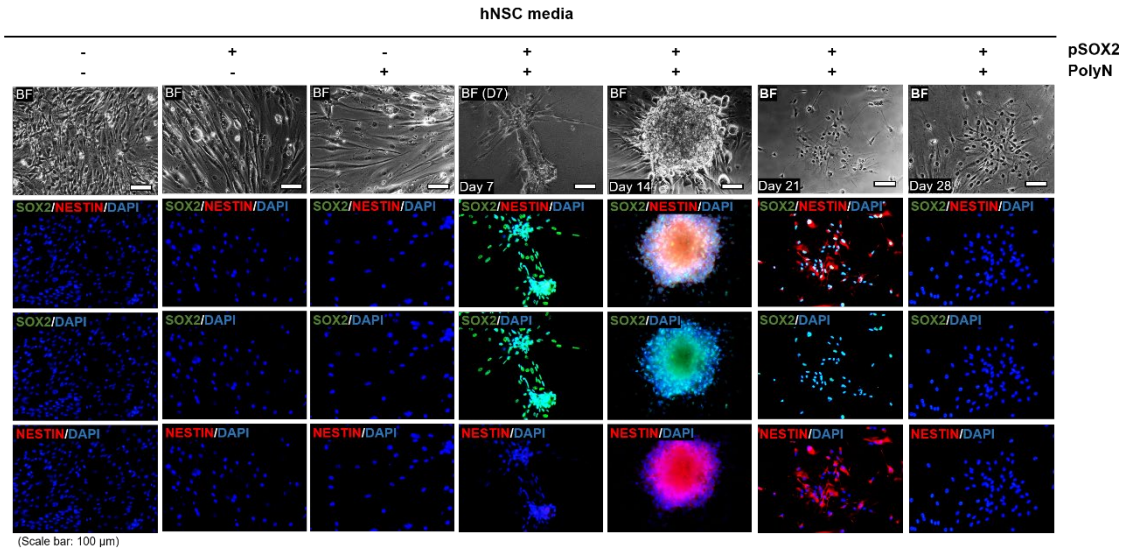

Figure 4.13 Detailed immunohistochemical analysis of the intermediate multipotent state. Cells treated with various combinations of pSOX2 and PolyN were analyzed by immune staining against neural stem cell markers (SOX2, NESTIN). Plus (+) and minus (-) symbols indicate the inclusion or exclusion of the factor. For cells treated with PolyN/pSOX2, time-dependent trafficking was performed up to 4 weeks to investigate the whole induction process and the duration of the neural stem cell-like intermediate. White scale bars indicate 100 μm.

On day 14, each group of cells was collected and stained with the marker-specific antibodies conjugated with specific dyes, and their population for the marker-positive cells was analyzed by flow cytometry. As shown in Figure 4.14A, approximately 80% of PolyN-iNSCs was turned out to be SOX2-positive on day 7. Although a slight decrease in the population was observed at the end of phase 2, still the calculated percentage score reached as high enough as ~60%. Along with the mRNA expression analysis, these data highly support the claim that the gene expression facilitated by PolyN could last at least 2 weeks. To confirm the

efficiency of the generation of intermediate cells, the ratio of the SOX2/NESTIN double-positive cells out of the whole population was analyzed (Figure 4.14B). With the correlation with the previous data in mRNA and protein level, the population of the SOX2/NESTIN double-positive cells was merely detected until day 7, and a dramatic increase of the population to ~17% was observed on day 14. Such data indicate that the generation of the intermediate cells may have been started at the end of phase 1, which explosively increased and reached its peak level at the end of phase 2. The overall results not only depict that the intermediate cells show a neural stem cell-like property but also highly support the hypothesis that only a single administration of the nanoparticle complex is enough to initiate the direct cell reprogramming.

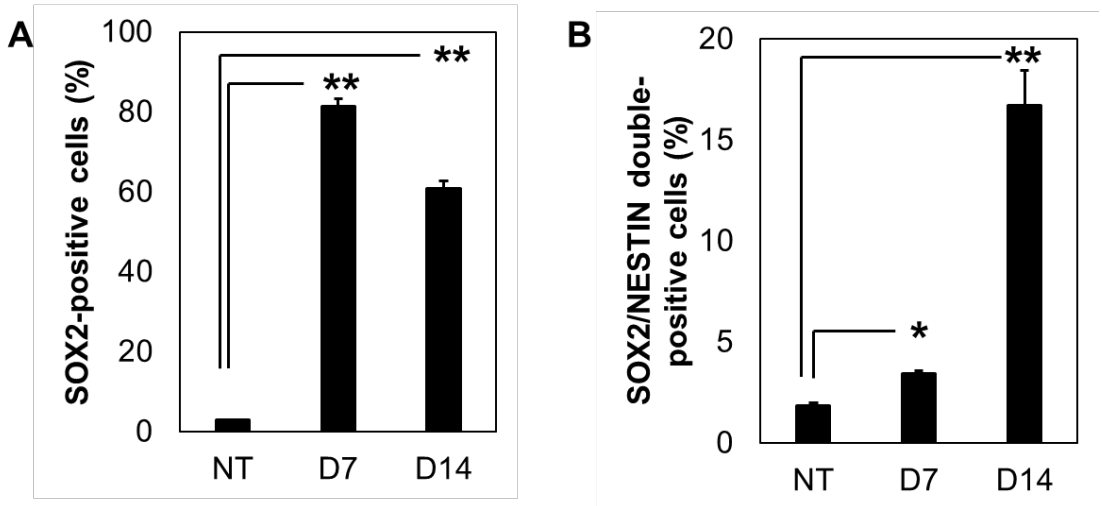

Figure 4.14 Flow cytometry analysis of turnover rate between the direct conversion to the intermediate multipotent state. (A) shows the ratio of the single SOX2-positive cells in each group, while (B) shows the SOX2/NESTIN double-positive cells. Bars indicate mean ± SEM, from three individual replicates in each group (n=3) unless stated otherwise. To determine the significance of the data, one-way ANOVA was performed to derive p-value. * or ** or *** indicates a significant change induced by PolyN/SOX2 compared to the vehicle (NT) control; * for $p \leq 0.05$, ** for $p \leq 0.01$, and *** for $p \leq 0.001$.

Encouraged by the previous results, we then investigated whether the generated

PolyN-iNSC intermediates are capable of neural differentiation. PolyN-iNSCs were plated and grown under the neuronal growth media and their morphology was examined (phase 3) (Scheme 4.4).

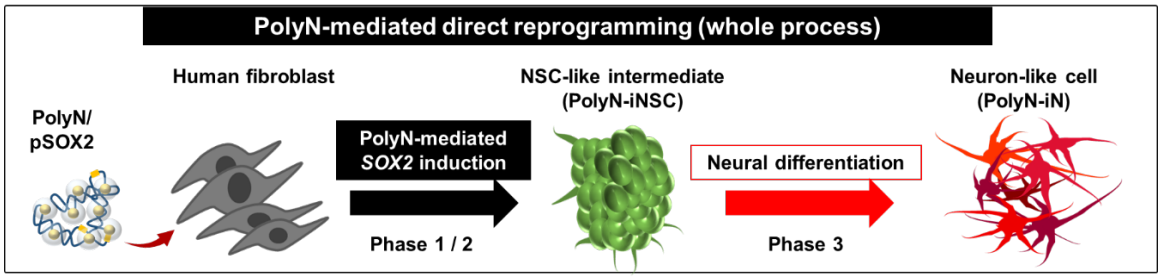

Scheme 4.4 Schematic illustration of the overall cell reprogramming process to generate a neuron-like cell (PolyN-iN), with separated 3 phases.

The end of phase 3 was preliminarily determined to be day 10, which was the time point when the conventional hNSCs were fully generated to neuron under the identical culture condition. During phase 3, the cytoplasm elongation was observed only in PolyN-iNSC. Other groups without pSOX2 or PolyN did not show such morphological change (Figure 4.15).

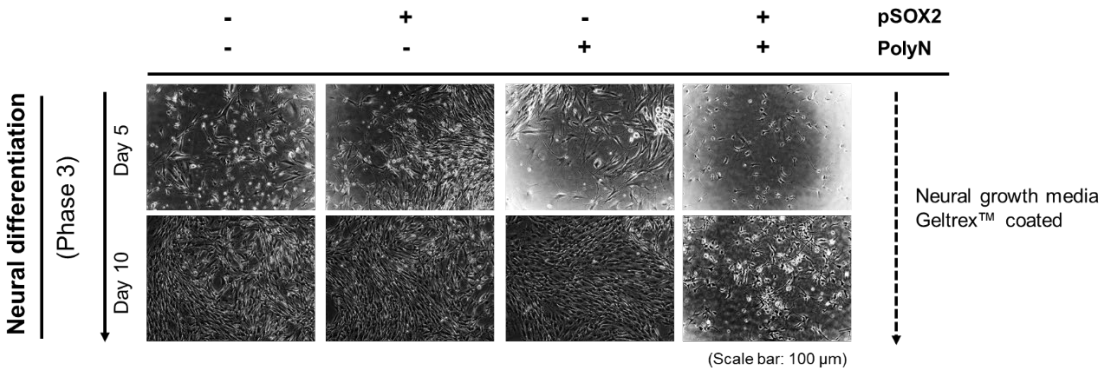

Figure 4.15 Cell morphology analysis during the overall direct cell reprogramming process (II). The overall process representing the neural differentiation (phase 3). Scale bar indicates 100 μm.

During phase 3, a distinct change in mRNA expression of the representative cell

markers (*SOX2*, *NESTIN* for neural stem cell marker; *TUJ1* for the neuronal marker) could be detected (Figure 4.16). Time points in phase 3 were set as day 1, 5, and 10 from the starting timeline of the neuronal differentiation. Each gene expression of the representative period (day 5 and day 10) was analyzed against that of day 1 (D1). In brief, the relative mRNA expression level of *SOX2* and *NESTIN* showed a gradually decreasing tendency, which completely diminished on day 10. In contrast, *TUJ1*, the neuron-specific marker which is not observed in the NSCs, newly started its expression in mRNA level from the beginning of phase 3. It was observed that the expression level of *TUJ1* vigorously increased on day 10.

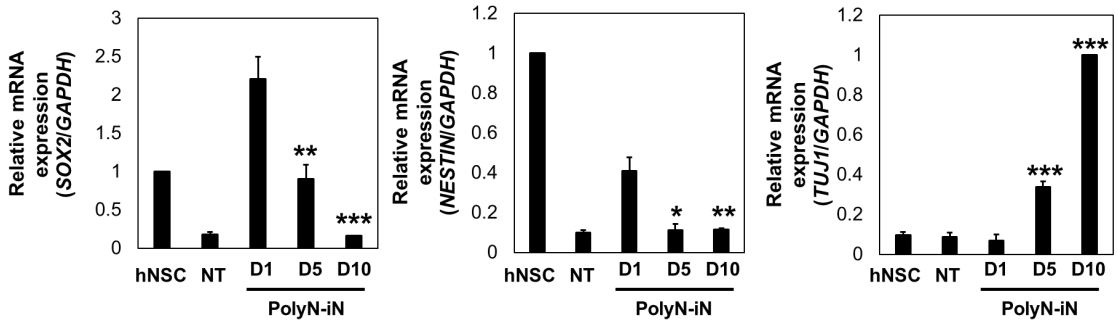

Figure 4.16 Semi-quantitative expression analysis of neural stem cell marker (*SOX2*, *NESTIN*) and neural marker (*TUJ1*). *GAPDH* was used as an endogenous control. Each gene expression level of hNSC and that of untreated HF (NT) was included in the graph to show the standard expression level, and those of day 1 (D1) was set as the negative control. Bars indicate mean ± SEM, from four individual replicates in each group (n=4). To determine the significance of the data, one-way ANOVA was performed to derive p-value. * or ** or *** indicates a significant time-dependent change compared to that of day 1 (D1); * for $p \leq 0.05$, ** for $p \leq 0.01$, and *** for $p \leq 0.001$.

Such a tendency in the expression of the cell markers could also be illustrated in the correlative protein level as well (Figure 4.17). The immunostaining analysis revealed that the expression of SOX2 and NESTIN showed a time-dependent

decrease and the eventual extinguishment on day 10, while that of TUJ1 showed a gradual increase during the whole phase. In day 10, significant elongation of the cytoplasm assumed as neurite outgrowth could be observed with the expression of TUJ1 (indicated with white arrows in the enlarged image). The overall difference in the expression tendency between the neural stem cell markers (SOX2, NESTIN) and the neuronal marker (TUJ1) indicated the successful transition from the intermediate to the neuron-like cells.

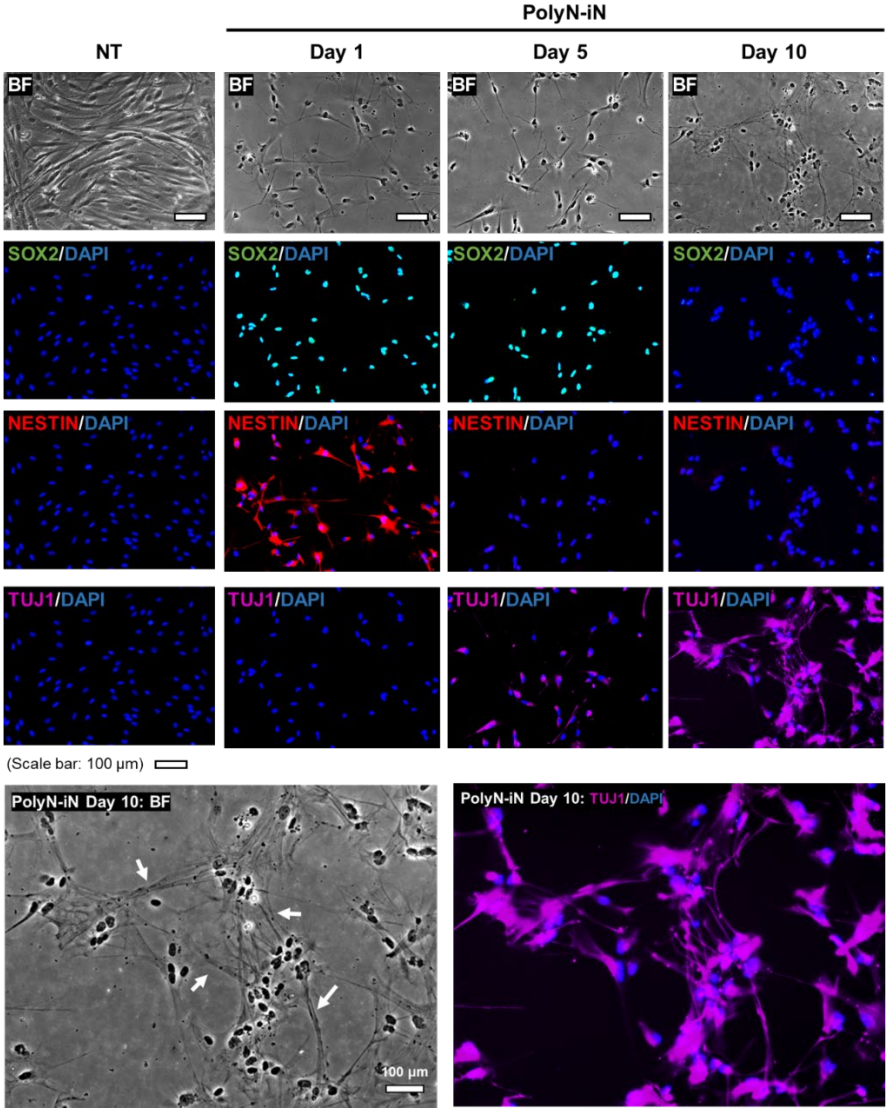

Figure 4.17 Immunocytochemistry analysis for the visualization of the expression of the representative markers (SOX2, NESTIN, and TUJ1) during the generation of PolyN-iN. White arrows in the enlarged image indicate the presumed axonal growth.

Then, the cellular population at each representative time point was further analyzed to determine the neural differentiation efficiency. Compared the that of day 1, the major outcome of the TUJ1-positive cells was observed after day 5 and reached the maximum population of ~40% at day 10 (Figure 4.18A). Besides, we observed a distinct, vigorous cytoplasmic elongation expressing TUJ1 at day 10, which was assumed to be a neurite outgrowth indicating the neuronal maturation. To further clear our doubts about whether the neuronal differentiation was in success, we performed an image-based quantitative analysis of the neurite outgrowth (Figure 4.18B). The neurite outgrowth analysis was performed against 50 representative cells, by measuring the average neurite length of each cell. As expected, the elongation of the neurites showed a gradual increase during phase 3, reaching its maximum length of ~500 μm on day 10. Overall, the comprehensive data highly suggest that the resulting cells generated from the PolyN/pSOX2-mediated direct cell reprogramming undoubtedly showed the neuron-like features, which is significantly distinguishable from that of the parental somatic cells.

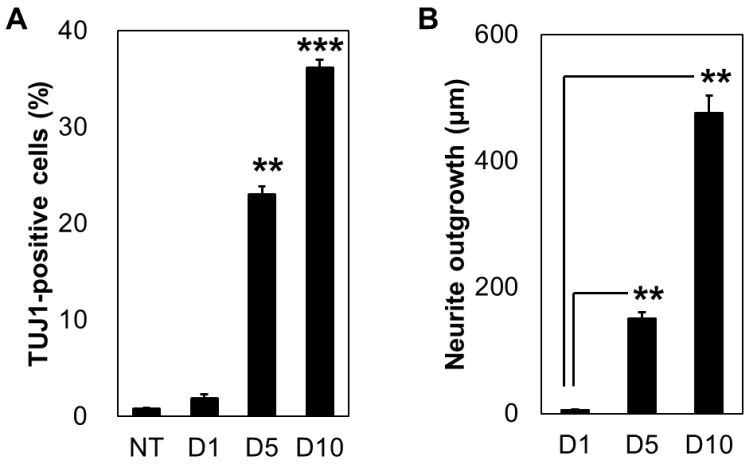

Figure 4.18 Cellular analysis of turnover rate between the neural stem cell-like state and neuronal cell state. (A) Flow cytometry analysis showing the ratio of the

TUJ1-positive cells in each group. Bars indicate mean ± SEM, from three individual replicates in each group (n=3). (B) Neurite outgrowth analysis showing the capability of the representative neural maturation in each group. Bars indicate mean ± SEM, from average neurite length of 50 individual cells (n=50). To determine the significance of the data, one-way ANOVA was performed to derive p-value. * or ** or *** indicates a significant time-dependent change compared to that of day 1 (D1); * for $p \leq 0.05$, ** for $p \leq 0.01$, and *** for $p \leq 0.001$.

4.3 Discussion

To date, various limitations have been under debate, regarding the conventional transfection methods involved in the cell conversion process. Viral vector-mediated methods connote the high risk of the uncontrollable genetic instability, whereas their alternatives, the non-viral methods, have the cytotoxicity issues to overcome. Our initial goal of this research was to come up with the strategy to develop an improved non-viral transfection reagent for cell engineering. We hypothesized that this could be realized by overcoming the cytotoxicity issues argued with the conventional cationic polymer-based reagents. We designed a nanodot in size of <20 nm in diameter surrounded by cationic polymer (PolyN) and created a polyplex with pDNA, followed by the evaluation of the zeta potential, cell viability against the model cell, and transfection efficiency. As a result, PolyN/pDNA complex with net neutral surface charge showed not only a reduction in the cytotoxicity but also a significant increase in the gene expression efficiency compared to those of the conventional PEI/pDNA complex. Such phenomena may be attributed to two factors of PolyN: First, the net neutral charge of the polyN/pDNA complex would reduce the cytotoxicity when administered to cells[35]. Second, the small size of the particle would increase the chance of diffusion in culture media, leading to an increase in cellular contact[36]. We believe that the combinatory effect from both characteristics in a single nanoparticle may have played a role to reduce the cytotoxicity and increase the cellular uptake, leading to enhanced transfection efficiency. Further investigation is undergoing to interrogate the thorough mechanism associated with the low cytotoxicity of PolyN.

Direct cell reprogramming is the unique way of cell conversion, distinguished from transdifferentiation by the presence of the intermediate multipotent state. To demonstrate the practical usage of PolyN, we employed the particle reagent to the

direct cell reprogramming of the human fibroblast into the neuron-like cell. Our data suggest that the single administration of pSOX2-PolyN complex is sufficient to induce the neural stem cell-like intermediate state. With the appropriate growth control, we showed that the intermediate cells could be further converted to the neuron-like cells, indicating that the PolyN could be used as the non-viral cell reprogramming reagent.

4.4 Materials and Methods

Materials and reagents

Paraformaldehyde (4% in water) was purchased from Daejung (Seoul, Korea). Citric acid, sodium azide, HOECHST 33342, fluorescence dye-conjugated anti-rabbit IgG were purchased from Sigma-Aldrich (MO, USA). Linear PEI (25K, cat. no. 23966) was purchased from Polysciences, Inc (PA, USA). DMEM (Dulbecco's Modified Eagle's Medium), 0.25% trypsin-EDTA solution, and PBS (pH 7.4), FBS, and P/S were purchased from WelGENE Inc. (Daegu, Korea). CCK-8 (Cell Counting Kit-8) was purchased from Dojindo Molecular Technologies, Inc. (MD, USA). MLV-RT™ reverse transcriptase was purchased from Elpis Biotech (Daejeon, Korea). Geltrex™, laminin, GlutaMAX™, N2 supplement, B27 supplement, Stempro™ culture media were purchased from Thermo Fisher Scientific Inc. (MA, USA). Primers for qRT-PCR were purchased from Cosmogenetech Inc. (Seoul, Korea). SYBR green master mix was purchased from Applied Biosystems Inc. (CA, USA). Fluorescence conjugated antibodies were purchased from Santa Cruz (TX, USA). Loading STAR™ was purchased from Dyne Bio Inc. (Kyunggi, Korea). Recombinant plasmids encoding either GFP or SOX2 (pGFP, pSOX2) were purchased from Addgene (MA, USA).

Synthesis of nanoparticles

Carbon nanodots were synthesized according to the microwave-mediated hydrothermal reaction. For the synthesis of PolyN, citric acid and linear PEI were mixed in distilled water in a round bottom flask with vigorous stirring. After stabilization, the transparent solution was hydrothermally induced with microwave (1000W) for 5 minutes. The hydrothermal process was repeated until the color of the solution turns into yellowish-white. After the cooling process to

RT, the solution was purified by Amicon™ filter (Millipore, US) and dialysis. The purified PolyN was dried with a freeze dryer and finally dispersed in distilled water to a concentration of 40 mg/mL. As a control, carbon dot was made from citric acid alone (CD from CA) by the same procedure.

Particle characterization

The size and morphology of PolyN were characterized by a high resolution - transmission electron microscope (HR-TEM; model JEM 3010 (JEOL, Japan)) in the National Center for Inter-university Research Facilities (Korea). The size distribution of the nanoparticle was further analyzed with Image J software. UV-Vis spectrophotometer Lambda 465 (PerkinElmer, USA) was used to obtain UV-Vis spectra. Raman spectrophotometer (model T64000 (Horiba, France)) in the National Center for Inter-university Research Facilities (Korea) was used to confirm the sp^2 hybridization. Zeta potential analysis was performed by using Zetasizer NanoS (Malvern Instruments, UK). The measurement of FT-IR spectra was performed with an FT-IR spectrometer (model Nicolet 6700 (Thermo Scientific, USA)).

Loading capacity analysis

In each PCR tube, 1 μg of PolyN or PEI was added with a serially diluted concentration of pGFP (0, 10, 25, 50, 100, 200 ng each) and incubated at RT for 15 minutes. The loading capacity was analyzed by agarose gel electrophoresis, by determining the existence of the pDNA leftovers shown in spilled out from the reagent (shown in the gel band). Before gel loading, the samples were added with LoadingStar™ for the ease of the visualization. The gel was analyzed under UV light with Chemidoc (Bio-Rad, USA).

Cell culture

Human fibroblast (HF) was kindly provided by Professor Kwangseog Ahn from the Department of Biology, Seoul National University. The human neural stem cell (NSC) was purchased from Takara Bio Inc. (Shiga, Japan). HF was cultured with a complete DMEM medium (with 10% FBS, 1% P/S) supplemented with 1x Glutamax in 5% CO_2, 37℃. Human NSC was cultured on the 10μg/mL laminin-coated plate, with NSC growth media (high glucose DMEM supplemented with Stempro™ neural supplement + 20 ng/mL N2 supplement + 20 ng/mL B27 supplement + 1% P/S) in 5% CO_2, 37℃.

Cell viability test

Before the experiment, HF was seeded in a density of 1.6 x10^4 cells / cm^2. After 24 hours of incubation in 5% CO_2, 37℃ condition, PolyN was treated in a serially diluted concentration for the next 24 hours. CCK-8 assay was performed according to the manufacturer's instruction. CCK-8 reagent was treated at a concentration of 10% v/v to each group and incubated for 1~4 hours in the conventional cell culture condition. The quantitative analysis of the change in colorimetric intensity was done by measuring the optical density of formazan salt at 450 nm with a microplate reader (Molecular Devices, Inc., USA). The experiment was carried out in triplicate, of which data were shown as mean ± SEM.

Transfection efficiency analysis

Before the experiment, HF was seeded in a density of 1.5 x 10^3 cells/cm^2 with HF growth media and incubated for 24 hours in 5% CO_2, 37℃ condition. On the next day, the cells were treated with PolyN/pGFP dispersed in the culture media.

Control groups were set by treating raw PolyN, pSOX, PEI, or PEI/pGFP complex on each cell. After 48 hours of incubation, the expression of the reporter gene was observed by a microscope connected with a CCD camera (Olympus, Japan). Then each group of the cells was collected and the GFP-positive cell population was analyzed by flow cytometry.

PolyN mediated, non-viral direct conversion to NSC-like cell (PolyN-iNSC)

Before the induction, HF was seeded to 10μg/mL laminin-coated culture plate in the density of 1.5 x 10^3 cells/cm^2 with HF growth media and incubated for 24 hours in 5% CO_2, 37℃ condition. On the next day, the cells were treated with PolyN/pSOX2 complex with HF growth media. For control groups, cells were treated with pSOX2 or bare PolyN, or PEI/pSOX2 complex. After 2 days of incubation, the media was changed to NSC growth media to induce the direct conversion to NSC-like cells. The media was changed every other day. The colony-like formation should be observed on day 4~7 after the initial media change into NSC growth media. The floating colonies were manually collected and plated on the uncoated 6-well culture plate under the NSC growth media for further growth. After 2-3 days, the floating colonies were collected, split into single cells by the addition of trypsin/EDTA solution and pipetting. After washing with PBS twice, the cells were plated on the laminin-coated culture plate in a density of 5.0 x 10^2 cells/cm^2 under the NSC growth media. For maintenance of the cell, the media was changed every other day.

Neural differentiation of PolyN-iNSC

Before the induction, PolyN-iNSC cells were collected and seeded to Geltrex™-coated culture plate in the density of 5.0 x 10^2 cells/cm^2 under the NSC growth

media and incubated for 24 hours in 5% CO_2, 37℃ condition. The culture media was changed to the neural induction media (high glucose DMEM supplemented with Stempro™ neural supplement + 20 ng/mL N2 supplement + 1% P/S). The media was changed every other day until the neurite growth was observed.

Relative RNA expression analysis

RNA was isolated from each cell-based samples treated with TRIZOL reagent, followed by cDNA synthesis aided by MLVRT™ reverse transcriptase according to the instruction manual. For target gene amplification, each primer was designed in consideration of GC content less than 50% and overlapping between two exons of the target genes with the expected amplicon size of ~100 bps. The primer sequence was confirmed as shown in Table S1. Quantitative real-time PCR (qRT-PCR) was performed to quantify the relative mRNA expression. Each reaction was conducted in a 20 μL volume, with SYBR green master mix. Quantstudio3™ (Applied Biosystems Inc., USA) was utilized in this study in the two-step amplification process. Semi-quantitative viral RNA was analyzed against that of the endogenous control, GAPDH.

Gene	Forward primer (5'- ... -3')	Reverse primer (5'- ... -3')	Amplicon size (bp)
Human *GAPDH*	TCACTGCCACCCAGAAGACTG	GGATGACCTTGCCCACAGC	123
Human *SOX2*	ACCTCTTCCTCCCACTCCAG	CTCTGGTAGTGCTGGGACATG	134
Human *NESTIN*	CTCCAGAAACTCAAGCACC	TCCTGATTCTCCTCTTCCA	145
Human *TUJ1*	CAGATGTTCGATGCCAAGAA	GGGATCCACTCCACGAAGTA	164

Table 4.1 Primer sequence for the quantitative real-time PCR.

Immunocytochemistry

For immunocytochemistry, PolyN-iNSC cells in each stage were plated onto laminin-coated cover glass, followed by the neural differentiation process

previously stated. After fixation with 4% paraformaldehyde, cells were blocked by treating 10% (v/v) FBS and 0.01% (v/v) Tween-20 in PBS for 30 minutes, followed by overnight incubation with either the unconjugated primary antibody (Rabbit anti-TUJ1, 1:500) or the fluorescence-conjugated primary antibodies (Alexa 488-Mouse anti-SOX2, 1:500 and Alexa 594-Mouse anti-NESTIN, 1:500) at 4℃, O/N. After washing with PBS twice, the secondary antibody corresponding to the unconjugated primary antibody was applied (Anti-rabbit IgG, 1:500). After 2-hour incubation at RT, samples were rinsed twice with PBS and each cover glass was removed from the culture plate and mounted to slide glass with Vectashield™ mounting solution containing DAPI.

Flow cytometry analysis

Before the analysis, each cell group was stained with the biomarker-specific antibodies conjugated with a distinct fluorescence dye. Fixation was carried out in option with 4% paraformaldehyde and cells were resuspended in the analysis solution (10% FBS + 1% sodium azide in PBS). Flow cytometry was carried out with the FACS CANTO II instrument (BD Sciences, USA), and the data analysis was performed with Flowjo software (BD Sciences, USA).

Neurite outgrowth analysis

Before the analysis, each group (neural induction (iN) day 1, 3, and 7) was stained with a TUJ1-specific antibody. Representative images of each group were obtained and neurites labeled with antibodies were measured by the Image J program (NIH, USA). The neurite outgrowth analysis was performed against 50 representative cells, by measuring the average neurite length of each cell.

Statistical analysis

Error bars indicate ± SEM unless stated otherwise. The statistical significance of the *in vitro* analysis was evaluated by either a two-tailed t-test or ANOVA.

4.5 Conclusion

In conclusion, we demonstrated the novel, non-viral direct cell reprogramming strategy incorporating PolyN to generate neuron-like cells from the non-neural, somatic cells. Sequential validation revealed that the practical potential of the PolyN as a nanocarrier capable for the efficient intracellular transgene delivery to facilitate the whole process of the direct cell reprogramming. During the initial transfection stage, incorporation of the reprogramming factor with PolyN led to not only the increase in cell viability but also the enhancement of gene expression efficiency compared to that of the conventional PEI. In this regard, we demonstrated the non-viral, direct cell reprogramming of human fibroblasts into the neuron-like cells with a single gene delivery by PolyN. Considering the simple synthetic procedure and its efficacy as the transfection reagent, we believe that the use of PolyN might provide one of the promising options for the convenient and efficient non-viral cell engineering.

4.6 Reference

1. Nonnekes, J.; Goselink, R. J. M.; Ruzicka, E.; Fasano, A.; Nutt, J. G.; Bloem, B. R., *Nat Rev Neurol* **2018,** *14* (3), 183-189.

2. Ney, J. P.; Johnson, B.; Knabel, T.; Craft, K.; Kaufman, J., *Neurology* **2016,** *86* (4), 367-74.

3. Gogel, S.; Gubernator, M.; Minger, S. L., *Gene Ther* **2011,** *18* (1), 1-6.

4. Xu, J.; Du, Y.; Deng, H., *Cell Stem Cell* **2015,** *16* (2), 119-34.

5. Prasad, A.; Manivannan, J.; Loong, D. T.; Chua, S. M.; Gharibani, P. M.; All, A. H., *Regen Med* **2016,** *11* (2), 181-91.

6. Zhang, S. B.; Xu, Y. M.; Wang, B.; Qiao, W. H.; Liu, D. L.; Li, Z. S., *J Control Release* **2004,** *100* (2), 165-180.

7. Dass, C. R., *Int J Pharmaceut* **2002,** *241* (1), 1-25.

8. Lv, H. T.; Zhang, S. B.; Wang, B.; Cui, S. H.; Yan, J., *J Control Release* **2006,** *114* (1), 100-109.

9. Davis, M. E.; Chen, Z.; Shin, D. M., *Nat Rev Drug Discov* **2008,** *7* (9), 771-782.

10. Rosi, N. L.; Mirkin, C. A., *Chem Rev* **2005,** *105* (4), 1547-1562.

11. Baker, S. N.; Baker, G. A., *Angew Chem Int Edit* **2010,** *49* (38), 6726-6744.

12. Gokus, T.; Nair, R. R.; Bonetti, A.; Bohmler, M.; Lombardo, A.; Novoselov, K. S.; Geim, A. K.; Ferrari, A. C.; Hartschuh, A., *Acs Nano* **2009,** *3* (12), 3963-3968.

13. Hola, K.; Zhang, Y.; Wang, Y.; Giannelis, E. P.; Zboril, R.; Rogach, A. L., *Nano Today* **2014,** *9* (5), 590-603.

14. Lee, H. U.; Park, S. Y.; Park, E. S.; Son, B.; Lee, S. C.; Lee, J.

W.; Lee, Y. C.; Kang, K. S.; Kim, M. I.; Park, H. G.; Choi, S.; Huh, Y. S.; Lee, S. Y.; Lee, K. B.; Oh, Y. K.; Lee, J., *Sci Rep-Uk* **2014,** *4*.

15. Miao, P.; Han, K.; Tang, Y. G.; Wang, B. D.; Lin, T.; Cheng, W. B., *Nanoscale* **2015,** *7* (5), 1586-1595.

16. Zhao, A. D.; Chen, Z. W.; Zhao, C. Q.; Gao, N.; Ren, J. S.; Qu, X. G., *Carbon* **2015,** *85*, 309-327.

17. Choi, Y.; Kim, S.; Choi, M. H.; Ryoo, S. R.; Park, J.; Min, D. H.; Kim, B. S., *Adv Funct Mater* **2014,** *24* (37), 5781-5789.

18. Kim, S.; Choi, Y.; Park, G.; Won, C.; Park, Y. J.; Lee, Y.; Kim, B. S.; Min, D. H., *Nano Res* **2017,** *10* (2), 503-519.

19. Li, J. G.; Yu, X. S.; Wang, Y.; Yuan, Y. Y.; Xiao, H.; Cheng, D.; Shuai, X. T., *Adv Mater* **2014,** *26* (48), 8217-8224.

20. Wang, Q.; Zhang, C. L.; Shen, G. X.; Liu, H. Y.; Fu, H. L.; Cui, D. X., *J Nanobiotechnol* **2014,** *12*.

21. Liu, C. J.; Zhang, P.; Zhai, X. Y.; Tian, F.; Li, W. C.; Yang, J. H.; Liu, Y.; Wang, H. B.; Wang, W.; Liu, W. G., *Biomaterials* **2012,** *33* (13), 3604-3613.

22. Pierrat, P.; Wang, R. R.; Kereselidze, D.; Lux, M.; Didier, P.; Kichler, A.; Pons, F.; Lebeau, L., *Biomaterials* **2015,** *51*, 290-302.

23. Wang, H. J.; He, X.; Luo, T. Y.; Zhang, J.; Liu, Y. H.; Yu, X. Q., *Nanoscale* **2017,** *9* (18), 5935-5947.

24. Cai, J. G.; Yue, Y. A.; Rui, D.; Zhang, Y. F.; Liu, S. Y.; Wu, C., *Macromolecules* **2011,** *44* (7), 2050-2057.

25. Hu, S.; Trinchi, A.; Atkin, P.; Cole, I., *Angew Chem Int Ed Engl* **2015,** *54* (10), 2970-4.

26. Chen, Y.; Lian, H.; Wei, Y.; He, X.; Chen, Y.; Wang, B.; Zeng,

Q.; Lin, J., *Nanoscale* **2018,** *10* (14), 6734-6743.

27. Takahashi, K.; Yamanaka, S., *Cell* **2006,** *126* (4), 663-676.

28. Marelli, E.; Scotting, P. J., *Mech Develop* **2017,** *145*, S169-S169.

29. Pevny, L. H.; Nicolis, S. K., *Int J Biochem Cell B* **2010,** *42* (3), 421-424.

30. Lujan, E.; Chanda, S.; Ahlenius, H.; Sudhof, T. C.; Wernig, M., *P Natl Acad Sci USA* **2012,** *109* (7), 2527-2532.

31. Thier, M.; Worsdorfer, P.; Lakes, Y. B.; Gorris, R.; Herms, S.; Opitz, T.; Seiferling, D.; Quandel, T.; Hoffmann, P.; Nothen, M. M.; Brustle, O.; Edenhofer, F., *Cell Stem Cell* **2012,** *10* (4), 473-479.

32. Brazel, C. Y.; Limke, T. L.; Osborne, J. K.; Miura, T.; Cai, J. L.; Pevny, L.; Rao, M. S., *Aging Cell* **2005,** *4* (4), 197-207.

33. Ring, K. L.; Tong, L. M.; Balestra, M. E.; Javier, R.; Andrews-Zwilling, Y.; Li, G.; Walker, D.; Zhang, W. R.; Kreitzer, A. C.; Huang, Y. D., *Cell Stem Cell* **2012,** *11* (1), 100-109.

34. Liu, Y. S.; Beyer, A.; Aebersold, R., *Cell* **2016,** *165* (3), 535-550.

35. Thompson, B.; Mignet, N.; Hofland, H.; Lamons, D.; Seguin, J.; Nicolazzi, C.; de la Figuera, N.; Kuen, R. L.; Meng, X. Y.; Scherman, D.; Bessodes, M., *Bioconjugate Chemistry* **2005,** *16* (3), 608-614.

36. Zhu, M.; Perrett, S.; Nie, G., *Small* **2013,** *9* (9-10), 1619-34.

Conclusion

We showed three representative achievements in the development and demonstration of the nanoplatforms applied for the advanced biotechnology; (1) one is the application of a nanobiosensor for the cost-effective discovery of the antiviral agents; (2) another is the utilization of porous nanoparticle for the rapid chemical-based neural differentiation of stem cells; (3) and the other is the application of modified nanodot for the non-viral, direct reprogramming of somatic cells into functional neurons. In each chapter, we described how we built up the hypothesis to utilize nanomaterials for the development of the system, followed by the criteria for the optimal selection of the appropriate nanomaterial candidates. Based on the unique biochemical properties of the nanomaterials, we described the basic principles to operate each system. Then we demonstrated how each system could be utilized to overcome several methodological limitations of the conventional biomedical and pharmaceutical research. We suggest that the incorporation of appropriate nanosystems to conventional biotechnology could enhance the research efficacy by increasing the experimental convenience and reducing time and labor required. In this way, we believe that our achievements could contribute to accelerate the fundamental research for future drug discovery and therapeutics.

Summary in Korean (국문요약)

생체적합성 나노물질을 활용한 항바이러스 의약품 발굴 및 세포 분화 연구

1980년대 화학 의약품의 대량 생산 및 개발에 힘입어, 합성 의약품으로 대표되는 전통적인 의약품은 비약적인 발전을 이룰 수 있었다. 그러한 성장에도 불구하고 바이러스에 기반한 감염성 질환이나 신경계통 관련 난치성 질환들은 발생 기전의 복잡성 및 관여 인자 제어의 어려움 등 복합적인 이유로 정복되지 못하고 있는 실정이다. 가령 RNA 바이러스성 질환의 경우, RNA 바이러스의 높은 유전적 변이율과 약물 회피 가능성 등으로 인해 치료법 개발 연구에서 난항을 겪고 있으며, 이는 현재 항바이러스제재나 백신 개발 분야가 투자 대비 효율이 높지 않은 주된 이유로 꼽힌다. 최근 몇몇 바이러스성 전염병들의 심각한 창궐로 인하여 항바이러스 제재의 수요가 급증하였고, 이에 따라 수많은 제약 회사들 사이에서 치열한 연구 개발 경쟁이 이루어지고 있다.

한편, 어떤 물질이 나노 수준 (10^{-9})의 크기가 되었을 때 원물질과 다른 고유의 특성을 띨 수 있다는 점이 발견되면서 나노물질의 특성을 연구하는 학문인 나노기술이 많은 관심을 받기 시작했다. 이 학문분야의 다학제적 연구 활용 가능성이 대두된 것은 비교적 최근으로, 다양한 나노물질의 고유한 특성을 활용하여 전기신호 및 광학 신호를 비롯한 다양한 작동 방식을 구현할 수 있는 탐지 장비 및 생체 적용 가능한 나노시약들의 개발 연구가 활발하게 이루어지고 있다.

본 연구에서는 나노기술의 다양한 다학제적 활용 분야 중 대표성을 띠는 세 가지 주제로 1) 형광 기반 나노센서를 활용한 고효율 의약품 발굴 및 2) 다공성 입자를 활용한 줄기세포의 신경 분화 연구, 그리고 3) 카본닷 나노전달체를 활용한 비바이러스성 체세포 직분화 연구를 병렬적으로 수행하였다. 각 연구에 활용된 나노물질들은 저마다 다른 특성을 갖고서

시스템 구현에 기여하였다. 해당 특성들이 어떤 방식으로 활용되었는지, 이를 기반으로 어떻게 각 시스템을 디자인하고 개발하였는지에 대하여 각 장에서 자세히 다루었다.

첫번째 연구에서는 산화그래핀의 특성을 활용하여 개발한 형광 나노바이오센서를 활용해 직접 작용 항바이러스 후보군을 선별하는 전체 과정을 소개하였다. 구체적으로, 형광 표지한 RNA와 산화그래핀을 사용하여 시험관 수준에서 신속하게 RNA 바이러스 특이적 효소의 활성을 정량 분석할 수 있는 플랫폼을 개발하였다. 다중 웰플레이트를 기반으로 형광 신호에 입각한 고효율 스크리닝이 가능하도록 최적화시킨 이 플랫폼을 이용해, FDA 승인된 의약품 라이브러리로부터 대표적인 RNA 바이러스 특이적 효소인 RNA-의존성 RNA 중합효소 (RdRp) 활성 저해제 후보군을 선별하는 데 성공했다. 다음으로 세포 및 동물 감염 모델에 기반한 약효 분석 연구 결과, 선별된 약물 후보군 중 몬텔루카스트가 바이러스 감소 효과뿐만 아니라 생존율 증가, 혈액 내 바이러스 저감 효과 및 감염에 의한 전신 증상 완화 등 실질적인 효능을 갖는 직접 작용 항바이러스 약물 후보군임을 입증하였다.

두번째 연구는 저분자 화합물의 적재 및 세포 내 도입이 가능한 다공성 실리카 나노전달체를 활용하여, 실험실 수준에서 배아줄기세포로부터 신경 발생단계를 재현하는 효율을 높이는 전략에 대한 연구이다. 다양한 표면 계질을 통해 저분자 화합물의 적재 효율을 최대화한 다공성 나노전달체를 선별하고, 해당 나노전달체가 군집 형태로 자라는 쥐 배아줄기세포 내부에 효과적으로 전달됨을 확인하였다. 이 전달체를 활용해 다량의 레티놀산을 배아줄기세포 군집에 안정적으로 공급하여, 레티놀산 관여 기전에 따른 신경세포 분화 과정을 촉진할 수 있음을 입증하였다.

세 번째 연구는 재조합 유전자의 적재 및 세포 내 도입이 가능한 탄소점 나노전달체를 활용하여, 비바이러스성 유전자 전달 방식으로 고효율의 체세포 직분화를 실현하는 전략에 대한 연구이다. 표면 전하를 최적화한

탄소점 나노전달체가 통상적으로 활용되는 고분자성 세포전달체 대비 재조합 유전자의 적재율이 높고 인간 피부세포에 대해 우수한 생체적합도를 보임을 확인하였다. 세포 전환 인자인 SOX2를 대량으로 적재한 탄소점 나노전달체를 인간 피부세포에 처리하여 신경줄기세포 유사 세포로의 직분화에 성공하였고, 직분화된 세포의 배양 조건을 조절하여 신경 유사 세포로의 분화 유도가 가능함을 함께 입증하였다.

상술한 연구 성과들은 기존 신약 발굴 및 세포 공학 분야에서 전통적인 접근 방식으로 해결하기 어려웠던 연구적 한계점들을 극복하는 기초 연구에 활용될 수 있을 것으로 기대한다.

키워드: 나노센서, 나노입자, 약물 전달, 유전자 전달, 항바이러스 신약 발굴, 고효율 스크리닝, 줄기세포, 세포 공학

학번: 2014-21248

Acknowledgments

7년에 걸친 학위과정 동안 많은 일이 있었습니다. 그동안 연구실에서 배운 예비 연구자의 마음가짐과 전공 지식, 그리고 삶의 지혜는 본 연구실 밖 어디서도 경험하지 못할 소중한 자산이었다고 생각합니다. 학위과정을 마치며, 그동안 많은 도움 주신 분들께 감사의 말을 전합니다. 학위 심사 및 연구의 발전 방향과 관련하여 아낌없이 조언해 주신 홍종인 교수님, 정택동 교수님, 이연 교수님께 감사드립니다. 또한 바이러스 효소 단백질의 발현부터 정제에 이르는 모든 분자생물학적 실험 기법들을 체계적으로 가르쳐 주시고 연구 전반에 걸쳐 정말 많은 도움을 주신 고려대학교 우재성 교수님과 연구원분들, 고려대학교 바이러스 은행 문광미 연구원님, 감염 동물 모델을 구축하는 과정 및 실험 데이터 분석에 많은 도움을 주신 전북대학교 장용석 교수님과 박지상 박사님께도 감사드린다는 말씀 꼭 전해드리고 싶습니다. 그리고 언제나 옆에서 지지해주고 함께 고민해 준 정호 오빠, 항상 고맙습니다. 그동안 함께 한 연구실 사람들에게도 고맙다는 말 전하고 싶습니다. 특히 저를 믿고 각 연구 주제를 맡겨 주신 민달희 교수님께 진심으로 감사드립니다. 학위과정을 수행하면서 많은 고민을 함께 나누었던 오랜 친구들인 한빛, 선영, 치혜, 호선, 민주, 성희언니, 애진, 온유언니, 그리고 언제나 아낌없이 조언해주신 지언언니에게 너무나 고맙다는 말 전하고 싶습니다. 그리고 누구보다도, 제가 흔들릴 때마다 저를 모든 방면에서 지지하고 잡아 주신 제 정신적 지주이자 멘토인 부모님과, 각자 자리에서 최선을 다하며 서로 응원해주는 동생들, 그리고 제 인생의 롤모델이신 할머니께 사랑하고 감사하다는 말을 꼭 전하고 싶습니다.